



저작자표시-비영리-변경금지 2.0 대한민국

이용자는 아래의 조건을 따르는 경우에 한하여 자유롭게

- 이 저작물을 복제, 배포, 전송, 전시, 공연 및 방송할 수 있습니다.

다음과 같은 조건을 따라야 합니다:



저작자표시. 귀하는 원저작자를 표시하여야 합니다.



비영리. 귀하는 이 저작물을 영리 목적으로 이용할 수 없습니다.



변경금지. 귀하는 이 저작물을 개작, 변형 또는 가공할 수 없습니다.

- 귀하는, 이 저작물의 재이용이나 배포의 경우, 이 저작물에 적용된 이용허락조건을 명확하게 나타내어야 합니다.
- 저작권자로부터 별도의 허가를 받으면 이러한 조건들은 적용되지 않습니다.

저작권법에 따른 이용자의 권리는 위의 내용에 의하여 영향을 받지 않습니다.

이것은 [이용허락규약\(Legal Code\)](#)을 이해하기 쉽게 요약한 것입니다.

[Disclaimer](#)

공학박사 학위논문

Lysosomal enzyme specific nanodrugs for targeted cancer therapy

표적형 항암 치료를 위한 리소좀 특이적 나노약물

2023년 2월

서울대학교 대학원

재료공학부 재료공학전공

조 한 희

Lysosomal enzyme specific nanodrugs for targeted cancer therapy

지도 교수 안 철 희

이 논문을 공학박사 학위논문으로 제출함
2022년 12월

서울대학교 대학원
재료공학부 재료공학전공
조 한 희

조한희의 공학박사 학위논문을 인준함
2023년 1월

위 원 장 유 웅 열 (인)

부위원장 안 철 희 (인)

위 원 권 민 상 (인)

위 원 김 광 명 (인)

위 원 김 주 은 (인)

Abstract

Despite the development of cancer therapy, conventional chemodrugs are still mainly used for cancer treatment due to its wide range of application and accessibility. However, common drugs have fetal side effects due to its non-specific mode of action. For that reason, several modified chemodrugs have been developed for targeted cancer therapy. Although targeting efficiency of conventional drugs have been improved by modification, such limitations are still remained. Herein, prodrug strategy was combined with enhancement drug delivery system for improvement of both tumor targeting efficiency and tumor specificity. In chapter 1, monomethyl auristatin E (MMAE), which has high toxicity, was introduced as anticancer agents. To obtain tumor specific toxicity, tumor overexpressed enzyme cathepsin B cleavable peptide FRRG was conjugated to the MMAE. The phenylalanine in the FRRG peptide has intermolecular hydrophobic interaction, which caused nano-formulation of FRRG conjugated MMAE. This FRRG-MMAE nano-structure was accumulated in tumor site due to EPR effects. After that, overexpressed cathepsin B cleaved MMAE conjugated peptide and releasing free MMAE only in the tumor site. In chapter 2, albumin was adopted as drug carrier for enhanced tumor targeting efficiency. For using albumin, maleimide functional group was introduced to cathepsin B cleavable peptide FRRG conjugated doxorubicin. Maleimide-FRRG-Dox could bound to the serum albumin via click chemistry, which improved tumor targeting efficiency and blood half-life. In chapter 3, a novel drug PROTAC was introduced to the maleimide functional group which is conjugated as ester bond. Maleimide-PROTAC was accumulated in the tumor site via albumin binding, and releasing free PROTAC due to tumor overexpressed

esterase. Overall, in this study, the new designed prodrugs were composed of 3 parts. The first part was functional moieties or amino acid sequence for enhanced tumor targeting efficiency. The second part was linkers which were cleaved by tumor overexpressed enzyme or tumor microenvironment. The last part was anticancer agents which is commonly used in first-line chemotherapy. Improved tumor targeting efficiency was observed in new designed prodrugs. Also, these novel prodrugs didn't show any safety problems, which means overcoming limitation of tumor specificity.

Keywords : Cancer, targeted therapy, cathepsin B, albumin, peptide-drug conjugate, PROTAC

Student number : 2016-20832

Table of contents

Abstract.....	i
Table of contents.....	iii
List of Figures.....	vii

Chapter 1. Introduction

1.1. General introduction	1
1.2. Linkers for tumor specificity	2
1.3. Functional moieties for enhanced targeting efficiency.....	5
1.4. Research rationale.....	6
1.5. References.....	7

Chapter 2. Tumor-specific monomethyl auristatin E (MMAE) prodrug nanoparticles for safe and effective chemotherapy

2.1. Introduction.....	13
2.2. Materials and methods.....	18
2.2.1. Materials.....	18
2.2.2. Preparation and characterization of FRRG-MMAE nanoparticles.....	18
2.2.3. Cellular uptake	19
2.2.4. Cytotoxicity study.....	20
2.2.5. Antitumor efficacy and toxicity study of FRRG-MMAE nanoparticles in breast tumor models	20
2.2.6. Statistics	21

2.3. Results.....	21
2.3.1. Preparation and characterization of FRRG-MMAE Nanoparticles	21
2.3.2. Cellular uptake and tumor cell selective cytotoxicity of FRRG-MMAE nanoparticles	30
2.3.3. Antitumor efficacy and safety of FRRG-MMAE nanoparticles in breast tumor- bearing mice.....	35
2.4. Conclusions.....	43
2.5. References.....	44

Chapter 3. Cancer-targeted therapy using cathepsin B activated albumin-binding doxorubicin prodrug

3.1. Introduction.....	48
3.2. Materials and methods.....	49
3.2.1. Materials.....	49
3.2.2. Synthesis of cathepsin B-overexpressed tumor cell activatable albumin- binding doxorubicin prodrug (Al-ProD)	50
3.2.3. Characterization of Al-ProD.....	51
3.2.4. Cellular uptake	52
3.2.5. Cytotoxicity assay.....	52
3.2.6. Western blot	53
3.2.7. Pharmacokinetics (PK).....	53
3.2.8. Biodistribution in breast tumor models.....	54
3.2.9. Antitumor efficacy and toxicity evaluation.....	55
3.2.10. Statistics	55

3.2. Results.....	56
3.3.1. Albumin-binding and selective activation of Al-ProD	56
3.3.2. Cancer cell-selective cytotoxicity of Al-ProD	67
3.3.3. Pharmacokinetics and tumor targeting of Al-ProD	74
3.3.4. Antitumor efficacy and toxicity studies of Al-ProD in breast tumor models..	80
3.4. Conclusions.....	85
3.5. References.....	86

Chapter 4. In situ albumin-binding and esterase-specifically cleaved BRD4-degrading PROTAC for targeted cancer therapy

4.1. Introduction.....	90
4.2. Materials and methods.....	96
4.2.1. Materials.....	96
4.2.2. Instruments.....	97
4.2.3. Synthesis of ECMal-PROTAC	98
4.2.4. In vitro albumin binding and dissociation test with ECMal-PROTAC	98
4.2.5. Preparation of Cy5.5-conjugated Arv-771 and BSA.....	99
4.2.6. In vitro cellular uptake and cell viability of ECMal-PROTAC	100
4.2.7. Western blot analysis	101
4.2.8. In vivo biodistribution of ECMal-PROTAC with tumor-bearing mice	102
4.2.9. In vivo therapeutic efficacy of ECMal-PROTAC against tumor-bearing mice	103
4.2.10. Statistical analysis	104
4.3. Results.....	105

4.3.1. Synthesis of BRD4-degrading ECMal-PROTAC	105
4.3.2. In vitro cellular uptake, BRD4 degradability, and therapeutic effect of ECMal-PROTAC.....	115
4.3.3. In vivo biodistribution of ECMal-PROTAC in tumor-bearing mice	121
4.3.4. In vivo therapeutic efficacy of ECMal-PROTAC in tumor-bearing mice	130
4.4. Conclusions.....	142
4.5. References.....	143
Chapter 5. Conclusions.....	148

List of Figures

Figure 2.1. Schematic illustration for the MOA of FRRG-MMAE.

Figure 2.2. Preparation of FRRG-MMAE nanoparticles and analysis data of synthesized FRRG-MMAE.

Figure 2.3. Size distribution and morphology of FRRG-MMAE nanoparticles.

Figure 2.4. The stability of FRRG-MMAE nanoparticles in mouse serum

Figure 2.5. Molecular dynamic simulation of one FRRG-MMAE molecule for 20 ns.

Figure 2.6. MD simulation of two FRRG-MMAE molecules for 20 ns.

Figure 2.7. MD simulation of two FRRG peptide molecules for 20 ns.

Figure 2.8. MD simulation of ten molecules of (a) FRRG-MMAE or (b) FRRG peptide.

Figure 2.9. The ratio of overlap surface over total surface areas of the FRRG-MMAE of FRRG peptide molecules.

Figure 2.10. Enzymatic cleavage assays of FRRG-MMAE nanoparticles

Figure 2.11. Metabolite assay of FRRG-MMAE nanoparticles after incubation with cathepsin B.

Figure 2.12. Confocal laser scanning microscopy images for intracellular dynamic study of FRRG-MMAE.

Figure 2.13. The tubulin formation of (a) 4T1 and (b) H9C2 cells after treatment with free MMAE or FRRG-MMAE.

Figure 2.14. The cell cytotoxicity study of 4T1 and H9C2 cells after treatment with (a) FRRG-MMAE or (b) free MMAE.

Figure 2.15. Tumor targeting efficiency study of FRRG-MMAE nanoparticles.

Figure 2.16. Antitumor efficacy of FRRG-MMAE nanoparticles.

Figure 2.17. Tumor tissue stained with fluorescent dye Cy5-conjugated tubulin Antibody.

Figure 2.18. Antitumor efficacy and safety of FRRG-MMAE nanoparticles in 4T1 breast tumor-bearing mice.

Figure 2.19. Tumor growth of 4T1 tumor-bearing mice during treatment with 0.5 mg/kg MMAE once every three days.

Figure 2.20. Hematological parameters of mice treated with saline, free MMAE or FRRG-MMAE for 5 days.

Figure 2.21. Safety study of FRRG-MMAE nanoparticle via measurement of body weight and survival rate after treatment.

Figure 3.1. Schematic illustration of *in situ* albumin-mediated cancer-targeted therapy by Al-ProD.

Figure 3.2. Synthetic scheme of Al-ProD.

Figure 3.3. The purity (> 99%) of Al-ProD was confirmed by high performance liquid chromatography (HPLC).

Figure 3.4. The molecular weight of Al-ProD was confirmed via MALDI-TOF mass spectrometer.

Figure 3.5. Albumin-binding of Al-ProD. Al-ProD was incubated with various serum albumins at room temperature.

Figure 3.6. Albumin binding affinity of HSA analyzed via RP-HPLC.

Figure 3.7. MALDI-TOF analysis results of human serum albumin and human serum albumin-bound Al-ProD.

Figure 3.8. HPLC chromatograms when Al-ProD was incubated with cathepsin B.

Figure 3.9. Metabolite assay of Al-ProD. Glycine-conjugated doxorubicin (G-DOX) released from Al-ProD was confirmed via MALDI-TOF mass spectrometer.

Figure 3.10. HPLC chromatograms when Al-ProD was incubated with various type of enzymes and normal saline (hydrolysis).

Figure 3.11. Cathepsin B expression levels of MDA-MB-231 and H9C2 cells.

Figure 3.12. Confocal laser scanning microscope images of MDA-MB-231 and H9C2 cells treated with Al-ProD.

Figure 3.13. Quantification analysis of DOX fluorescence in nuclei or cytosol of Al-ProD treated MDA-MB-231, H9C2 and cathepsin B-inhibitory siRNA-treated MDA-MB-231 cells.

Figure 3.14. Fluorescence images of MDA-MB-231 and H9C2 cells treated with free Dox.

Figure 3.15. Cell cytotoxicity of Al-ProD or free Dox in MDA-MB-231 and H9C2 cells.

Figure 3.16. Pharmacokinetics (PK) profiles of Al-ProD and free DOX.

Figure 3.17. NIRF images of MDA-MB-231 tumor-bearing mice treated with Al-ProD or free DOX.

Figure 3.18. Quantification analysis on the DOX fluorescence at tumor tissues in NIRF images.

Figure 3.19. Ex vivo imaging of organs from mice treated with Al-ProD or free DOX after 12 h injection.

Figure 3.20. Fluorescence images of whole tumor tissues after 12 h of Al-ProD or free DOX treatment.

Figure 3.21. Tumor growth curves of MDA-MB-231 tumor-bearing mice after saline, free DOX, or Al-ProD treatment.

Figure 3.22. Tumor tissues stained with H&E or TUNEL to assess antitumor efficacy on day 20 after treatment.

Figure 3.23. Body weights during treatment.

Figure 3.24. Mice survival during treatment.

Figure 3.25. Major organs stained with H&E to assess structural abnormalities on day 20 after treatment.

Figure 4.1. Schematic illustration for the MOA of ECMal-PROTAC.

Figure 4.2. Schematic illustration for the In vivo MOA of ECMal-PROTAC.

Figure 4.3. Synthetic scheme of ECMal-PROTAC.

Figure 4.4. Characterization of ECMal-PROTAC.

Figure 4.5. Albumin binding affinity study of ECMal-PROTAC.

Figure 4.6. Through the DLS analysis before and after the binding of ECMal-PROTAC.

Figure 4.7. Cleavage study of the albumin bound ECMal-PROTAC by esterase.

Figure 4.8. In vitro cellular uptake of ECMal-PROTAC.

Figure 4.9. The intracellular fluorescence intensities were quantified.

Figure 4.10. In vitro protein degradability of ECMal-PROTAC via western blot assay.

Figure 4.11. The relative expression level of (a) c-Myc, Bcl-2 and (b) BRD4 in 4T1 cells depending on the ARV-771 or ECMal-PROTAC treatment, plotted as a function of concentration.

Figure 4.12. The cytotoxicity study of ARV-771 and ECMal-PROTAC in 4T1 breast cancer cell.

Figure 4.13. Pharmacokinetic profiles of intravenously administered Cy5.5-ARV-771 and Cy5.5-Alb-ECMal-PROTAC.

Figure 4.14. The time-dependent biodistribution of Cy5.5-Alb-ECMal-PROTAC and Cy5.5-ARV-771.

Figure 4.15. Quantification analysis on the Cy5.5 fluorescence at tumor tissues in NIRF images.

Figure 4.16. The ex vivo fluorescence images of excised major organs and tumor tissues after the single administration of Cy5.5-ARV-771 and Cy5.5-Alb-ECMal-PROTAC, and (b) their quantified fluorescence intensities.

Figure 4.17. The ex vivo fluorescence images of excised tumor tissues were obtained and their fluorescence intensities were quantified.

Figure 4.18. The whole tumor confocal fluorescence images were additionally obtained with the excised tumors.

Figure 4.19. Excised tumor tissues were further co-stained with DAPI and CD31, analyzed with confocal fluorescence microscopy.

Figure 4.20. Cross-sectional fluorescence signals of yellow line on the figure 3.19 were plotted.

Figure 4.21. The tumor growth profile according to the repeated treatment of saline, native ARV-771, or ECMal-PROTAC.

Figure 4.22. (a) Digital images of excised tumors and (b) confocal fluorescence images of excised tumor tissues after their TUNEL staining.

Figure 4.23. The changes in body weights of saline-, ARV-771-, and ECMal-PROTAC-treated mice.

Figure 4.24. The histological analysis of major organs extracted from saline, ARV-771 and ECMal-PROTAC treated groups.

Figure 4.25. TUNEL assay of livers excised from experimental groups.

Figure 4.26. Western blot assay of excised tumor tissues with ECMal-PROTAC treatment showed reduced levels of BRD4, c-Myc, and Bcl-2.

Figure 4.27. Quantification analysis of the band intensity on the figure 4.26.

Figure 4.28. The BRD4-degrading and subsequent c-Myc-suppressing properties of ECMal-PROTAC were further visualized by staining tumor tissues.

Figure 4.29. DAB-stained tumors with repeated treatment of saline, ARV-771, and ECMal-PROTAC, showing the BRD4 deficiency in ECMal-PROTAC-treated tissues.

Figure 4.30. The MOA of BRD4-degrading PROTAC was schematically described.

Chapter 1. Introduction

1.1. General introduction

In recent years, various methods are used for cancer therapy. Among them, chemotherapy is the main treatment for all stage of cancer [1]. These anticancer agents tend to act specifically on cancer cells with rapid proliferation. For example, doxorubicin which induces cell apoptosis through DNA intercalating mainly affects rapid differentiation cells due to the mode of action [2]. For this reason, chemodrugs also affect rapid dividing normal cells with various side effects, such as nausea, vomiting and hair loss [3]. To overcome these limitations, several limitations, several methods are used for the conventional anticancer agents. For example, for enhancement tumor targeting efficiency, albumin nanoparticle (Abraxane), liposome carrier (Doxil) and antibody conjugate (Brentuxibam-vedotin) were developed [4-6]. However, even though these modified chemodrugs covered several limitations, they still have several limitations such as low specificity, low drug loading efficiency and drug leaking phenomenon [7]. Therefore, new design is required for effective and safe tumor targeting chemotherapy.

Two strategies could be adopted for new design. The first strategy is increasing tumor targeting efficiency of first-line chemodrugs with developed drug delivery systems such as nano-formulation and antibody conjugation [4-6]. Chemodrugs with this method could target tumor site effectively and accumulate in tumor site via EPR (enhanced permeability and retention) effect [8]. Nevertheless, this advanced chemodrugs still have several limitations such as native toxicity of additives and

multidrug resistance due to tumor heterogeneity [9-13]. The other strategy is to develop called 'Prodrug'. The first-line conventional drugs could be modified as inactive form, and it turns over to active form at tumor specific condition such as low pH, hypoxia and overexpressed enzyme [14]. The meaning of prodrug is these modified drugs which could be activated in certain circumstance. Using this method, side effects of drugs could be minimized due to its inactive form at normal tissue. However, prodrugs with these linkers have low tumor targeting efficiency which cause possibility of nonspecific cleavage because of ubiquitously existed physiological conditions in the body. Nevertheless, combination of these strategies could increase therapeutic effect for the cancer treatment with advanced tumor targeting efficiency and specificity [14, 15]. Also, various combination structure could be generated with cancer specifically cleavable linkers and tumor targeting moieties for maximize anticancer effect.

1.2. Linkers for tumor specificity

For reducing side effects on normal tissues caused by antitumor chemotherapy, various linkers could be conjugated to conventional drugs to turned into inactive form. The linkers could be cleaved by tumor microenvironment such as low pH, hypoxia and overexpressed enzyme and release free drugs to the specific site [16].

Cathepsins, lysosomal enzyme of cysteine proteases, act an important role in cellular proteolysis. Several studies have revealed that cathepsins are involved in tumor progression and metastasis [17]. Especially, cathepsin B is well-known overexpressed enzyme in malignant tumors, therefore, many cathepsin B cleavable produrgs with anticancer agents have been developed [18]. For example, cathepsin B cleavable

peptide was adopted between dendritic polymer and linear polymer for formation of nanoparticles to improve drug delivery efficiency [19]. At the tumor site, doxorubicin contained dendritic polymer was released due to cleavage of peptide by tumor overexpressed cathepsin B. As another example, doxorubicin was conjugated with peptide composed of cathepsin B cleavable sequence and phenylalanine amino acid [20]. In this peptide, phenylalanine act as the driving force of forming nanoparticles and this phenomenon increased the efficiency of drug delivery systems via EPR effect. Also, if nanoparticles accumulated in tumor, overexpressed cathepsin B cleaved peptide and release free doxorubicin at the tumor site inducing cancer cell apoptosis.

Carboxylesterases (CES) are carboxylic ester cleavage enzyme which are endoplasmic-reticulum-resident [21]. They have significant roles in the metabolism of xenobiotics such as drugs and toxins [22]. Several types of CES in the human body were revealed, and CES2 overexpression is observed in several cancer cells such as multiple myeloma, thyroid papillary carcinoma and kidney adenocarcinoma [23]. Therefore, carboxylic ester can be introduced for prodrug that is activated by CES. In this mechanism, toxicity of typical anticancer agents is firstly hidden by various functional moieties, conjugated with carboxylic ester bond until prodrugs are cleaved by CES and release conventional chemodrugs. Recently, CPT-11 (7-ethyl-10[4-(1-piperidino)-1-piperidino]carbonyloxycamptothecin), which was conjugation of camptothecin and δ -lactone ring by ester bond, was developed [24]. After CES2 cleaved the carboxylic ester of CPT-11, camptothecin was released and dealt damage to DNA of target cells.

Caspases enzyme, a group of proteases, are in programmed cell death, apoptosis and inflammation protocol. In recent years, 12 caspases are revealed in

humans. Among them, caspase-3 is highly related to cell apoptosis, activated by both intrinsic and extrinsic pathways. For that reason, caspase-3-cleavable linker is adopted to build prodrug. Because of caspase-3 expressed mechanism, targeted-therapy or radiotherapy are pre-treated before using caspase-3 activatable prodrug [25, 26]. If pretreated cancer cells are induced apoptosis, caspase-3 enzyme is released from dead cells to adjacent cells which are indirectly treated. Then cytotoxins are released from prodrug by caspase-3, and this phenomenon is called bystander killing effect [27]. For example, albumin binding moiety could be linked by caspase-3 cleavable peptide to anticancer agent doxorubicin [28]. The synthesized molecule was finally bound to serum albumin for drug delivery with inducing apoptosis of cancer cells in tumor site, also subsequently killed adjacent tumor.

Matrix metalloproteinases (MMPs) play a prominent role as cleave various ECM (extracellular matrix) proteins, inactivated cytokine and chemokine [29]. In terms of anticancer prodrugs, MMPs are important due to its role in cancer cell proliferation, differentiation, migration and angiogenesis [30]. Particularly, because of MMPs' significant role in metastasis, MMP-2 and MMP-9 cleavable linker have been a main target for anticancer prodrugs. For example, MMP-cleavable peptide (Gly-Pro-Leu-Gly-Val or Pro-Val-Gly-Leu-Ile-Gly) was introduced to various conventional drugs, such as paclitaxel, doxorubicin, and methotrexate for deactivation of their toxicity, until they were reactivated by MMP-2 induced cleavage to recover the original toxicity [31-35]. In recent years, MMPs cleavable prodrugs encapsulated in nanoparticles, and specifically released at tumor site [36, 37]. The introduced anticancer agents with the MMPs cleavable linker could be conjugated or interacted hydrophobically with polymers then formed nanoparticles for advanced drug delivery efficiency.

Hydrazone, which is cleaved by low pH condition, is used as linker between functional moieties and chemodrugs for prodrug. Aldoxorubicin (INNO-206), which has maleimide functional group with hydrazone linker, is in clinical trials phase II for the patients who are suffered from breast cancer [38]. By the low pH due to tumor microenvironment, hydrazone bond is cleaved, and free doxorubicin is released to the tumor specifically for apoptosis.

1.3. Functional moieties for enhanced targeting efficiency

Prodrugs without additional moieties could be a good selection for cancer therapy. However, because of its low targeting efficiency, various challenge has been arisen such as nonspecific releasing of anticancer agents and short circulative half-life of drugs. For that reason, several moieties could be introduced to prodrugs for enhanced properties such as tumor targeting efficiency, specific cytotoxicity and drug releasing trigger.

Albumin, which is the most abundant protein in blood plasma, could be introduced to drug delivery systems [39]. Due to its long circulatory half-life and passive accumulation ability in the tumor, albumin binding moieties such as cysteine³⁴ or fatty acids are adopted to overcome limitations of conventional drugs, for example, low targeting efficiency and specificity [40].

Small peptide sequence could also be a good functional moiety to improve systemic efficiency of prodrugs with inducing self-assemble. For example, hydrophobic phenylalanine could be self-assembled due to its π - π stacking induced hydrophobic interaction [20]. Formation of nanoparticles due to phenylalanine interaction have

enhanced tumor targeting efficiency by EPR (enhanced permeability and retention) effect.

RGD (Arg-Gly-Asp) peptide is a popular ligand that bound to the integrin $\alpha V\beta 3$ receptor. The integrin $\alpha V\beta 3$ receptor is also known as overexpressed in cancer, it is used for increasing tumor targeting efficiency of prodrug. This strategy is introduced to doxorubicin with caspase-3 cleavable peptide reported in previous chapter [25].

Light triggered prodrugs are developed for photodynamic therapy (PDT). While light irradiated to prodrugs, conjugated photosensitizers such as Ce6 or verteporfin convert oxygen into reactive singlet oxygen which cause cell apoptosis [41]. Cell apoptosis locally by singlet oxygen induce typical enzyme release which can cleave specific peptides to discharge free anticancer agents [42]. Additionally, several photosensitizers could be in hydrophobic interaction which can self-assembled to nanoparticles for enhanced tumor targeting efficiency.

1.4. Research Rationale

Despite the development of next-generation anticancer agents, first-line chemotherapy is considered the preferred treatment due to its versatility and utility. However, there are still challenges about side effects, and much research have been in trouble to overcome these limitations.

This study was conducted to minimize the side effects while maintaining the effects of conventional anticancer agents. Cancer cell overexpressed enzyme cleavable linkers were used for enhanced cancer specificity and various functional moieties were

introduced for increasing tumor targeting efficiency. As previously reported, there are various types of linkers for modifying conventional drugs to prodrugs. Among these linkers, ester bond and Arg-Arg (RR) peptide were used to compose cancer-specific prodrugs. Additionally, functional moieties for improvement of targeting efficiency were adopted. Maleimide group or phenylalanine were used, which could bound to serum albumin or could self-assembled to nanoparticles.

Through this study, various combinations composed of conventional drugs, linkers and functional moieties could be suggested appropriately for various cancer types. In addition, in the case of PROTAC which was used in the last chapter could induce PD-L1 regression by degradation of BRD4 which has significant role for transcription of PD-L1 oncogene. Thus, it could be possible for additional immunotherapy. Therefore, this study could be important development of next-generation anticancer agents.

1.5. References

1. Luo, D.D., et al., Chemophototherapy: An Emerging Treatment Option for Solid Tumors. *Advanced Science*, 2017. 4(1).
2. Tacar, O., P. Sriamornsak, and C.R. Dass, Doxorubicin: an update on anticancer molecular action, toxicity and novel drug delivery systems. *Journal of Pharmacy and Pharmacology*, 2013. 65(2): p. 157-170.
3. Petru, E. and D. Schmähl, Cytotoxic chemotherapy-induced second primary neoplasms: clinical aspects. *Neoplasma*, 1991. 38(2): p. 147-155.
4. Green, M.R., et al., Abraxane®, a novel Cremophor®-free, albumin-bound

- particle form of paclitaxel for the treatment of advanced non-small-cell lung cancer. *Annals of Oncology*, 2006. 17(8): p. 1263-1268.
5. Barenholz, Y., Doxil® — The first FDA-approved nano-drug: Lessons learned. *Journal of Controlled Release*, 2012. 160(2): p. 117-134.
 6. Abramson, J.S., et al., ADCs, BiTEs, CARs, and Small Molecules: A New Era of Targeted Therapy in Non-Hodgkin Lymphoma. *American Society of Clinical Oncology Educational Book*, 2020(40): p. 302-313.
 7. Sharma, A. and U.S. Sharma, Liposomes in drug delivery: Progress and limitations. *International Journal of Pharmaceutics*, 1997. 154(2): p. 123-140.
 8. Lim, S., et al., Recent advances and challenges of repurposing nanoparticle-based drug delivery systems to enhance cancer immunotherapy. *Theranostics*, 2019. 9(25): p. 7906-7923
 9. Joubert, N., et al. Antibody–Drug Conjugates: The Last Decade. *Pharmaceutics*, 2020. **13**, DOI: 10.3390/ph13090245.
 10. Cahill, D.P., et al., Genetic instability and darwinian selection in tumours (Reprinted from *Trends in Biochemical Science*, vol 12, Dec., 1999). *Trends in Cell Biology*, 1999. 9(12): p. M57-M60.
 11. Bedard, P.L., et al., Tumour heterogeneity in the clinic. *Nature*, 2013. 501(7467): p. 355-364.
 12. Marusyk, A., V. Almendro, and K. Polyak, Intra-tumour heterogeneity: a looking glass for cancer? *Nature Reviews Cancer*, 2012. 12(5): p. 323-334.
 13. Weyel, D., et al., Secreted human beta-glucuronidase: a novel tool for gene-directed enzyme prodrug therapy. *Gene Therapy*, 2000. 7(3): p. 224-231.
 14. Lee, M.H., et al., Fluorogenic reaction-based prodrug conjugates as targeted

- cancer theranostics. *Chemical Society Reviews*, 2018. 47(1): p. 28-52.
15. Mu, J., et al., Development of endogenous enzyme-responsive nanomaterials for theranostics. *Chemical Society Reviews*, 2018. 47(15): p. 5554-5573.
 16. Alizadeh, A.A., et al., Toward understanding and exploiting tumor heterogeneity. *Nature Medicine*, 2015. 21(8): p. 846-853.
 17. Gocheva, V. and J.A. Joyce, Cysteine Cathepsins and the cutting edge of cancer invasion. *Cell Cycle*, 2007. 6(1): p. 60-64.
 18. Kryczka, J., et al., Cathepsin B Is Upregulated and Mediates ECM Degradation in Colon Adenocarcinoma HT29 Cells Overexpressing Snail. *Cells*, 2019. 8(3).
 19. Cai, H., et al., Stimuli-Sensitive Linear–Dendritic Block Copolymer–Drug Prodrug as a Nanoplatfrom for Tumor Combination Therapy. *Advanced Materials*, 2022. 34(8): p. 2108049.
 20. Shim, M.K., et al., Carrier-free nanoparticles of cathepsin B-cleavable peptide-conjugated doxorubicin prodrug for cancer targeting therapy. *Journal of Controlled Release*, 2019. 294: p. 376-389.
 21. Aranda, J., et al., The Catalytic Mechanism of Carboxylesterases: A Computational Study. *Biochemistry*, 2014. 53(36): p. 5820-5829.
 22. Ross, M.K. and J.A. Crow, Human Carboxylesterases and their role in xenobiotic and endobiotic metabolism. *Journal of Biochemical and Molecular Toxicology*, 2007. 21(4): p. 187-196.
 23. Wang, D.D., et al., Human carboxylesterases: a comprehensive review. *Acta Pharmaceutica Sinica B*, 2018. 8(5): p. 699-712.
 24. Kunimoto, T., et al., Antitumor Activity of 7-Ethyl-10-[4-(1-piperidino)-1-

- piperidino]carbonyloxycamptothecin, a Novel Water-soluble Derivative of Camptothecin, against Murine Tumors¹. *Cancer Research*, 1987. 47(22): p. 5944-5947.
25. Chung, S.W., et al., Self-Triggered Apoptosis Enzyme Prodrug Therapy (STAEPT): Enhancing Targeted Therapies via Recurrent Bystander Killing Effect by Exploiting Caspase-Cleavable Linker. *Advanced Science*, 2018. 5(7).
 26. Lee, B.S., et al., Induced Phenotype Targeted Therapy: Radiation-Induced Apoptosis-Targeted Chemotherapy. *Jnci-Journal of the National Cancer Institute*, 2015. 107(2).
 27. Xu, G. and H.L. McLeod, Strategies for enzyme/prodrug cancer therapy. *Clinical Cancer Research*, 2001. 7(11): p. 3314-3324.
 28. Chung, S.W., et al., Albumin-binding caspase-cleavable prodrug that is selectively activated in radiation exposed local tumor. *Biomaterials*, 2016. 94: p. 1-8.
 29. Van Lint, P. and C. Libert, Chemokine and cytokine processing by matrix metalloproteinases and its effect on leukocyte migration and inflammation. *Journal of Leukocyte Biology*, 2007. 82(6): p. 1375-1381.
 30. Gialeli, C., A.D. Theocharis, and N.K. Karamanos, Roles of matrix metalloproteinases in cancer progression and their pharmacological targeting. *Febs Journal*, 2011. 278(1): p. 16-27.
 31. Chau, Y., et al., Antitumor efficacy of a novel polymer-peptide-drug conjugate in human tumor xenograft models. *International Journal of Cancer*, 2006. 118(6): p. 1519-1526.

32. Huang, C.J., et al., Controlled release strategy of paclitaxel by conjugating to matrix metalloproteinases-2 sensitive peptide. *Oncotarget*, 2016. 7(32): p. 52230-52238.
33. Shi, N.Q., et al., Enhancing cellular uptake of activable cell-penetrating peptide-doxorubicin conjugate by enzymatic cleavage. *International Journal of Nanomedicine*, 2012. 7: p. 1613-1621.
34. Lee, G.Y., et al., MMPs-specific PEGylated peptide-DOX conjugate micelles that can contain free doxorubicin. *European Journal of Pharmaceutics and Biopharmaceutics*, 2007. 67(3): p. 646-654.
35. Chau, Y., F.E. Tan, and R. Langer, Synthesis and characterization of dextran-peptide-methotrexate conjugates for tumor targeting via mediation by matrix metalloproteinase II and matrix metalloproteinase IX. *Bioconjugate Chemistry*, 2004. 15(4): p. 931-941.
36. Jiang, J., et al., Combretastatin A4 Nanodrug-Induced MMP9 Amplification Boosts Tumor-Selective Release of Doxorubicin Prodrug. *Advanced Materials*, 2019. 31(44).
37. Gao, A., et al., Sheddable Prodrug Vesicles Combating Adaptive Immune Resistance for Improved Photodynamic Immunotherapy of Cancer. *Nano Letters*, 2020. 20(1): p. 353-362.
38. Mita, M.M., et al., Pharmacokinetic study of aldorubicin in patients with solid tumors. *Investigational New Drugs*, 2015. 33(2): p. 341-348.
39. Um, W., et al., A Comparative Study on Albumin-Binding Molecules for Targeted Tumor Delivery through Covalent and Noncovalent Approach. *Bioconjugate Chemistry*, 2019. 30(12): p. 3107-3118.

40. Hyun, H., et al., Surface modification of polymer nanoparticles with native albumin for enhancing drug delivery to solid tumors. *Biomaterials*, 2018. 180: p. 206-224.
41. Kessel, D., Apoptosis and associated phenomena as a determinants of the efficacy of photodynamic therapy. *Photochemical & Photobiological Sciences*, 2015. 14(8): p. 1397-1402.
42. Um, W., et al., Visible light-induced apoptosis activatable nanoparticles of photosensitizer-DEVD-anticancer drug conjugate for targeted cancer therapy. *Biomaterials*, 2019. 224.

Chapter 2. Tumor-specific monomethyl auristatin E (MMAE) prodrug nanoparticles for safe and effective chemotherapy

2.1. Introduction

Chemotherapy is still the most common approach for anticancer treatment owing to its considerable antitumor efficacy by high sensitivity in the broad spectrum of cancer types [1]. However, anticancer drugs are often accompanied by severe side effects during treatment because of their low tumor selectivity, which restricts drug dosage in vivo, resulting in treatment failure by limiting the tumors from being exposed to sufficient drug concentrations [2, 3]. As a promising approach to improve the tumor selectivity of anticancer drugs, the prodrug is a bioreversible medication that is specifically converted to the active drug by chemical or enzymatic transformation in the tumor microenvironment, which can considerably reduce the chemotherapy-induced side effects [4, 5]. Importantly, tumor tissues show significantly different characteristics in comparison to normal tissues, including high reactive oxygen species (ROS), elevated/low pH, and hypoxia condition [6]. In particular, the overexpression of several enzymes, including cathepsins, caspases, and matrix metalloproteinases (MMPs), is observed within the tumor microenvironment compared to normal tissues [7-10]. Thus, designed prodrugs releasing active drugs selectively by those overexpressed enzymes in the tumor microenvironment have been proposed to increase the safety of chemotherapy [11-13]. However, prodrug strategies usually have low antitumor

efficacy compared to parent drugs by delayed drug release because they need time to be activated by enzymatic cleavage and also cannot be fully recovered to the active drugs [14]. Therefore, highly potent anticancer drug should be considered for development utilizing the prodrug system to expect a sufficient antitumor efficacy for tumor treatment.

Monomethyl auristatin E (MMAE), a synthetic analog of the natural product dolastatin 10, is a potent antimitotic agent that inhibits tubulin polymerization [15]. Even with the 100 - 1000 times more potent antitumor efficacy than doxorubicin, the clinical use of MMAE has been strictly hindered owing to the severe toxicity [3]. Hence, many researchers have developed antibody-drug conjugates (ADCs) integrating prodrug system by using MMAE; this is to reduce the severe toxicity of MMAE via prodrug strategy, and to further enhance the tumor selectivity by antibody-mediated active targeting against receptors specifically overexpressed in tumor cells compared to normal cells [16, 17]. For instance, cAC10-vcMMAE, constructed with anti-CD30 monoclonal antibody (cAC10), cathepsin B-specific cleavable valine-citrulline (VC) dipeptide linker, and MMAE, has shown highly selective therapy for the tumor treatment with minimized toxicity [18]. However, ADCs typically carry one to four of anticancer drug molecules per antibody, and thus drug loading capacity is determined to be 1–4% in terms of molecular weight, which limit the antitumor efficacy. In addition, their complex synthetic chemistry hindering industrial scale manufacturing is a formidable challenge for clinical translation. In addition, there were also several approaches to prepare MMAE modified with cytokines or peptides for superior antitumor efficacy, but their clinical use was strictly hindered owing to severe MMAE-related toxicities [19-21].

Here, I propose tumor-specific MMAE prodrug nanoparticles for safe and effective chemotherapy. The MMAE is chemically conjugated with the cathepsin B-cleavable FRRG (Phe-Arg-Arg-Gly) peptide via simple one step synthetic chemistry, resulting in FRRG-MMAE (Figure 2.1a). The FRRG sequence is a substrate for the cathepsin B, which is a promising cancer biomarker overexpressed specifically in tumor cells compared to normal cells. Moreover, they efficiently release the active drug by sequential cleavage mechanisms by which -RR- sequences are firstly cleaved by cathepsin B, and the released glycine (G)-conjugated drug is subsequently metabolized into the free drug by intracellular proteases [22-28]. The target enzyme specificity of FRRG sequence was confirmed by assessing reduced antitumor efficacy of the doxorubicin when they were conjugated with scrambled FGRG peptide instead of FRRG peptide. FGRG-conjugated doxorubicin formed stable nanoparticles similar with FRRG-conjugated doxorubicin, but they showed no cytotoxicity owing to the absence of enzyme-specific cleavage mechanism. Most importantly, FRRG-MMAE self-assembled into stable nanoparticles without any additional carrier materials by hydrophobic interaction-derived aggregations [29]. This novel carrier-free nanoparticle system has ultra-high drug loading capacity (>50%) and favorable synthetic protocol for large-scale production, and reduces the potential toxicity by carrier materials, compared to conventional nanoparticles that physically encapsulates the anticancer drugs. When the FRRG-MMAE nanoparticles are intravenously injected into the breast tumor-bearing mice, they efficiently accumulate within the tumor tissues by enhanced permeability and retention (EPR) effect and release free MMAE by cathepsin B overexpressed in tumor cells (Figure 2.1b). The released MMAE molecules inhibit the tubulin polymerization in the tumor cells, resulting in significant cell death. In contrast,

FRRG-MMAE nanoparticles, which are non-specifically accumulated in the normal tissues, maintain an inactive state owing to the innately low cathepsin B expression in the normal cells, minimizing the MMAE-related severe toxicity (Figure 2.1c). In this chapter, the physicochemical characterization of FRRG-MMAE nanoparticles, and their intracellular behavior and cytotoxicity in tumor or normal cells are investigated. In addition, the safe and effective chemotherapy by FRRG-MMAE nanoparticles is evaluated in the breast tumor-bearing mice.

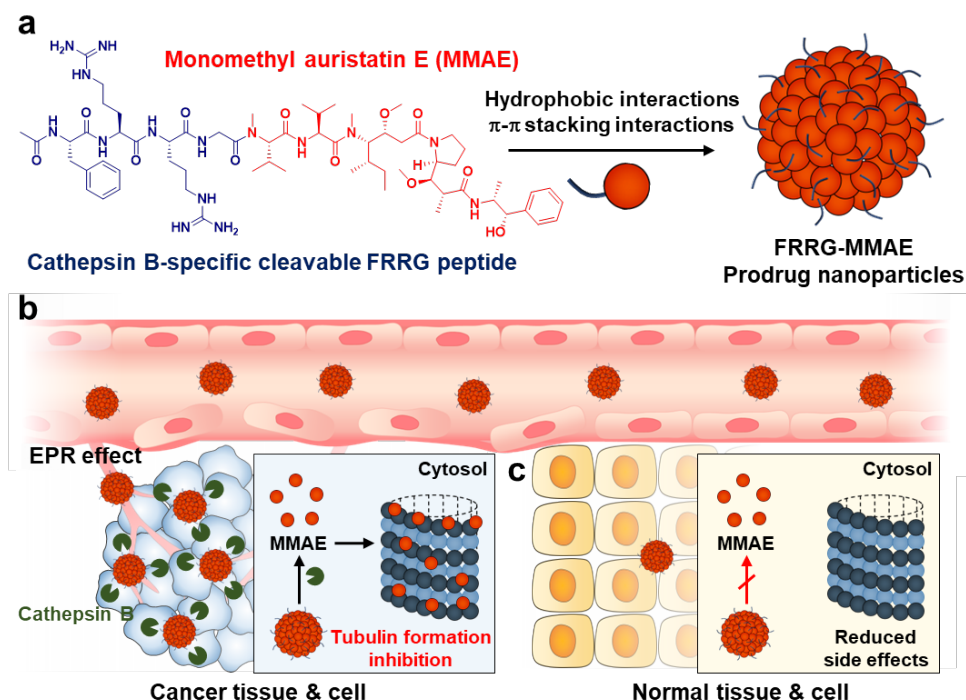


Figure 2.1. (a) The FRRG (Phe-Arg-Arg-Gly) peptide is conjugated to MMAE. The synthesized FRRG-MMAE self-assembled into nanoparticles by hydrophobic interaction without additional materials. (b) When the FRRG-MMAE nanoparticles are intravenously injected into the breast tumor models, they efficiently accumulate within the tumor tissues owing to the enhanced permeability and retention (EPR) effect and specifically release free MMAE by cathepsin B overexpressed in tumor cells. The released MMAE inhibits the tubulin polymerization in the tumor cells, resulting in significant cell death. (c) In contrast, FRRG-MMAE nanoparticles, which are non-specifically accumulated in the normal tissues, maintain inactive state owing to the innately low cathepsin B expression in the normal cells, minimizing the MMAE-related severe toxicity.

2.2. Materials and Methods

2.2.1 Materials

N-terminal acylated FRRG (Ac-Phe-Arg-Arg-Gly-COOH) and FRRG (NH₂-Phe-Arg-Arg-Gly-COOH) peptides were purchased from Peptron (Daejeon, Korea). Monomethyl auristatin E (MMAE) was purchased from MedChemExpress (Monmouth Junction, NJ, USA). *N,N*-Dimethylformamide (DMF), HATU, 1-ethyl-3-(3-dimethylaminopropyl)carbodiimide (EDC), *N,N*-diisopropylethylamine (DIPEA) and *N*-hydroxysuccinimide (NHS) were purchased from Sigma Aldrich (St. Louis, MO, USA). TUNEL assay kit and cathepsin B enzyme were purchased from R&D systems (Minneapolis, MN, USA). CellLight™ Lysosomes-RFP, Bac-Mam 2.0 was purchased from Thermo Fisher Scientific Inc. (Rockford, IL, USA). TEM grid (Carbon Film 200 Mesh copper) was purchased from Electron Microscopy Sciences (Atlanta, GA, USA). DMEM media, fetal bovine serum (FBS), penicillin, and streptomycin were purchased from WELGENE Inc. (Daegu, Korea). The 4T1 (murine breast adenocarcinoma) and H9C2 (rat BDIX heart myoblast) cells were purchased from ATCC (American Type Culture Collection; Manassas, VA, USA).

2.2.2. Preparation and Characterization of FRRG-MMAE Nanoparticles

To prepare tumor-specific MMAE prodrug, the cathepsin B-specific cleavable FRRG (Phe-Arg-Arg-Gly) peptide was conjugated to the MMAE through HATU one-step reaction. Briefly, FRRG peptide (200 mg, 1 eq), MMAE (219 mg, 1 eq), HATU (232 mg, 2 eq) and DIPEA (2 eq) were dissolved in 10 mL DMF, followed by stirring at 37 °C for 24 h. Then, FRRG-MMAE was purified using reverse-phase high

performance liquid chromatography (RP-HPLC; Agilent 1200 Series HPLC System, Santa Clara, CA, USA). The purity and exact molecular weight of FRRG-MMAE were characterized by RP-HPLC and matrix-assisted laser desorption/ionization time of flight (MALDI-TOF, AB Sciex TOF/TOF 5800 System, USA) mass spectrometer, respectively. The size distribution and particle morphology of FRRG-MMAE nanoparticles (1 mg/mL in saline) were analyzed using Zetasizer Nano ZS (Malvern Instruments, Worcestershire, UK) and transmission electron microscopy (TEM, CM-200, Philips, Bentonville, AR, USA), respectively. To assess the cathepsin B-specific cleavage of FRRG-MMAE nanoparticles, they were incubated with enzyme reaction buffer (MES buffer) containing 10 µg cathepsin B enzyme at 37 °C.

2.2.3. Cellular Uptake

The cellular uptake of FRRG-MMAE nanoparticles was assessed in the 4T1 cells. Briefly, 1×10^5 4T1 cells were seeded in the confocal dishes, followed by incubation with FRRG-MMAE (1 nM) at 37 °C. The tubulin formation after FRRG-MMAE nanoparticles or free MMAE treatments were visualized by staining with Cy5.5 fluorescent dye-conjugated anti-tubulin antibody for 24 h at 4 °C. Then, cells were fixed with 4% paraformaldehyde fixative for 25 min, and stained with DAPI solution (Invitrogen, Carlsbad, CA, USA) for 15 min in the dark. Finally, the 4T1 cells were observed using a confocal laser scanning microscope (CLSM) equipped with 405 diode (405 nm) and HeNe-Red (633 nm) lasers (Leica, Wetzlar, Germany).

2.2.4. Cytotoxicity Study

The cytotoxicity of FRRG-MMAE nanoparticles was assessed by cell counting kit-8 (CCK-8) assays. First, 3×10^3 4T1 or H9C2 cells were seeded in the 96-well cell culture plates. Then, the FRRG-MMAE nanoparticles or free MMAE were incubation with the cells for 24 h, followed by additional incubation with cell culture medium containing CCK-8 (10%) for 10 min. Finally, the cell viability of each cell was measured using a microplate reader with 450 nm of wavelength (VERSAmax™; Molecular Devices Corp., San Jose, CA, USA).

2.2.5. Antitumor Efficacy and Toxicity Study of FRRG-MMAE Nanoparticles in Breast Tumor Models

The antitumor efficacy was evaluated in the breast tumor models. The breast tumor models were prepared via subcutaneous injection of 1×10^6 4T1 cells. When the tumor volumes were approximately 80 mm³, mice were divided into three groups: (i) saline; (ii) MMAE (1 mg/kg); and (iii) FRRG-MMAE nanoparticles (equivalent dose of 1 mg/kg based on MMAE contents). The mice were treated once every three days, and tumor volumes were calculated as the smallest diameter² \times largest diameter \times 0.53. The mice with a tumor volume of 2000 mm³ or larger were counted as dead. The toxicity study of FRRG-MMAE nanoparticles was assessed via histology. The major organs were collected from mice on day 5 after treatments, and structural abnormality in the organ tissues was assessed by staining with H&E.

2.2.6. Statistics

The statistical significance between two groups was analyzed using Student's t-test. One-way analysis of variance (ANOVA) was performed for comparisons of more than two groups, and multiple comparisons were analyzed using the Tukey–Kramer post hoc test. Survival data were plotted as Kaplan–Meier curves and analyzed using the log-rank test. The statistical significance was indicated with asterisks (* $p < 0.05$, ** $p < 0.01$, *** $p < 0.001$) in the figures.

2.3. Results

2.3.1. Preparation and Characterization of FRRG-MMAE Nanoparticles

The tumor-specific MMAE prodrug nanoparticles, FRRG-MMAE, constructed with cathepsin B-specific cleavable FRRG (Phe-Arg-Arg-Gly) peptide and MMAE, were designed to reduce the severe MMAE-related toxicity and to enhance their antitumor efficacy. The MMAE was chemically conjugated to the C-terminus of the FRRG peptide via one step HATU reaction (Figure 2.2a). After the preparation, 99.9% of FRRG-MMAE was purified with HPLC (Figure 2.2b). The successful synthesis was also confirmed using the MALDI-TOF mass spectrometer. The exact molecular weight of FRRG-MMAE was calculated to be 1276.64 Da for $C_{64}H_{105}N_{15}O_{12}$, and measured to be 1276.7 m/z [M] and 1299.07 [M+Na] (Figure 2.2c).

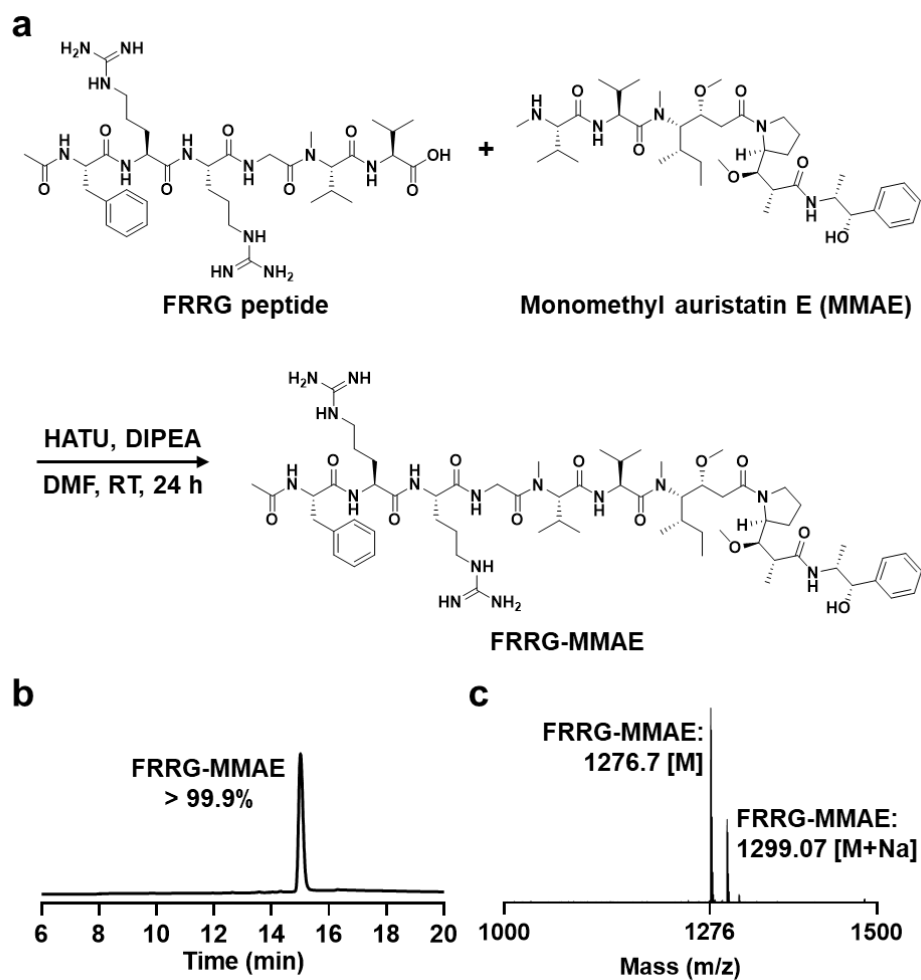


Figure 2.2. Preparation of FRRG-MMAE nanoparticles. (a) Synthetic route for preparation of tumorspecific monomethyl auristatin E (MMAE) prodrug nanoparticles, FRRG-MMAE. The (b) purity and (c) molecular weight of FRRG-MMAE after preparation.

Importantly, FRRG-MMAE molecules self-assembled into about 200 nm-sized spherical nanoparticles in aqueous condition without any additional carrier materials (Figure 2.3). In addition, FRRG-MMAE nanoparticles were highly stable in the mouse plasma of physiological condition without significant changes of the particle size (Figure 2.4). These stable structures with around 200 nm are suitable to accumulate within the tumor tissues via EPR effect [30]. The mechanism for the self-assembly of FRRG-MMAE molecules were assessed via molecular dynamic (MD) simulation. The MD simulation results of one FRRG-MMAE molecule showed the amphiphilic characteristics due to the positively charged polar arginine sequences (blue color) and neutrally charged non-polar MMAE molecules (Figures 2.5). In addition, MD simulation results of two FRRG-MMAE molecules indicated that MMAE in each FRRG-MMAE maintain a close distance for 20 ns (Figure 2.6), whereas the distance between two FRRG (without MMAE) molecules became distant because of electrostatic repulsion in the side chains (Figures 2.7). Similar results were also observed in the MD simulation results, which are performed with ten FRRG-MMAE molecules (Figure 2.8). As a result, the ratio of overlap surface over total surface areas of the FRRG-MMAE molecules was sustainably maintained, while that of the FRRG peptide converged to zero (Figure 2.9). These results clearly demonstrate that the self-assembly mechanism of FRRG-MMAE molecules are hydrophobic interactions due to the MMAE molecules [29]. Next, the target-enzyme specificity of FRRG-MMAE nanoparticles was evaluated by incubation with cathepsin B. When the FRRG-MMAE nanoparticles were incubated with cathepsin B in the MES buffer (pH 5.5), they began to release the glycine-conjugated MMAE (G-MMAE) from 1 h of incubation (Figure 2.10). In addition, over 90% of FRRG-MMAE nanoparticles cleaved to G-MMAE after

3 h of incubation and eventually fully cleaved 6 h post-incubation. This result was supported by MALDI-TOF analysis, which verify the exact molecular weight of G-MMAE (calculated mass: 775.58 Da, measured mass: 775.8 m/z [M], 798.1 [M+Na], and 814.4 [M+K]) at a newly appeared characteristics peak in the HPLC spectrum (approximately 13 min) after incubation of FRRG-MMAE nanoparticles with cathepsin B (Figure 2.11). It was previously studied that glycine (G)-conjugated drug is subsequently metabolized into the free drug by intracellular proteases [14]. Taken together, these results demonstrate that FRRG-MMAE nanoparticles offer simple synthetic chemistry for industrial-scale manufacturing and form stable nanoparticles that specifically release MMAE molecules by cathepsin B-mediated enzymatic cleavage.

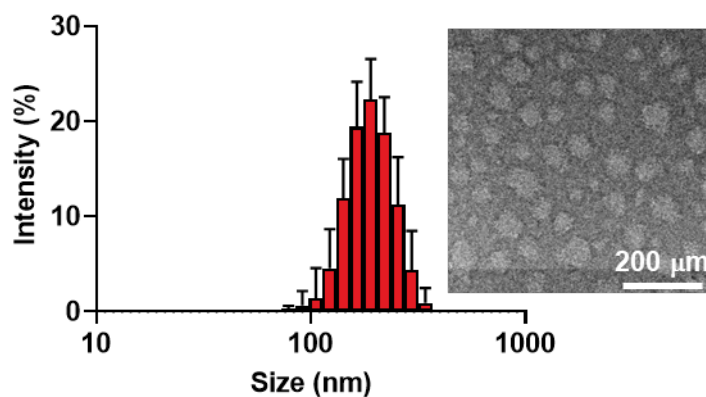


Figure 2.3. Size distribution and morphology of FRRG-MMAE nanoparticles for structural characterization.

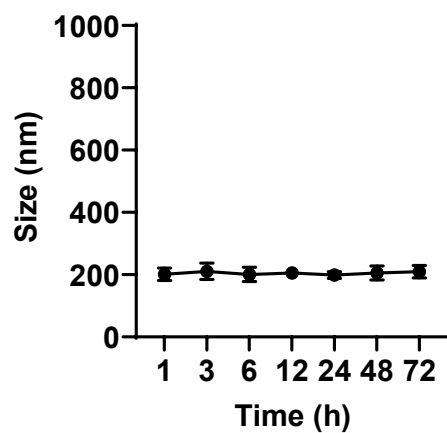


Figure 2.4. The stability of FRRG-MMAE nanoparticles in mouse serum.

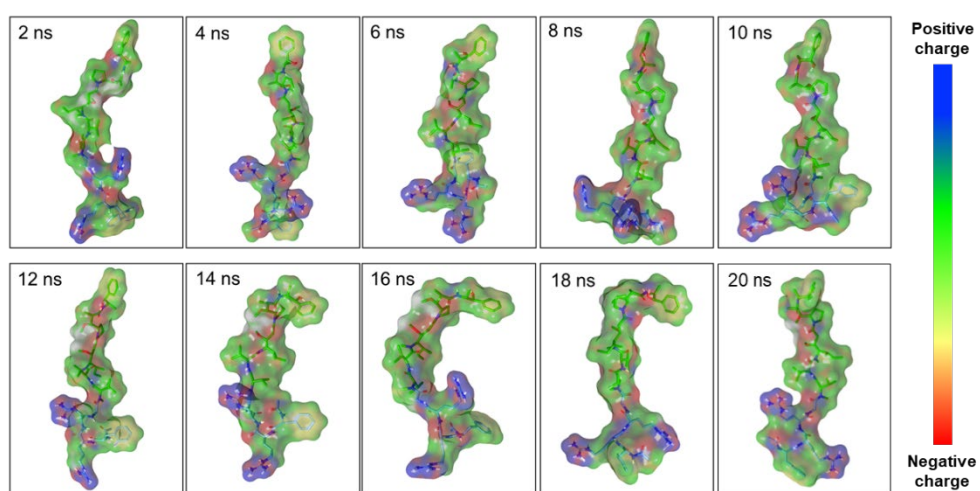


Figure 2.5. Molecular dynamic (MD) simulation of one FRRG-MMAE molecule for 20 ns.

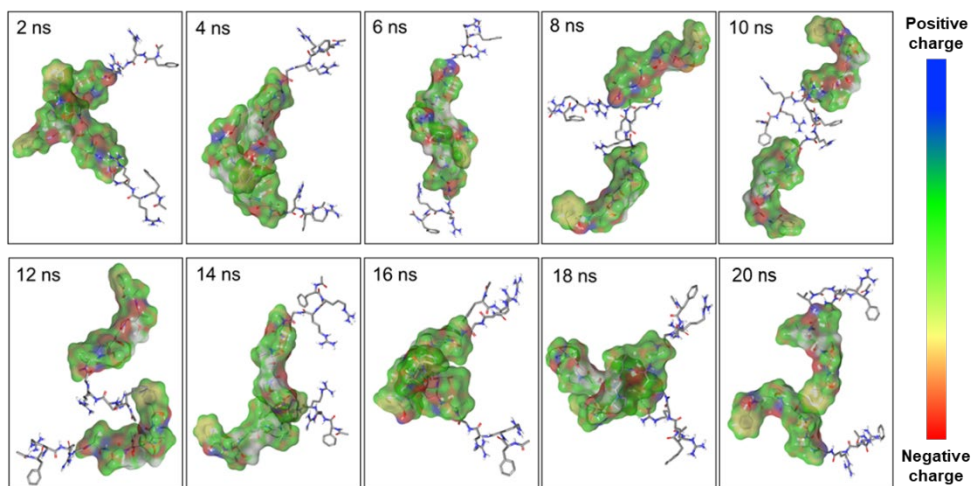


Figure 2.6. MD simulation of two FRRG-MMAE molecules for 20 ns.

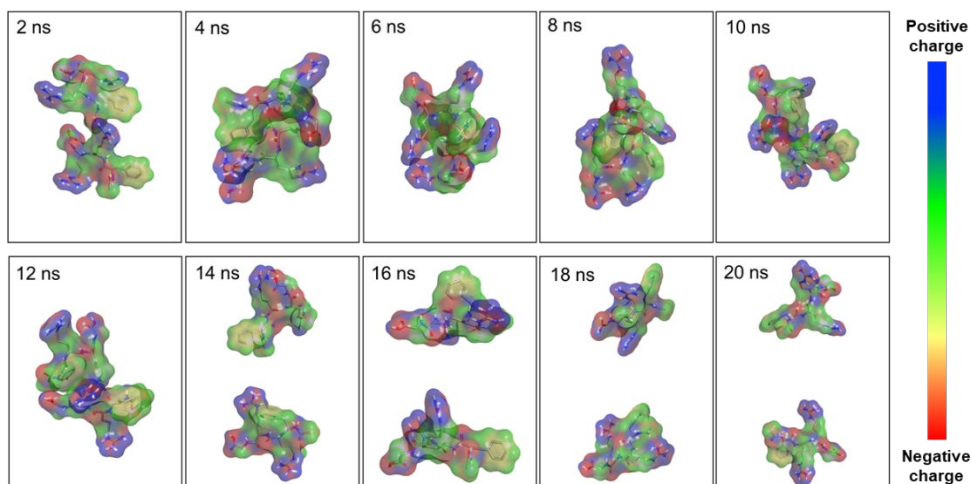


Figure 2.7. MD simulation of two FRRG peptide molecules for 20 ns.

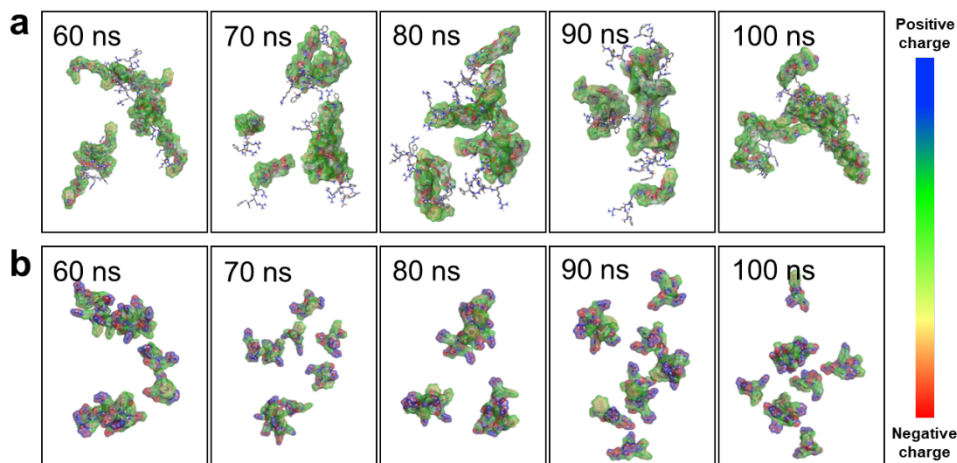


Figure 2.8. MD simulation of ten molecules of (a) FRRG-MMAE or (b) FRRG peptide. The system was fully relaxed for 50 ns due to large number of molecules, and the snapshot images from 50 to 100 ns in simulation time were used. The images showed that the aggregation was driven by the intermolecular interaction in MMAE segments, whereas the FRRG peptides were separated without significant aggregations.

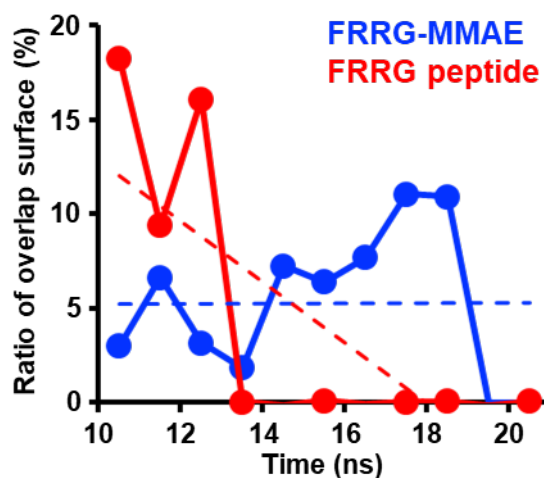


Figure 2.9. The ratio of overlap surface over total surface areas of the FRRG-MMAE of FRRG peptide molecules.

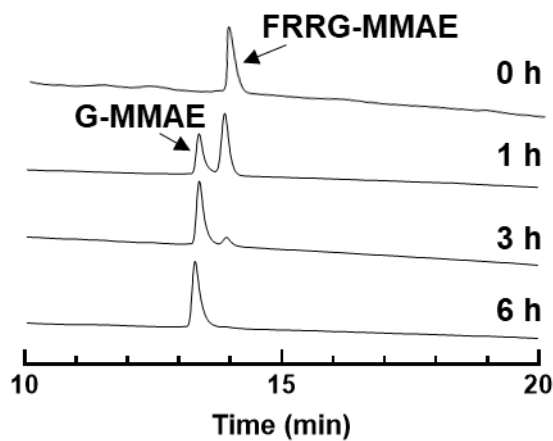


Figure 2.10. Enzymatic cleavage assays of FRRG-MMAE nanoparticles after incubation with cathepsin B.

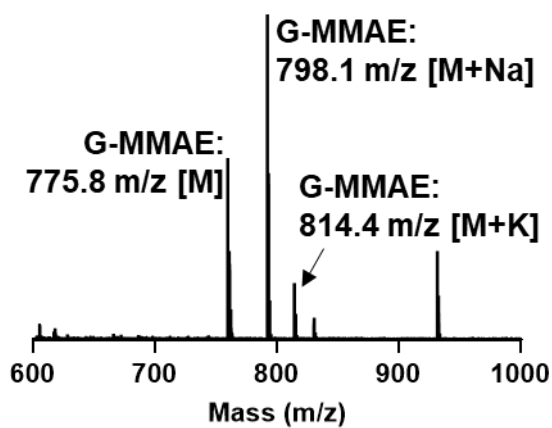


Figure 2.11. Metabolite assay of FRRG-MMAE nanoparticles after incubation with cathepsin B.

2.3.2. Cellular Uptake and Tumor Cell Selective Cytotoxicity of FRRG-MMAE Nanoparticles

The cellular uptake of FRRG-MMAE nanoparticles was assessed in the murine breast carcinoma (4T1) cells. For the efficient monitoring, FRRG-MMAE nanoparticles containing 10% of FITC Fluorescent dye-conjugated FRRG-MMAE were used in the experiments. When the 4T1 cells were treated with FRRG-MMAE nanoparticles (1 nM) at 37 °C, a robust uptake was clearly observed, wherein the FITC fluorescence signals of nanoparticles were gradually increased cells in the with an incubation time-dependent manner (Figure 2.12a). I also observed strong co-localization of FRRG-MMAE nanoparticles with lysosomes in the 4T1 cells after 24 h of incubation (Figure 2.12b). These results clearly indicate that FRRG-MMAE nanoparticles internalize in the cells via the nanoparticle-derived endosomal-lysosomal endocytosis mechanism. Next, the selective MMAE release of FRRG-MMAE nanoparticles by cathepsin B was evaluated in 4T1 cells and rat BDIX cardiomyocytes (H9C2). This is because 4T1 cells express significantly high levels (32.48 ± 3.14 -fold) of cathepsin B than H9C2 cells [26]. The tubulin formation in the 4T1 cells was significantly inhibited after 24 h of treatment with free MMAE or FRRG-MMAE nanoparticles compared to naïve cells (Figure 2.13a). Importantly, the effect to inhibit tubulin formation in the cells of free MMAE was similar in the H9C2 and 4T1 cells, whereas FRRG-MMAE nanoparticle-treated H9C2 cells showed similar tubulin formation with naïve cells (Figure 2.13b). These results indicate that FRRG-MMAE nanoparticles inhibit tubulin polymerization by releasing MMAE molecules owing to the overexpressed cathepsin B in the tumor cells, but they maintain inactive states in the cathepsin B-deficient normal cells. In agreement with these results, the IC₅₀ value

of FRRG-MMAE nanoparticles in the 4T1 cells was measured to be 9.87 nM after 72 h incubation, while it was 70.81 nM in the H9C2 cells, which showed an approximately seven-fold difference, indicating tumor cell selective cytotoxicity (Figure 2.14a). In contrast, free MMAE showed indiscriminate cytotoxicity in both cells with nearly similar IC₅₀ values (Figure 2.14b). These results indicate that FRRG-MMAE nanoparticles can efficiently eradicate the tumors with reduced MMAE-related severe toxicity toward normal tissues by tumor cell selective cytotoxicity.

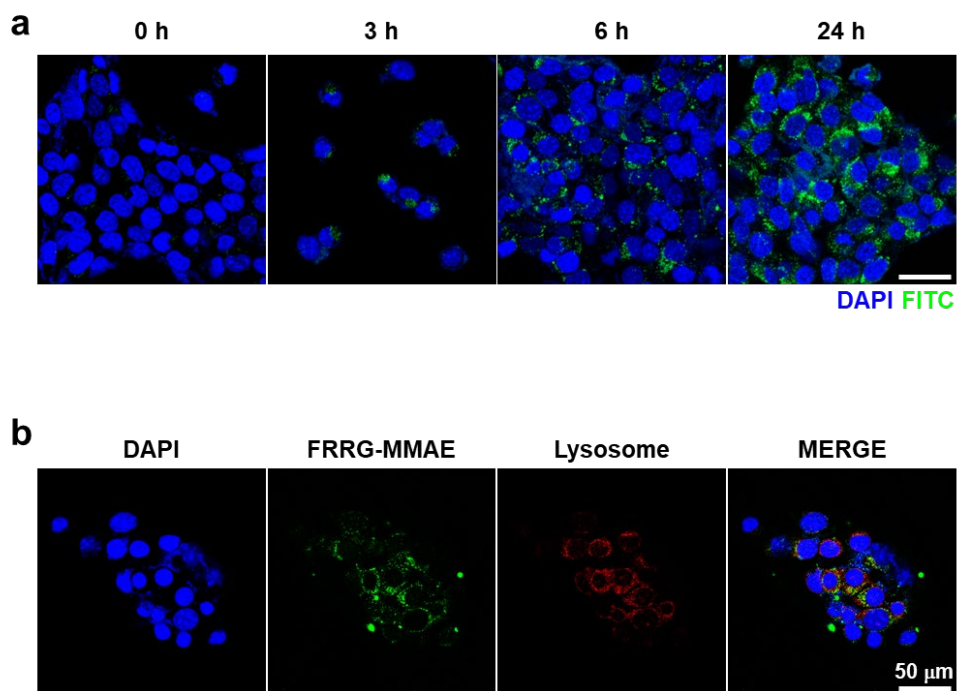


Figure 2.12. (a) Cellular uptake of FRRG-MMAE nanoparticles in 4T1 cells. (b) Co-localization of FRRG-MMAE nanoparticles and lysosomes in 4T1 cells.

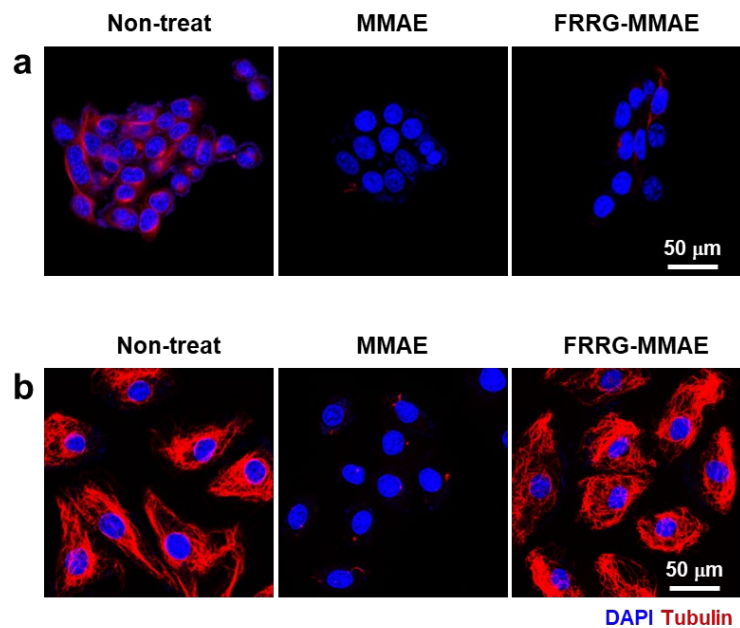


Figure 2.13. The tubulin formation of (a) 4T1 and (b) H9C2 cells after treatment with free MMAE or FRRG-MMAE.

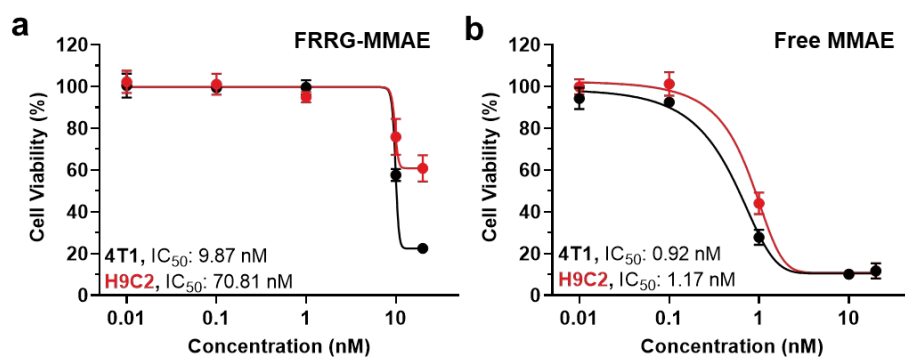


Figure 2.14. The cell viability of 4T1 and H9C2 cells after treatment with (a) FRRG-MMAE or (b) free MMAE.

2.3.3. Antitumor Efficacy and Safety of FRRG-MMAE Nanoparticles in Breast Tumor-Bearing Mice

The high tumor targeting of FRRG-MMAE nanoparticles via the EPR effect was assessed in the breast tumor-bearing mice that were established by subcutaneous inoculation of 4T1 cells into the flank of the BALB/C mice. Fluorescent dye Cy5.5-conjugated free MMAE or FRRG-MMAE with an equivalent dose of 1 mg/kg of MMAE content were intravenously injected in the mice. The NIRF images of the 4T1 tumor-bearing mice showed that a significantly higher number of FRRG-MMAE nanoparticles was accumulated in the targeted tumor tissues compared to free MMAE (Figure 2.15a). Quantitatively, a 2.98 - 3.01-fold higher number of FRRG-MMAE nanoparticles accumulated within the tumor tissues compared to free MMAE (Figure 2.15b).

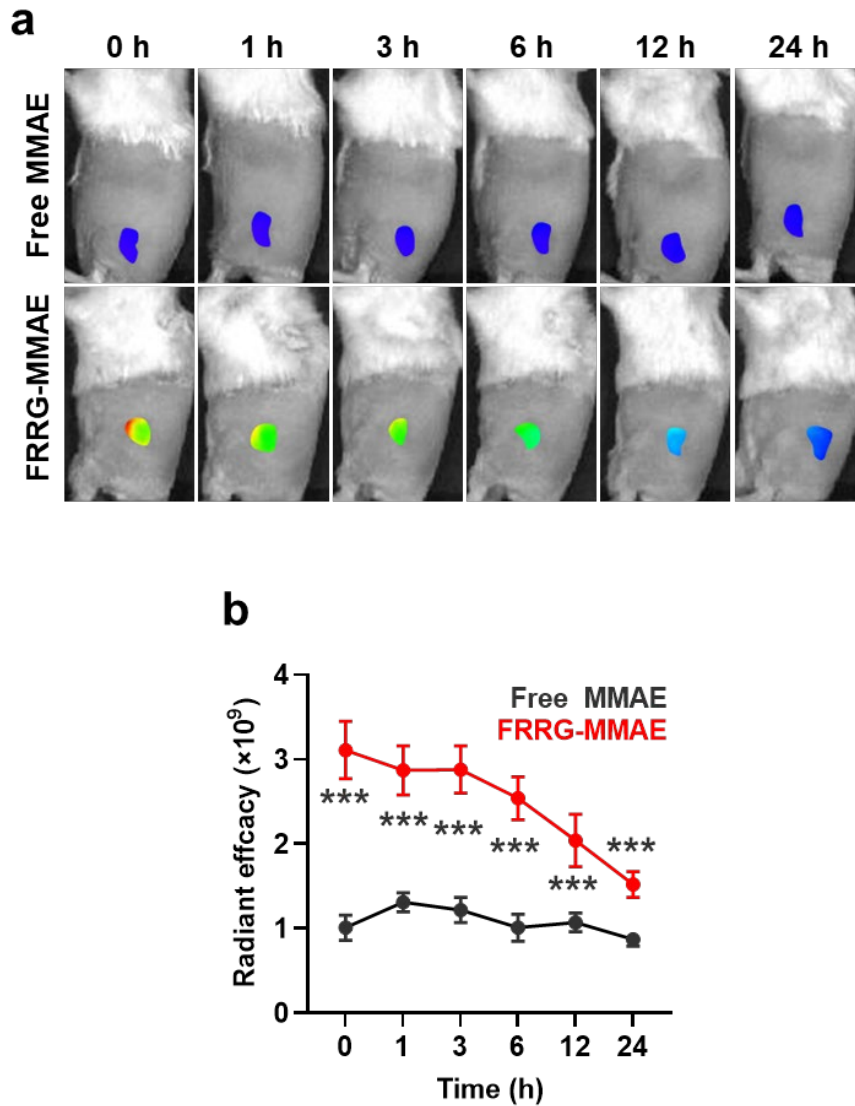


Figure 2.15. Tumor targeting of FRRG-MMAE nanoparticles. (a) NIRF images of 4T1 tumor-bearing mice treated with fluorescent dye Cy5.5-conjugated free MMAE or FRRG-MMAE. (b) Quantitative analysis for fluorescence intensities in the tumor regions of NIRF images. The statistical significance was indicated with asterisks *** $p < 0.001$ in the figures.

To evaluate the antitumor efficacy and safety of FRRG-MMAE nanoparticle treatment, 4T1 tumor-bearing mice were treated with free MMAE (1 mg/kg) or FRRG-MMAE nanoparticles (equivalent dose of 1 mg/kg based on MMAE contents) once every three days. As expected, FRRG-MMAE nanoparticles ($71.92 \pm 26.03 \text{ mm}^3$) significantly inhibited the tumor growth compared to saline ($261.81 \pm 37.33 \text{ mm}^3$; $p < 0.001$) and free MMAE ($154.73 \pm 31.63 \text{ mm}^3$; $p < 0.001$) groups on day 5 after treatment (Figure 2.16). In addition, tumor tissues stained with fluorescent dye Cy5-conjugated tubulin antibody showed a significantly inhibited tubulin formation compared to saline and free MMAE groups after five days of treatment (Figure 2.17). Tumor tissues stained with H&E also showed greatly elevated structural abnormalities from the extensive tumor areas in the FRRG-MMAE nanoparticle group than saline and free MMAE groups after five days of treatments (Figure 2.18a). Quantitatively, the ratio of the damaged areas in the tumor tissues from mice treated with FRRG-MMAE nanoparticles were 14.31 - 14.48-fold and 1.63 - 1.88-fold higher compared to those treated with saline and free MMAE, respectively (Figure 2.18b). This is attributable to the high tumor accumulation owing to the EPR effect by 200 nm-sized stable structure of FRRG-MMAE nanoparticles [30]. To directly compare the antitumor efficacy of free MMAE and FRRG-MMAE nanoparticles for 15 days, tumor growth of 4T1 tumor-bearing mice was additionally assessed during treatment with 0.5 mg/kg MMAE once every three days. This is because mice treated with 1 mg/kg MMAE once every three days were all dead within five days owing to their severe systemic toxicity. The results demonstrated that free MMAE-treated mice showed rapid tumor growth compared to FRRG-MMAE-treated mice during monitoring for 15 days (Figure 2.19). The safety of FRRG-MMAE nanoparticle treatment was evaluated via H&E staining of normal

organs (liver, lung, spleen, kidney and heart) after five days of treatment. As shown in Figure 2.18, mice treated with free MMAE showed severe systemic toxicity, wherein the structural abnormalities (black arrows) were clearly observed in all the organs. Moreover, free MMAE treated mice showed significant changes in the hematological parameters related with liver or kidney toxicities including albumin (ALB), aspartate aminotransferase (AST) and alanine transaminase (ALT), whereas those in the mice treated with FRRG-MMAE nanoparticles were in normal range and similar with saline group after five days of treatment (Figure 2.20). Finally, mice treated with free MMAE showed significant body weight loss owing to the severe toxicity; eventually, all the mice were dead within five days of treatment (Figure 2.21). In contrast, FRRG-MMAE nanoparticle-treated mice exhibited no significant changes in the body weight compared to saline group, wherein the no death cases occurred during 15 days of treatment. These results show the significantly reduced MMAE-related toxicity in the FRRG-MMAE nanoparticle group. Collectively, my findings demonstrate that FRRG-MMAE nanoparticles effectively inhibit the tumor growth, owing to the tumor-specific MMAE release and the high tumor accumulation due to the nanoparticle-derived EPR effect, as well as reduce MMAE-related toxicity by high cathepsin B-specificity, thereby allowing safe and effective chemotherapy.

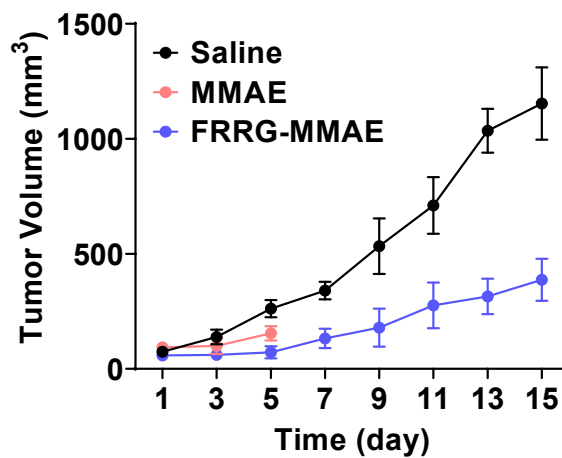


Figure 2.16. Antitumor efficacy of FRRG-MMAE nanoparticles. Tumor growth of 4T1 tumor-bearing mice during treatment with free MMAE or FRRG-MMAE nanoparticles once every three days.

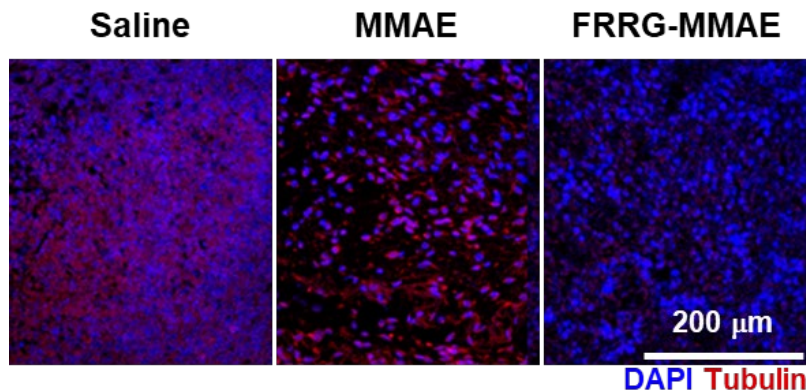


Figure 2.17. Tumor tissue stained with fluorescent dye Cy5-conjugated tubulin antibody after 5 days of treatment.

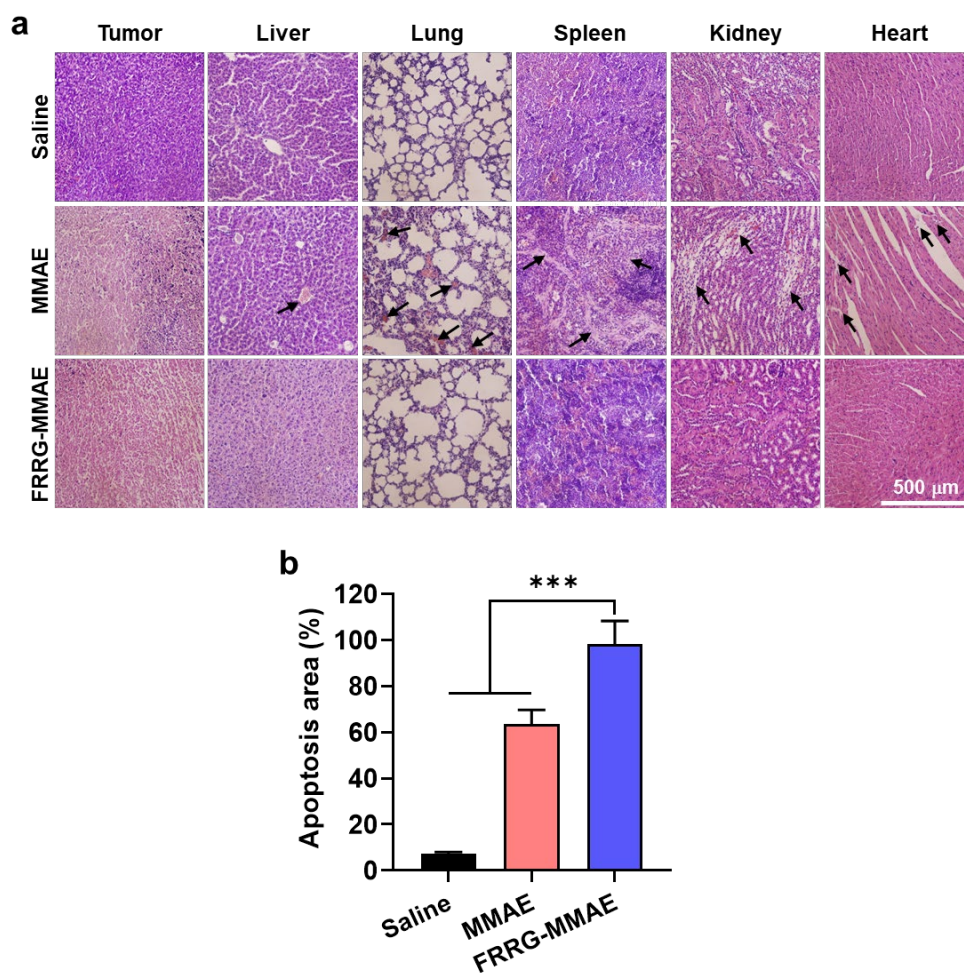


Figure 2.18. Antitumor efficacy and safety of FRRG-MMAE nanoparticles in breast tumor-bearing mice. (a) Tumor and organ tissues stained with H&E after 5 days of treatment with free MMAE or FRRG-MMAE nanoparticles. (b) The percentages of apoptosis area in tumor tissues after 5 days of treatment with free MMAE or FRRG-MMAE nanoparticles. (***) $p < 0.001$)

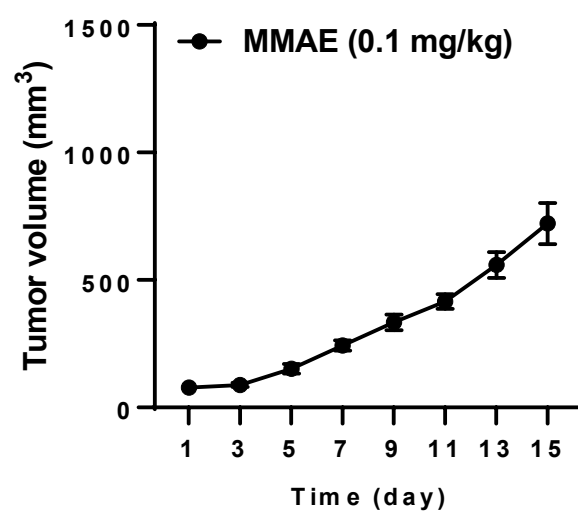


Figure 2.19. Tumor growth of 4T1 tumor-bearing mice during treatment with 0.5 mg/kg MMAE once every three days.

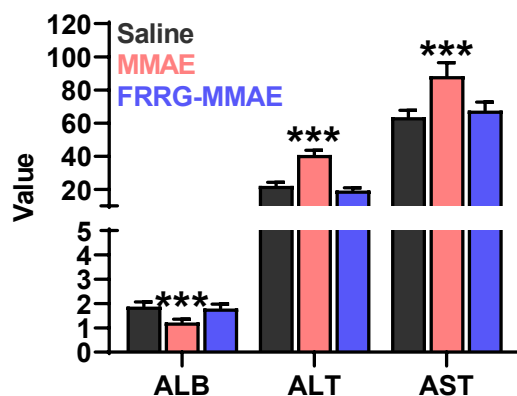


Figure 2.20. Hematological parameters of mice treated with saline, free MMAE or FRRG-MMAE for 5 days. The statistical significance was indicated with asterisks *** $p < 0.001$ in the figures.

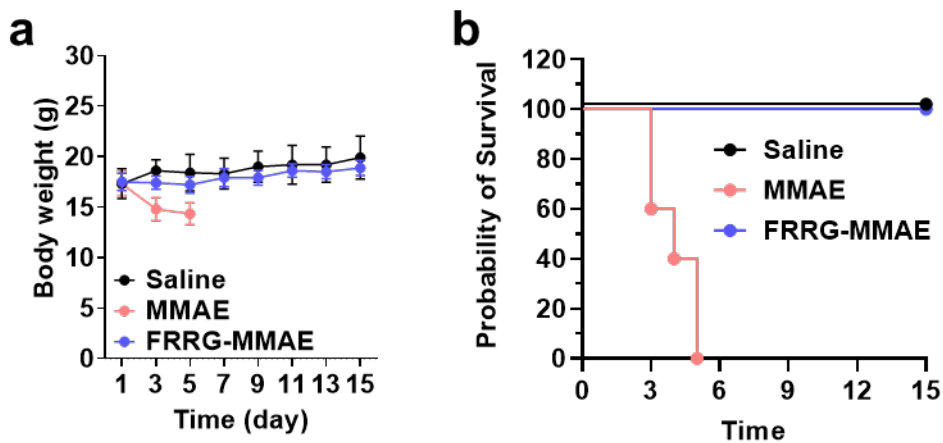


Figure 2.21. (a) The body weight of mice during treatment with free MMAE or FRRG-MMAE nanoparticles once every three days. (b) The mice survival.

2.4. Conclusion

In summary, I proposed tumor-specific MMAE prodrug nanoparticles for safe and effective chemotherapy. FRRG-MMAE, which consists of cathepsin B-specific cleavable FRRG peptide and MMAE, formed stable nanoparticles without any additional carrier materials by hydrophobic interaction-derived aggregations. Importantly, highly accumulated FRRG-MMAE nanoparticles in the tumor tissues via the EPR effect selectively released MMAE molecules in cathepsin B-overexpressed tumor cells, which induced a potent antitumor efficacy by inhibiting tubulin polymerization. Meanwhile, FRRG-MMAE nanoparticles significantly minimized the MMAE-related toxicity toward normal tissues owing to their innately low cathepsin B. As a result, efficient tumor delivery of MMAE by FRRG-MMAE nanoparticles greatly inhibited the breast tumor growth with minimal side effects. Compared with the conventional drug delivery system encapsulating anticancer drugs into the nanoparticles, this carrier-free prodrug nanoparticle system can mitigate the potential off-target toxicity by carrier materials. In addition, its precise and concise structures can achieve the simple one step synthetic protocol, thereby overcoming the formidable challenges of nanoparticles for clinical translation, such as difficulty in industrial-scale manufacturing and quality control (QC). Therefore, this study offers a promising approach for safe and effective chemotherapy via MMAE-based prodrug nanoparticles, which may open new avenues for advanced drug design for translational nanomedicine.

2.5. References

1. De Souza, R., et al., Polymeric drug delivery systems for localized cancer chemotherapy. *Drug Delivery*, 2010. 17(6): p. 365-375.
2. Shim, M.K., et al., Targeting of claudin-4 by *Clostridium perfringens* enterotoxin-conjugated polysialic acid nanoparticles for pancreatic cancer therapy. *Journal of Controlled Release*, 2021. 331: p. 434-442.
3. Shim, M.K., et al., Tumor-activated carrier-free prodrug nanoparticles for targeted cancer Immunotherapy: Preclinical evidence for safe and effective drug delivery. *Advanced Drug Delivery Reviews*, 2022. 183.
4. Jeon, S.I., et al., Cathepsin B-responsive prodrugs for cancer-targeted therapy: Recent advances and progress for clinical translation. *Nano Research*, 2022. 15(8): p. 7247-7266.
5. Xu, G. and H.L. McLeod, Strategies for enzyme/prodrug cancer therapy. *Clinical Cancer Research*, 2001. 7(11): p. 3314-3324.
6. Wu, T. and Y. Dai, Tumor microenvironment and therapeutic response. *Cancer Letters*, 2017. 387: p. 61-68.
7. Bejarano, L., M.J.C. Jordao, and J.A. Joyce, Therapeutic Targeting of the Tumor Microenvironment. *Cancer Discovery*, 2021. 11(4): p. 933-959.
8. Lee, S., et al., Nano-sized metabolic precursors for heterogeneous tumor-targeting strategy using bioorthogonal click chemistry in vivo. *Biomaterials*, 2017. 148: p. 1-15.
9. Shim, M.K., et al., Caspase-3/-7-Specific Metabolic Precursor for Bioorthogonal Tracking of Tumor Apoptosis. *Scientific Reports*, 2017. 7.

10. Shim, M.K., et al., Cathepsin B-Specific Metabolic Precursor for In Vivo Tumor-Specific Fluorescence Imaging. *Angewandte Chemie-International Edition*, 2016. 55(47): p. 14698-14703.
11. Kim, H.Y., et al., Epidermal growth factor (EGF)-based activatable probe for predicting therapeutic outcome of an EGF-based doxorubicin prodrug. *Journal of Controlled Release*, 2020. 328: p. 222-236.
12. Um, W., et al., Visible light-induced apoptosis activatable nanoparticles of photosensitizer-DEVD-anticancer drug conjugate for targeted cancer therapy. *Biomaterials*, 2019. 224.
13. Walther, R., J. Rautio, and A.N. Zelikin, Prodrugs in medicinal chemistry and enzyme prodrug therapies. *Advanced Drug Delivery Reviews*, 2017. 118: p. 65-77.
14. Yang, S., et al., Cancer-activated doxorubicin prodrug nanoparticles induce preferential immune response with minimal doxorubicin-related toxicity. *Biomaterials*, 2021. 272.
15. Buckell, L., et al., Tumor Radiosensitization by Monomethyl Auristatin E: Mechanism of Action and Targeted Delivery. *Cancer Research*, 2015. 75(7): p. 1376-1387.
16. Bryant, P., et al., In Vitro and In Vivo Evaluation of Cysteine Rebridged Trastuzumab-MMAE Antibody Drug Conjugates with Defined Drug-to-Antibody Ratios. *Molecular Pharmaceutics*, 2015. 12(6): p. 1872-1879.
17. Li, C.Z., et al., Clinical pharmacology of vc-MMAE antibody-drug conjugates in cancer patients: learning from eight first-in-human Phase 1 studies. *Mabs*, 2020. 12(1).

18. Francisco, J.A., et al., cAC10-vcMMAE, an anti-CD30-monomethyl auristatin E conjugate with potent and selective antitumor activity. *Blood*, 2003. 102(4): p. 1458-1465.
19. Bennett, G., et al., MMAE Delivery Using the Bicycle Toxin Conjugate BT5528. *Molecular Cancer Therapeutics*, 2020. 19(7): p. 1385-1394.
20. Karsten, L., et al., Bivalent EGFR-Targeting DARPIn-MMAE Conjugates. *International Journal of Molecular Sciences*, 2022. 23(5).
21. Serna, N., et al., Time-Prolonged Release of Tumor-Targeted Protein-MMAE Nanoconjugates from Implantable Hybrid Materials. *Pharmaceutics*, 2022. 14(1).
22. Cho, H., et al., Cathepsin B-Overexpressed Tumor Cell Activatable Albumin-Binding Doxorubicin Prodrug for Cancer-Targeted Therapy. *Pharmaceutics*, 2022. 14(1).
23. Choi, J., et al., Visible-Light-Triggered Prodrug Nanoparticles Combine Chemotherapy and Photodynamic Therapy to Potentiate Checkpoint Blockade Cancer Immunotherapy. *Acs Nano*, 2021. 15(7): p. 12086-12098.
24. Kim, J., et al., The safe and effective intraperitoneal chemotherapy with cathepsin B-specific doxorubicin prodrug nanoparticles in ovarian cancer with peritoneal carcinomatosis. *Biomaterials*, 2021. 279.
25. Kim, J., et al., Combination of cancer-specific prodrug nanoparticle with Bcl-2 inhibitor to overcome acquired drug resistance. *Journal of Controlled Release*, 2021. 330: p. 920-932.
26. Moon, Y., et al., Anti-PD-L1 peptide-conjugated prodrug nanoparticles for targeted cancer immunotherapy combining PD-L1 blockade with

- immunogenic cell death. *Theranostics*, 2022. 12(5): p. 1999-2014.
27. Shim, M.K., et al., Cancer-specific drug-drug nanoparticles of pro-apoptotic and cathepsin B-cleavable peptide-conjugated doxorubicin for drug-resistant cancer therapy. *Biomaterials*, 2020. 261.
 28. Shim, M.K., et al., Carrier-free nanoparticles of cathepsin B-cleavable peptide-conjugated doxorubicin prodrug for cancer targeting therapy. *Journal of Controlled Release*, 2019. 294: p. 376-389.
 29. Zhuang, W.R., et al., Applications of pi-pi stacking interactions in the design of drug-delivery systems. *Journal of Controlled Release*, 2019. 294: p. 311-326.
 30. Lim, S., et al., Recent advances and challenges of repurposing nanoparticle-based drug delivery systems to enhance cancer immunotherapy. *Theranostics*, 2019. 9(25): p. 7906-7923.

Chapter 3. Cancer-targeted therapy using cathepsin B activated albumin-binding doxorubicin prodrug

3.1 Introduction

Chemotherapy is still the first-line treatment option as its high sensitivity against wide range of cancers, but it is often accompanied by serious side effects attributed to a lack of cancer selectivity [1]. The risk of side effects by chemotherapy restricts drug dosage, which may limit the tumors from being exposed to sufficiently high drug concentrations, eventually leading to treatment failure [2]. Thus, many endeavors have been made to overcome these issues by improving the cancer selectivity of anticancer drugs to tumors. One of the promising approaches, prodrug, involves bioreversible medications that should undergo an enzymatic or chemical transformation in the tumor microenvironment to release active drugs, which greatly improve the cancer selectivity to reduce the off-target toxicity of anticancer drugs [3–5]. Selective activation of prodrugs can be achieved by intrinsic differences of enzyme expression between tumor and normal tissues [6]. Many designed prodrugs that selectively release active drugs by overexpressed enzymes in the tumor microenvironment, including caspases, cathepsins, and matrix metalloproteinases (MMPs), have greatly increased the safety of chemotherapy with minimal side effects [7–10]. However, such approaches have been challenged by unfavorable pharmacokinetics (PK), indicating a short in vivo half-life and poor tumor targeting owing to their small molecule structure, resulting in limited antitumor efficacy [11].

Albumin is the most abundant protein in the blood and has 17 disulphide bonds with one free thiol from unpaired cysteine (Cys34), which has emerged as a versatile protein carrier to improve the PK profile of anticancer drugs for tumor targeting [12]. The underlying mechanism of albumin-based drug delivery is that anticancer drugs containing thiol-reactive molecules selectively bind to accessible free thiol on Cys34 of endogenous albumins, and thus enhance the half-lives of drugs [13]. This long half-life is attributable mainly to its macromolecular size, being above the kidney filtration threshold, as well as receptor-mediated salvage mechanism, preventing degradation, facilitated by the neonatal Fc receptor (FcRn) [14]. Therefore, anticancer drugs bound to albumin accumulate within tumors via the enhanced permeability and retention (EPR) effect that is shown in the macromolecular complex by the increased vascular permeability and low lymphatic drainage [15,16]. In clinics, albumin-bound doxorubicin, aldoxorubicin, has shown potent antitumor efficacy with significantly prolonged patient survival [17]. However, the delivery efficiency to tumors of even the effective drug carriers was, unexpectedly, found to be less than 1~3% in many preclinical studies [18]. This means that a considerable amount of drugs inevitably localized in the off-target tissues and blood stream, which can increase the risk of systemic toxicity. Thus, albumin-based drug delivery of aldoxorubicin still indicated representative side effects of chemotherapy in patients at various stages [19].

3.2 Materials and Methods

3.2.1. Materials

Synthesized peptide *Phe-Arg-Arg-Gly* (NH₂-FRRG-COOH) was purchased

from Peptron (Daejeon, Republic of Korea). Cathepsin B-inhibitory siRNA, γ -maleimidobutyric acid, and monoclonal anti-mouse cathepsin B antibody were purchased from Santa Cruz Biotechnology (Dallas, TX, USA). Cell counting kit-8 (CCK-8) was purchased from Vitascientific (Beltsville, MD, USA). TUNEL assays kit, recombinant cathepsin B, cathepsin E, cathepsin D, caspase-9, and caspase-3 were purchased from R&D systems (Minneapolis, MN, USA). BCA protein quantification kit was purchased from Thermo Fisher scientific (Oakville, ON, USA). Maleimide-PEG₂-NHS, human serum albumin (HSA), mouse serum albumin (MSA), bovine serum albumin (BSA), hematoxylin and eosin (H&E) staining kit, and doxorubicin hydrochloride were purchased from Sigma Aldrich (Oakville, ON, USA). Fetal bovine serum (FBS), RPMI 1640 medium, Dulbecco's modified Eagle medium (DMEM) high glucose medium, streptomycin, and penicillin were purchased from WELGENE Inc. (Daegu, Korea). Anti-b-actin antibody was purchased from Abcam (Hanam, Republic of Korea). MDA-MB-231 (human breast cancer cells) and H9C2 (rat BDIX heart myoblasts) cell lines were purchased from American Type Culture Collection (ATCC; Manassas, VA, USA). Six-week-old female Balb/c nude mice were purchased from NaraBio, Inc. (Seoul, Korea).

3.2.2. Synthesis of cathepsin B-overexpressed tumor cell activatable albumin-binding doxorubicin prodrug (Al-ProD)

Al-ProD was synthesized via a three-step reaction. At first, Fmoc protected FRRG (200 mg, 1 eq.) was reacted with doxorubicin hydrochloride (229.9 mg, 1.5 eq.) in 10 ml anhydrous DMF under 37 °C for 12 h. EDC (76 mg, 1.5 eq.), HOBt (60.9 mg, 1.5 eq.) and DIPEA (76.8 mg, 1.5 eq.) were additionally dissolved in the reaction

mixture. At the end of reaction, the reaction mixture was precipitated in diethylether and further purified via HPLC Preparation. Second, N-term protection group Fmoc was removed from synthesized Fmoc-FRRG-Dox by 20 % piperidine in anhydrous DMF for 15 min. After that, the reaction mixture was precipitated in diethylether. Finally, subsequent synthesis of maleimide-PEG₂-FRRG-Dox (Al-ProD) was performed by dissolving maleimide-PEG₂-NHS (120.4 mg, 3 eq.) and previously synthesized FRRG-Dox (100 mg, 1 eq.) in 10 mL anhydrous DMF with DIPEA (18.3 mg, 1.5 eq.) while stirring at 37 °C for 24 h. Then, Al-ProD was further purified via HPLC, and lyophilized at -90 °C to obtain a red powder (Freeze Dryer, ilShinBioBase, Republic of Korea). After preparation, successful synthesis of Al-ProD was confirmed by measuring purity and molecular weight via HPLC and MALDI-TOF mass spectrometer, respectively.

3.2.3. Characterization of Al-ProD

The albumin-binding property of Al-ProD was firstly evaluated. Briefly, to a human serum albumin (HSA), mouse serum albumin (MSA), or bovine serum albumin (BSA; 700 µM in PBS; pH 7.4), Al-ProD (100 µM) was added and incubated for 0, 5, and 60 min at room temperature. As a control, the HSA solution was pre-incubated with γ -maleimidobutyric acid for 1 h before adding Al-ProD. After incubation, samples were analyzed via native 12% SDS-PAGE gel. The gels were observed by trans-UV using the iBrightTM Imaging System (Invitrogen by Thermo Fisher Scientific), and then stained with coomassie blue for visualizing proteins. The albumin-binding property of Al-ProD was further analyzed using reverse-phased high performance liquid chromatography (RP-HPLC; Agilent cary 300; Agilent Technologies) with ACN/H₂O gradient from 80:20 to 20:80 for 30 min under a fluorescence detector (Ex/Em: 530/590

nm). In addition, mass shift after incubation of HSA with Al-ProD for 5 min was confirmed by a matrix-assisted laser desorption/ionization time of flight (MALDI-TOF, AB Sciex TOF/TOF 5800 System, Annapolis, MD, USA) mass spectrometer with a cyano-4-hydroycinnamic acid (CHCA) matrix. Next, cathepsin B-specific cleavage of Al-ProD that was pre-incubated with HAS for 5 min (HSA-bound Al-ProD; 10 μ M) was assessed by incubating with cathepsin B, cathepsin E, cathepsin D, cathepsin L, caspase-9, or caspase-3 (50 μ g) at 37 °C for 24 h, followed by an analysis using HPLC with ACN/H₂O gradient from 20:80 to 80:20 for 30 min.

3.2.4. Cellular uptake

To assess intracellular behavior of Al-ProD via fluorescence imaging, 3×10^5 MDA-MB-231 and H9C2 cells were seeded in confocal dishes. After 24 h stabilization, each cell was incubated with free DOX or HSA-bound Al-ProD (2 μ M) for 48 h at 37 °C. As a control, MDA-MB-231 cells were pre-incubated for 2 h with cathepsin B-inhibitory siRNA that was pre-incubated with Lipofectamine 2000 for 40 min at room temperature. Then, cells were washed twice with DPBS, fixed with 5% paraformaldehyde for 15 min, and stained with 4',6-diamidino-2-phenylindole (DAPI) for 10 min. Fluorescence imaging was performed using a Leica TCS SP8 confocal laser-scanning microscope (Leica Microsystems GmbH; Wetzlar, Germany). The DOX fluorescence in images was quantitatively analyzed using an Image Pro software (Media Cybernetic, Rockville, MD, USA).

3.2.5. Cytotoxicity assay

The cytotoxicity of Al-ProD was assessed via cell counting kit-8 (CCK-8)

assays. First, 5×10^3 MDA-MB-231 or H9C2 cells were seeded in 96-well cell culture plates. After 24 h stabilization, the free DOX or HSA-bound Al-ProD were added to each well and incubated for 48 h. Then, the cells were additionally incubated with culture medium containing 10% CCK-8 solution for 30 min. The cell viability was measured using a microplate reader (VERSAmaxTM; Molecular Devices Corp., San Jose, CA, USA) with 450 nm of wavelength.

3.2.6. Western blot

Cathepsin B expression in MDA-MB-231 and H9C2 cells was analyzed via Western blot [20]. Briefly, 2×10^5 MDA-MB-231 or H9C2 cells were seeded in six-well cell culture plates. After 24 h incubation, MDA-MB-231 and H9C2 cells were solubilized using lysis buffer including 1% protease inhibitors, and the resulting lysates were centrifuged at 3000 rpm for 40 min to remove debris. The proteins in lysates were quantified by BCA protein quantification kit, and then separated using sodium dodecyl sulfate-polyacrylamide gel electrophoresis (SDS-PAGE) and transferred onto PVDF membranes. Then, membranes were incubated with TBS-T containing 5% bovine serum albumin (BSA) for 1 h to block non-specific IgG binding and incubated with anti-cathepsin B primary antibody for 12 h at 4 °C. Finally, membranes were incubated with HRP-conjugated anti-mouse IgG antibody for 2 h at room temperature and immunoreactive bands were observed via an enhanced chemiluminescence (ECL) system.

3.2.7. Pharmacokinetics (PK)

Mice were bred under pathogen-free conditions at the Korea Institute of

Science and Technology (KIST). All experiments with live animals were performed in compliance with the relevant laws and institutional guidelines of Institutional Animal Care and Use Committee (IACUC) in KIST, and IACUC approved the experiment (approved number of 2020-123). To assess pharmacokinetic (PK) profiles *in vivo*, BALB/c nude mice were intravenously injected with free DOX (5 mg/kg) or Al-ProD (5 mg/kg based on DOX contents), and blood samples were collected from mice at pre-determined times (0, 3 h, 6 h, 9 h, 12 h, 24 h, 48 h, 72 h, 96 h, 120 h, and 144 h). Then, each drug in the blood samples was extracted with DMSO by intense vortex and the samples were centrifuged at 2000 rpm for 40 min to obtain as a blood plasma. Finally, amount of free DOX and Al-ProD in samples was analyzed by IVIS Lumina Series III system (PerkinElmer; Waltham, MA, USA).

3.2.8. Biodistribution in breast tumor models

The biodistribution of Al-ProD was assessed in breast tumor models, which were prepared by subcutaneous inoculation of 1×10^7 MBA-MB-231 cells into the left flank of BALB/c nude mice. When the tumor volumes were approximately 200–250 mm³, the mice were intravenously injected with free DOX (5 mg/kg) or Al-ProD (5 mg/kg based on DOX contents). Then, noninvasive near-infrared fluorescence (NIRF) imaging was performed using an IVIS Lumina Series III system after 0 h, 3 h, 6 h, 12 h, 24 h, 48 h, and 72 h of injection. Fluorescence intensities in tumor regions were quantified via Living Image software. Mice were sacrificed after 12 h of injection for *ex vivo* imaging, followed by the collection of lung, liver, kidney, spleen, heart, and tumor tissues. Tumor tissues were also cut into 10 µm thick sections for histological assays. Slide-mounted tumor sections were analyzed by Leica TCS SP8 confocal laser-

scanning microscope.

3.2.9. Antitumor efficacy and toxicity evaluation

To evaluate the antitumor efficacy, MDA-MB-231 tumor-bearing mice were randomly divided into three groups: (i) saline; (ii) free DOX; and (iii) Al-ProD. Then, mice were treated once every three days with free DOX (5 mg/kg) or Al-ProD (5 mg/kg based on DOX contents), at which time tumor volumes were approximately 60–80 mm³. Antitumor efficacy was assessed by measuring tumor volumes once every two days, calculated as largest diameter \times smallest diameter² \times 0.53, once every 2 days. The body weights of mice were also measured once every two days to assess in vivo toxicity. The in vivo toxicity of Al-ProD was further assessed by histological analyses. At 20 days after treatment, major organs were collected from mice and samples were stained with H&E following the manufacturer's protocol. Then, organ sections were observed using an optical microscope.

3.2.10. Statistics

The statistical significance between two groups was analyzed using Student's t-test. One-way analysis of variance (ANOVA) was performed for comparisons of more than two groups, and multiple comparisons were analyzed using Tukey–Kramer post-hoc test. Survival data were plotted as Kaplan–Meier curves and analyzed using log-rank test. Statistical significance was indicated with an asterisk (* $p < 0.05$, ** $p < 0.01$, and *** $p < 0.001$) in the figures.

3.3 Results

3.3.1 Albumin-binding and selective activation of Al-ProD

Herein, I propose cathepsin B-overexpressed tumor cell activatable albumin-binding doxorubicin prodrug, Al-ProD, which can effectively deliver anticancer drugs by in situ albumin-mediated passive targeting with minimal side effects. The Al-ProD was prepared by conjugating doxorubicin (DOX) to C-terminus of cathepsin B-cleavable peptide ($\text{NH}_2\text{-FRRG-COOH}$; $\text{NH}_2\text{-Phe-Arg-Arg-Gly-COOH}$) and introducing a maleimide group to the N-terminus of peptide (Figure 3.1a). The maleimide group in the Al-ProD selectively bound to the thiol in physiological pH, thereby allowing the covalent binding with in situ circulating albumin (Figure 3.1b). Moreover, FRRG peptide is a well-known substrate of cathepsin B, which is associated with tumor invasion and metastasis as a promising cancer biomarker overexpressed in malignant tumors compared with normal tissues in clinical studies [21,22]. Compared with other substrate peptide of cathepsin B, FRRG peptide exhibited high specificity against the target enzyme without non-specific cleavage and, especially, it was reported that G-DOX cleaved from FRRG-DOX by enzymatic cleavage was additionally metabolized into free DOX by intracellular proteases [23,24]. Therefore, the in situ albumin-bound Al-ProD greatly enhances tumor accumulation with prolonged in vivo half-life and induces a potent antitumor efficacy by selectively releasing free DOX in cathepsin B-overexpressed tumor cells (Figure 3.1c). Concurrently, toxicity toward normal tissues with innately low cathepsin B expression is significantly reduced by maintaining a non-toxic inactive state, thereby increasing the safety of chemotherapy (Figure 3.1d). In the present study, albumin-binding of Al-ProD was confirmed on

human serum albumin (HSA), mouse serum albumin (MSA), and bovine serum albumin (BSA). Selective action of Al-ProD was studied in breast cancer cells and cardiomyocytes, indicating differential levels of cathepsin B. The *in vivo* pharmacokinetics and tumor regression effect with minimal toxicity were also carried out in breast cancer models.

The cathepsin B-overexpressed tumor cell activatable albumin-binding doxorubicin prodrug, Al-ProD, which consists of albumin-binding maleimide group, cathepsin B-cleavable peptide (NH₂-FRRG-COOH; NH₂-Phe-Arg-Arg-Gly-COOH), and doxorubicin (DOX), was designed for cancer-targeted therapy with minimal side effects. The Al-ProD was synthesized by introducing a maleimide group to the N-terminus of FRRG peptide and conjugating DOX to the C-terminus of peptide (Figure 3.2). After the reaction, 99% of Al-ProD was purified with HPLC (Figure 3.3). The successful synthesis was also confirmed via matrix-assisted laser desorption ionization time-of-flight (MALDI-TOF) mass spectrometer, wherein the exact molecular weight of Al-ProD was calculated to be 1370.44 Da for C₆₄H₈₃N₁₃O₂₁ and measured to be 1370.616 *m/z* [M] (Figure 3.4).

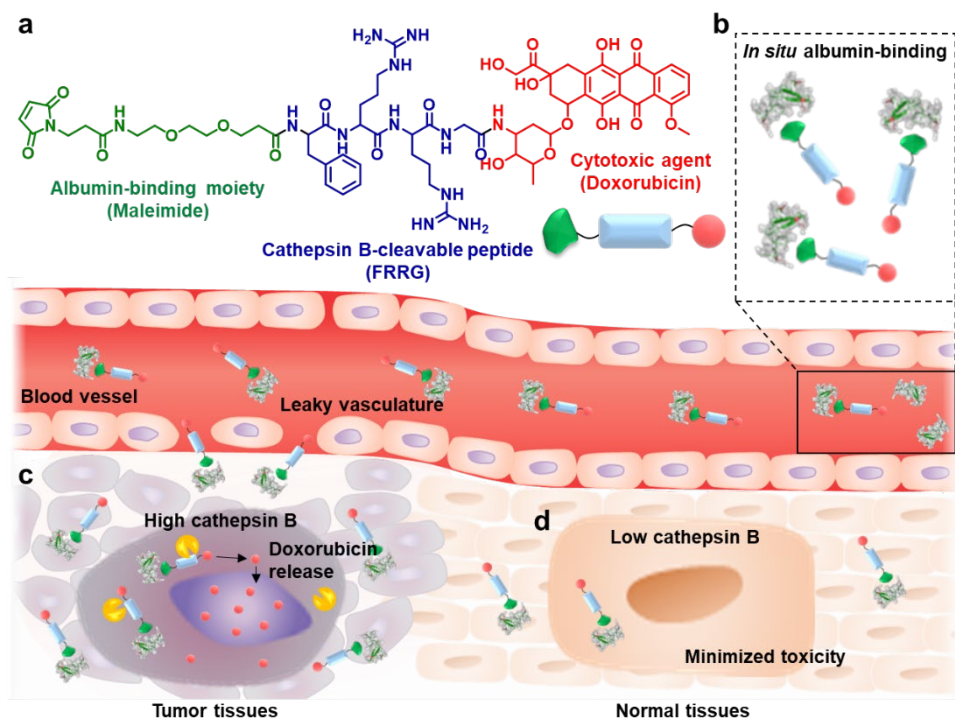


Figure 3.1. In situ albumin-mediated cancer-targeted therapy by AI-ProD. (a) The AI-ProD is prepared by conjugating doxorubicin (DOX) to the C-terminus of cathepsin B-cleavable peptide (FRRG) and introducing a maleimide group to the N-terminus of peptide. (b) Intravenously injected AI-ProD efficiently binds to in situ circulating albumin in blood vessels. (c) Albumin-bound AI-ProD greatly enhances tumor accumulation via albumin-mediated passive tumor targeting and induces a potent antitumor efficacy by selectively releasing free DOX in cathepsin B-overexpressed tumor cells. (d) Concurrently, AI-ProD significantly reduced toxicity toward normal tissues with innately low cathepsin B expression by maintaining a non-toxic inactive state, thereby increasing the safety of chemotherapy.

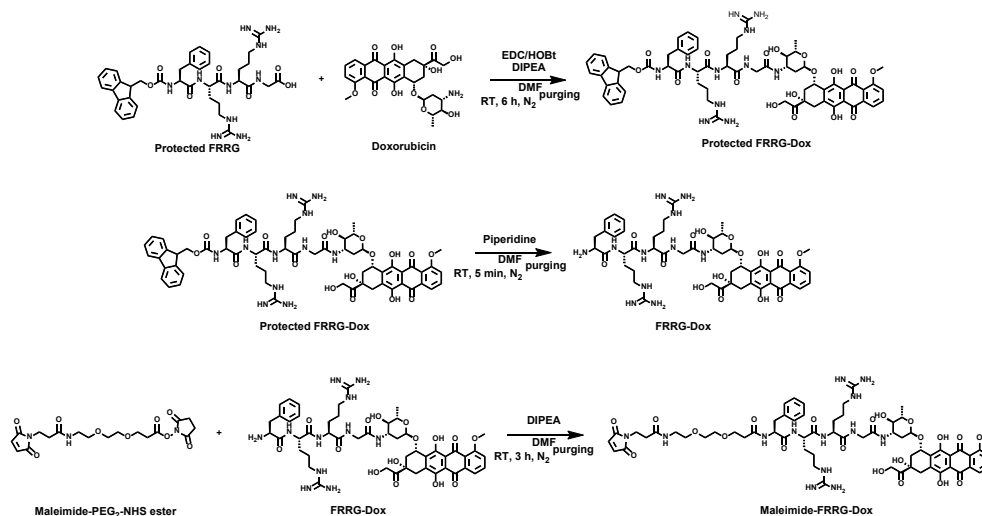


Figure 3.2. Al-ProD was synthesized via a three-step reaction. At first, Fmoc protected FRRG (200 mg, 1 eq.) was reacted with doxorubicin hydrochloride (229.9 mg, 1.5 eq.) in 10 ml anhydrous DMF under 37 °C for 12 h. EDC (76 mg, 1.5 eq.), HOBt (60.9 mg, 1.5 eq.) and DIPEA (76.8 mg, 1.5 eq.) were additionally dissolved in the reaction mixture. Second, N-term protection group Fmoc was removed from synthesized Fmoc-FRRG-Dox by 20 % piperidine in anhydrous DMF for 15 min. Finally, subsequent synthesis of maleimide-PEG₂-FRRG-Dox (Al-ProD) was performed by dissolving maleimide-PEG₂-NHS (120.4 mg, 3 eq.) and previously synthesized FRRG-Dox (100 mg, 1 eq.) in 10 mL anhydrous DMF with DIPEA (18.3 mg, 1.5 eq.) while stirring at 37 °C for 24 h.

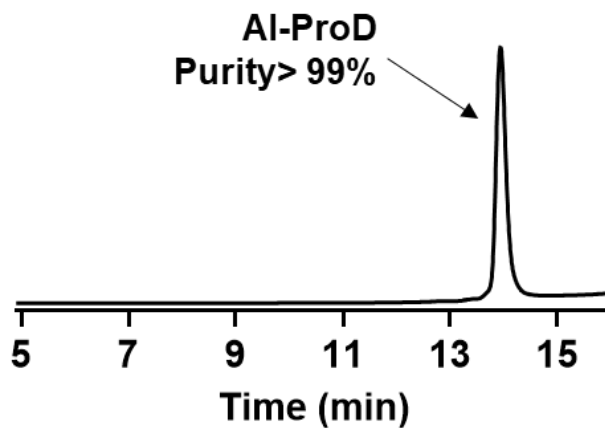


Figure 3.3. The purity (> 99%) of Al-ProD was confirmed by high performance liquid chromatography (HPLC).

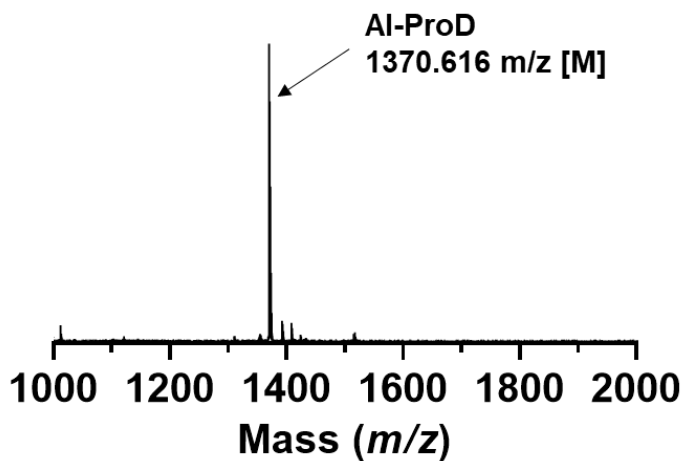


Figure 3.4. The molecular weight of Al-ProD was confirmed via MALDI-TOF mass spectrometer. The molecular weight of Al-ProD was calculated to be 1370.44 Da for $C_{64}H_{83}N_{13}O_{21}$ and measured to be 1370.616 m/z .

First, the plasma albumin-binding ability of Al-ProD was assessed by various *in vitro* studies. The Al-ProD and albumin from different species of human (human serum albumin; HSA), mouse (mouse serum albumin; MSA), and bovine (bovine serum albumin; BSA) were clearly observed via the doxorubicin absorbance and coomassie blue staining in SDS-PAGE gel, respectively (Figure 3.5). Importantly, the band of Al-ProD was detected below 7 kDa, but the band shifted to 50–75 kDa after incubation with HSA, BSA, or MSA for 1 h. In contrast, the Al-ProD band was not shifted when each albumin (HSA, MSA, and BSA) was preincubated with γ -maleimidobutyric acid to block the thiol group. As a control, FRRG-DOX with the absence of a maleimide group and free DOX were also not bound to all types of albumin, only showing the band below 7 kDa. The HSA-binding of Al-ProD was further analyzed by HPLC (Figure 3.6). Binding of Al-ProD with HSA in HPLC spectrum was confirmed by a shift of the Al-ProD peak (14 min) to a broad peak at 16 min that appeared to be a free HSA peak, wherein the binding was accomplished within 5 min. However, Al-ProD did not bound to HSA for 60 min when the thiol group of HSA was blocked. MALDI-TOF mass spectrometer further confirmed the molecular weight shift of the HSA from 66,409 to 67,780 m/z when incubated with Al-ProD, showing a mass difference comparable to that of Al-ProD (1370.616 m/z), indicating the successful albumin-binding (Figure 3.7).

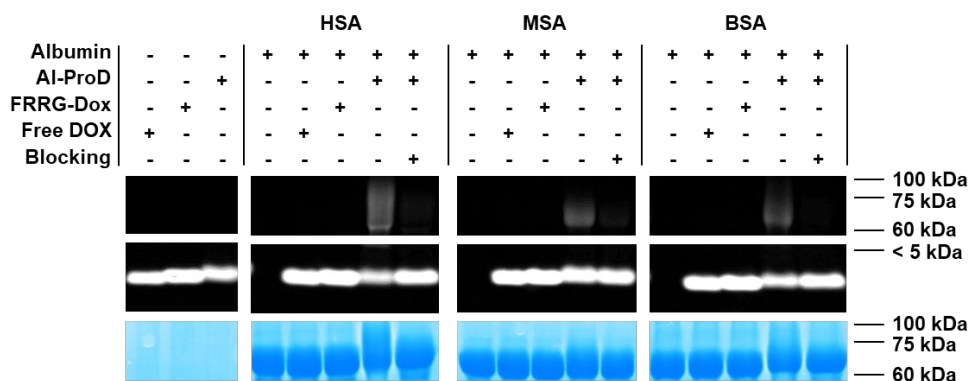


Figure 3.5. Albumin-binding of AI-ProD. AI-ProD was incubated with human serum albumin (HSA), mouse serum albumin (MSA), or bovine serum albumin (BSA) at room temperature. As a control, the HSA solution was pre-incubated with γ -maleimidobutyric acid to block thiol in HSA. In addition, free DOX or FRRG-DOX with the absence of a maleimide group were also incubated with three types of serum albumin. After incubation, samples were analyzed via SDS-PAGE gel.

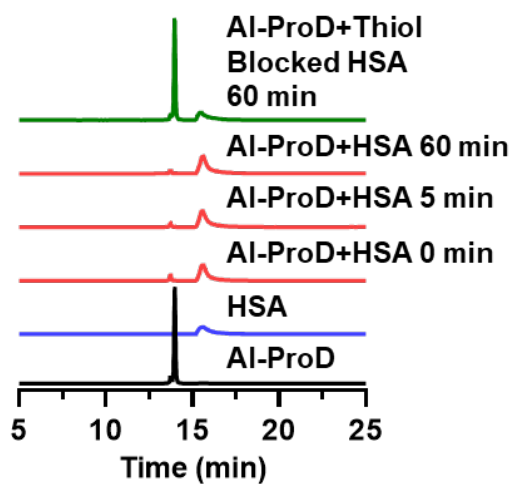


Figure 3.6. Albumin binding affinity of HSA analyzed via RP-HPLC. As a control, thiol group of HSA was blocked by γ -maleimidobutyric acid through 1 h pre-incubation.

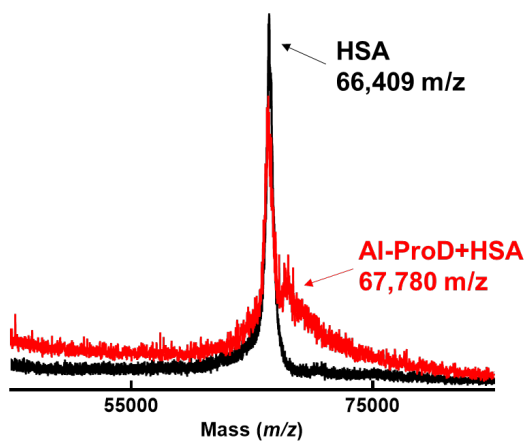


Figure 3.7. MALDI-TOF analysis results of human serum albumin and human serum albumin-bound Al-ProD.

Next, I assessed the cathepsin B-specific cleavage of Al-ProD by incubation with various enzymes. As the Al-ProD releases the DOX molecules via enzymatic degradation in the presence of cathepsin B, it is major of concern whether the cathepsin B can recognize and cleave FRRG peptide without interference by albumin adjacent when Al-ProD was bound to albumin. To address this concern, HSA-bound Al-ProD was incubated with enzyme reaction buffer containing cathepsin B (MES buffer; 50 $\mu\text{g/mL}$). The result showed that HSA-bound Al-ProD began to be cleaved to glycine-conjugated doxorubicin (G-DOX) after 3 h incubation and G-DOX release was gradually increased for 9 h incubation (Figure 3.8). These results were clearly supported by MALDI-TOF analysis, which confirm the molecular weight of G-DOX (calculated mass: 600.58 Da, measured mass: 601.2019 m/z [M+H], 623.184 [M+Na], and 639.1573 [M+K]) at a newly appeared peak (14 min) after incubation with cathepsin B in the HPLC spectrum (Figure 3.9). It was already reported that G-DOX cleaved from FRRG-DOX by cathepsin B enzymatic cleavage are efficiently metabolized into free DOX by intracellular proteases [23,24]. In contrast, HSA-bound Al-ProD was not cleaved by other enzymes, such as caspase-3, caspase-9, cathepsin D, cathepsin E, and cathepsin L, or saline (hydrolysis; Figure 3.10). These results clearly demonstrate that Al-ProD successfully binds to albumin via a maleimide group and selectively releases DOX molecules in the presence of cathepsin B enzyme.

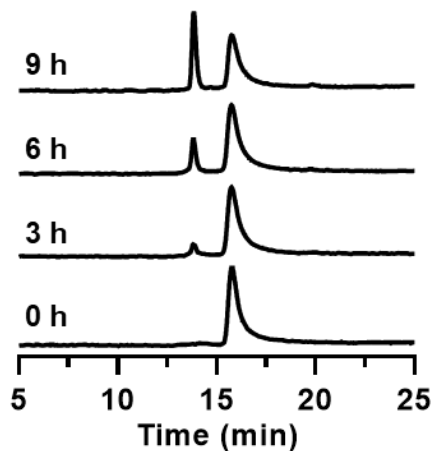


Figure 3.8. HPLC chromatograms when Al-ProD was incubated with cathepsin B. For the analysis, HSA-bound Al-ProD was incubated with MES buffer containing cathepsin B (50 $\mu\text{g/ml}$).

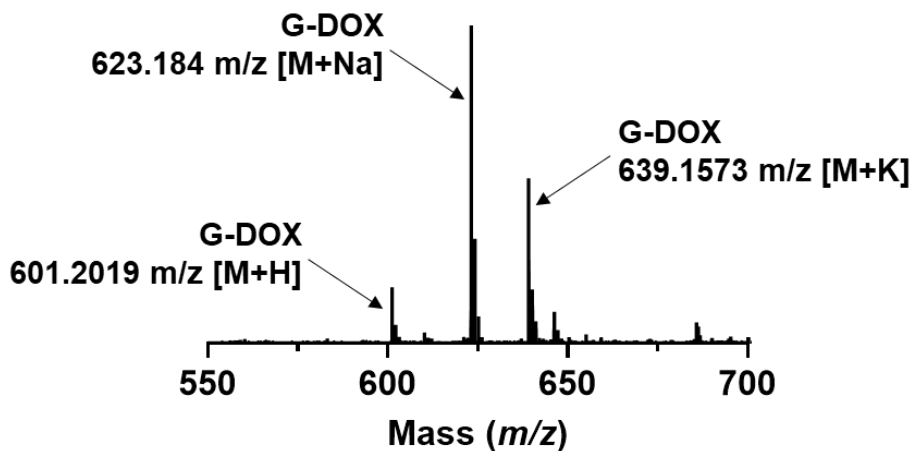


Figure 3.9. Metabolite assay of Al-ProD. Glycine-conjugated doxorubicin (G-DOX) released from Al-ProD was confirmed via MALDI-TOF mass spectrometer. For this analysis, Al-ProD was incubated with MES buffer containing cathepsin B (50 μg), and enzyme reaction buffer was analyzed. As a result, the molecular weights of G-DOX were measured to be 601.2019 m/z [M+H], 623.184 [M+Na] and 639.1573 [M+K].

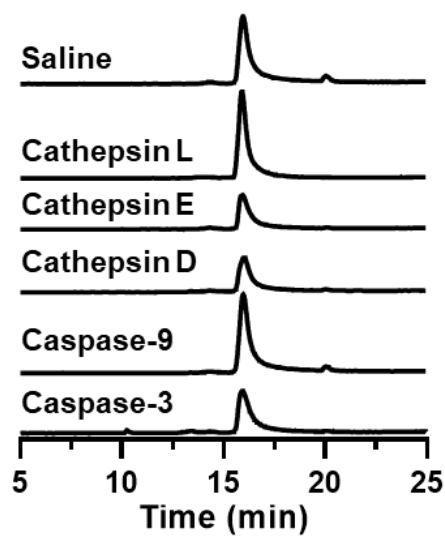


Figure 3.10. HPLC chromatograms when Al-ProD was incubated with saline (hydrolysis), cathepsin L, cathepsin E, cathepsin D, caspase-9 and caspase-3.

3.3.2. Cancer cell-selective cytotoxicity of Al-ProD

The in vitro selective activation of Al-ProD premised on differential expression levels of cathepsin B was assessed in breast cancer cells (MDA-MB-231) and rat BDIX cardiomyocytes (H9C2). As expected, MDA-MB-231 cells expressed a 24.26 ± 3.08 -fold high amount of cathepsin B compared with H9C2 cells (Figure 3.11). Each cell showed a robust uptake of HSA-bound Al-ProD (red color) after 48 h of incubation, as confirmed by confocal laser scanning microscope (CLSM; Figure 3.12). However, DOX fluorescence was limited to the cytoplasm of H9C2 cells, whereas that in MDA-MB-231 cells was observed in nuclei. The HSA-bound Al-ProD also remained in the cytoplasm of cathepsin B-suppressed MDA-MB-231 cells, which are pre-treated with cathepsin B-inhibitory siRNA for 24 h. Quantitatively, DOX fluorescence in nuclei was 2.48–2.89-fold stronger in HSA-bound Al-ProD-treated MDA-MB-231 cells than H9C2 and cathepsin B-suppressed MDA-MB-231 cells (Figure 3.13). In contrast, intracellular free DOX was clearly observed at the nuclei in both MDA-MB-231 and H9C2 cells, regardless of cathepsin B expression (Figure 3.14). As the mode of action of DOX is intercalation into DNA base pairs, inducing breakage of DNA strand and inhibition of DNA and RNA replication, the DOX molecule inside the nuclei of cells is an important indicator of its cytotoxicity. As a result, this differential cellular uptake of Al-ProD resulted in cancer cell-selective cytotoxicity [25]. The IC₅₀ value of HSA-bound Al-ProD in MDA-MB-231 was measured to be 7.33 mM, while it was >200 mM in H9C2 cells after 48 h incubation, which showed about a 30-fold difference that indicates cancer cell-selective cytotoxicity (Figure 3.15a). In contrast, free DOX exhibited indiscriminate cytotoxicity in both MDA-MB-231 and H9C2 cells with nearly similar IC₅₀ values (Figure 3.15b). These results suggest that

Al-ProD can efficiently eradicate cancers with minimal off-target toxicities toward normal tissues by selective activation in cancer cells.

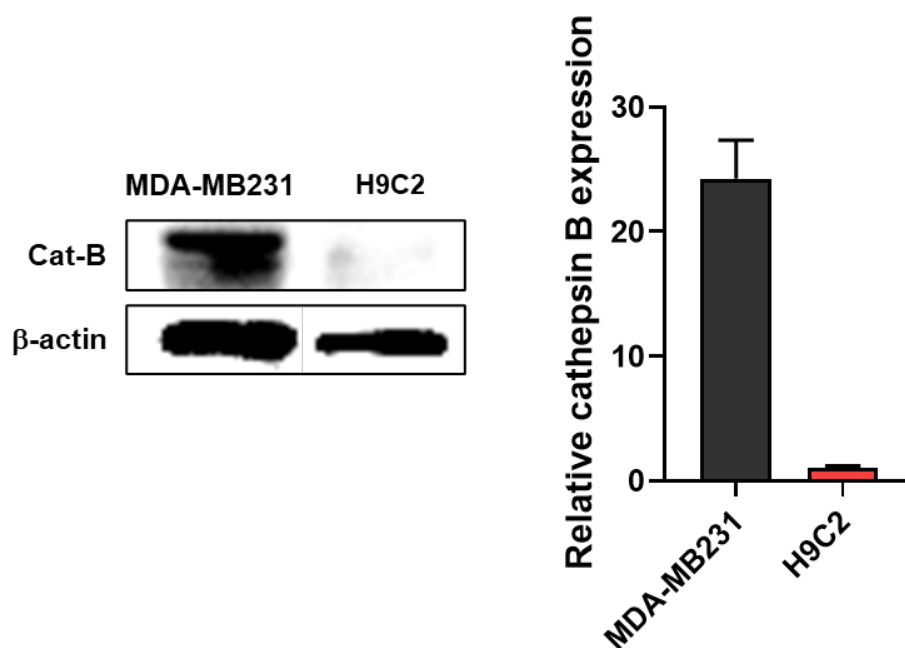


Figure 3.11. Cathepsin B expression levels of MDA-MB-231 and H9C2 cells. (left) Western blot analysis of cathepsin B of MDA-MB-231 cancer cells and H9C2 normal cells. (right) Relative expression levels of cathepsin B in each cell; MDA-MB-231 cells expressed 24.26 ± 3.08 -fold higher amount of cathepsin B than H9C2 cells.

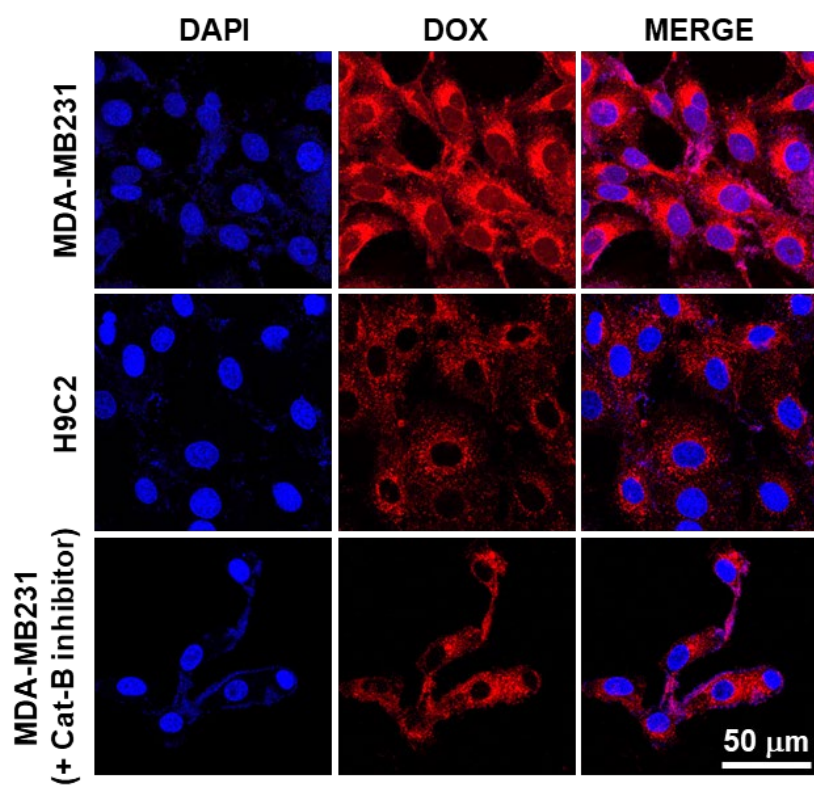


Figure 3.12. Confocal laser scanning microscope images of MDA-MB-231 and H9C2 cells treated with Al-ProD. As as control, MDA-MB-231 cells were pre-incubated with cathepsin B-inhibitory siRNA.

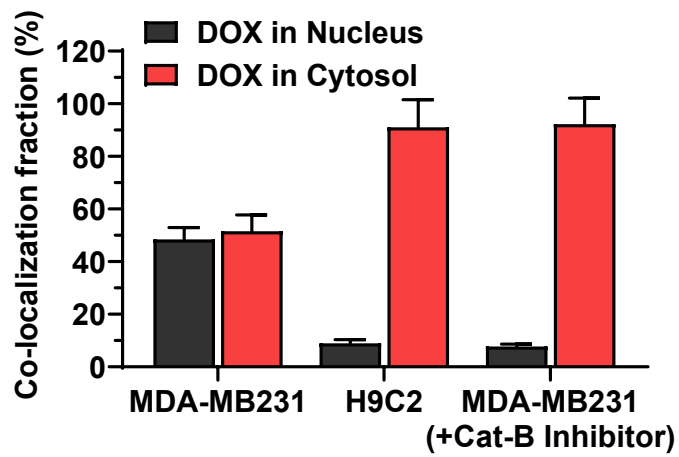


Figure 3.13. Quantification analysis of DOX fluorescence in nuclei or cytosol of Al-ProD-treated MDA-MB-231, H9C2 and cathepsin B-inhibitory siRNA-treated MDA-MB-231 cells.

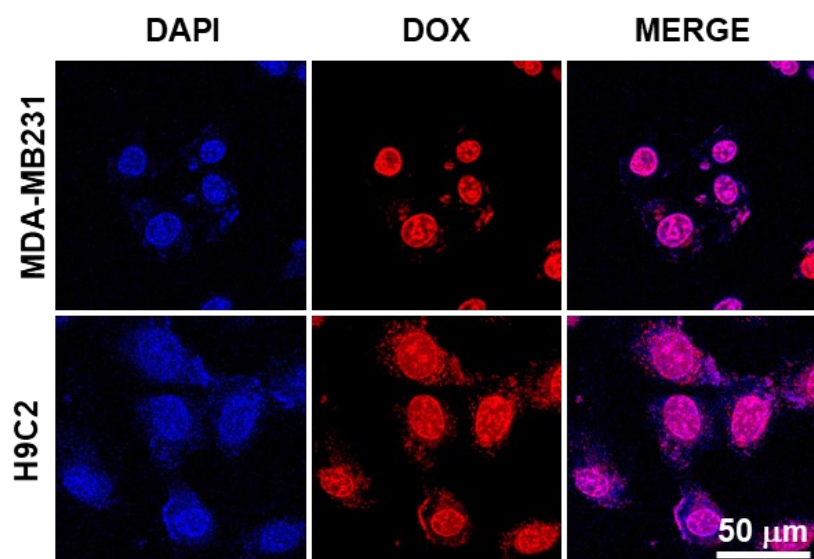


Figure 3.14. Fluorescence images of MDA-MB-231 and H9C2 cells treated with free Dox.

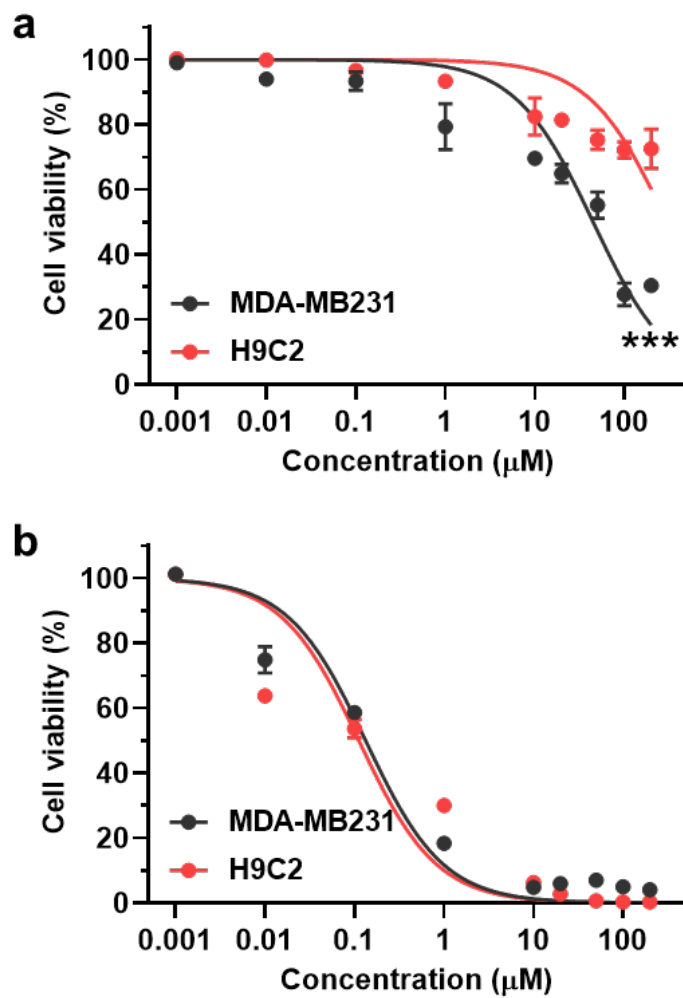
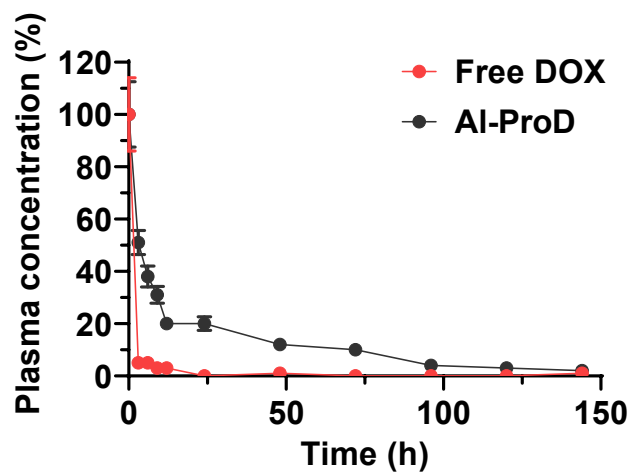


Figure 3.15. Cell cytotoxicity of (a) Al-ProD or (b) free Dox in MDA-MB-231 and H9C2 cells. Significance (***) $p < 0.001$ was determined by Student's t -test (a).

3.3.3. Pharmacokinetics and tumor targeting of Al-ProD

To evaluate the high tumor accumulation of albumin-binding Al-ProD by extended in vivo half-life, the pharmacokinetics (PK) of Al-ProD and free DOX was firstly compared in BALB/c nude mice after intravenous injection at a dose of molar equivalent to 5 mg/kg of doxorubicin. In contrast to free DOX, showing fast in vivo clearance with a half-life of 15 min, Al-ProD showed a significantly extended half-life of more than 3 h (Figure 3.16). In addition, a detectable amount of the Al-ProD remained for 144 h in the body, indicating the dramatically extended residence time in vivo. As a result, the area under the curve (AUC) of Al-ProD was approximately seven-fold increased compared with that of free DOX. The tumor accumulation of Al-ProD by extended in vivo half-life was further assessed via noninvasive near-infrared fluorescence (NIRF) imaging in breast tumor models. The breast tumor-bearing mice were prepared by subcutaneous inoculation of MDA-MB-231 cells (1×10^7) into BALB/c nude mice, and free DOX (5 mg/kg) or Al-ProD (5 mg/kg based on DOX contents) were intravenously injected into mice. In the case of free DOX, the DOX fluorescence in tumor tissues was rapidly decreased for 6 h owing to its rapid in vivo clearance by a short half-life (Figure 3.17). However, DOX fluorescence of Al-ProD in tumor tissues was significantly stronger than free DOX at all time points and was retained for 72 h of injection, which indicates high tumor accumulation by albumin-mediated passive targeting effect. The DOX fluorescence from tumor tissues was quantitatively 3.33–4.08-fold stronger in mice treated with Al-ProD than free DOX after 12 h injection (Figure 3.18). Ex vivo imaging after 12 h of injection further confirmed the high tumor accumulation of Al-ProD, wherein the DOX fluorescence in tumor tissues was 3.41–4.92-fold stronger than the free DOX group (Figure 3.19).

Finally, histological analyses also indicated strong DOX fluorescence (red color) in whole tumor tissues from mice treated with AI-ProD compared with free DOX (Figure 3.20). In contrast, only a small quantity of free DOX was observed in tumor tissues. These results demonstrate that the albumin-binding property of AI-ProD greatly extended the in vivo half-life of drugs, leading to high tumor accumulation via a passive targeting effect.



	$T_{1/2}$ (h)	AUC
Free DOX	0.25 h	272.25 ± 24.75
Al-ProD	3.1 h	1838.5 ± 98.5

Figure 3.16. Pharmacokinetics (PK) profiles of Al-ProD and free DOX. Area under the curve (AUC) was calculated by Origin 2020 software.

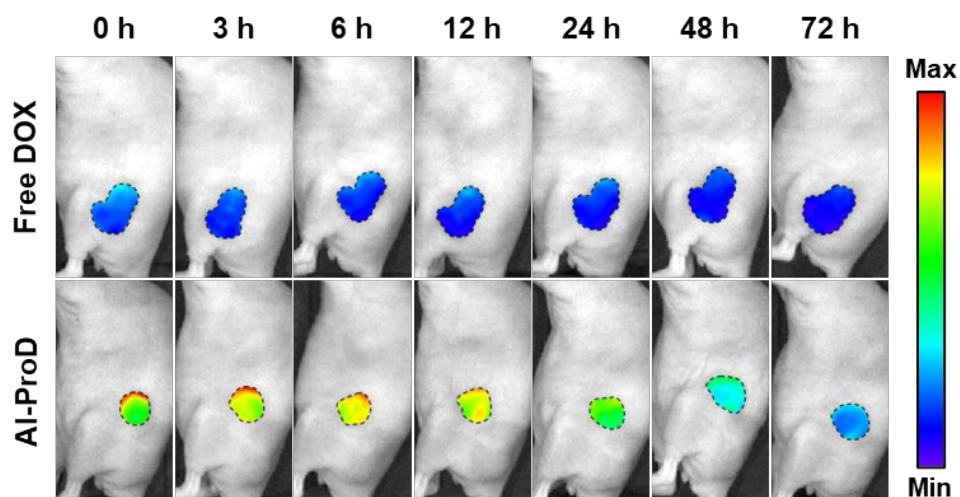


Figure 3.17. NIRF images of MDA-MB-231 tumor-bearing mice treated with AI-ProD or free DOX.

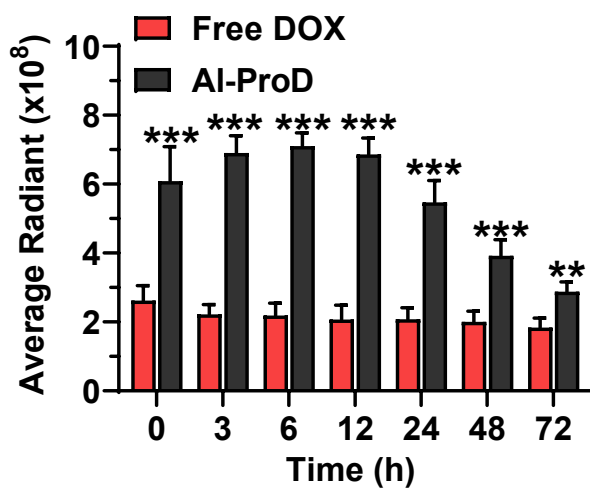


Figure 3.18. Quantification analysis on the DOX fluorescence at tumor tissues in NIRF images. Significance (** $p < 0.01$, *** $p < 0.001$) was determined by Student's t -test.

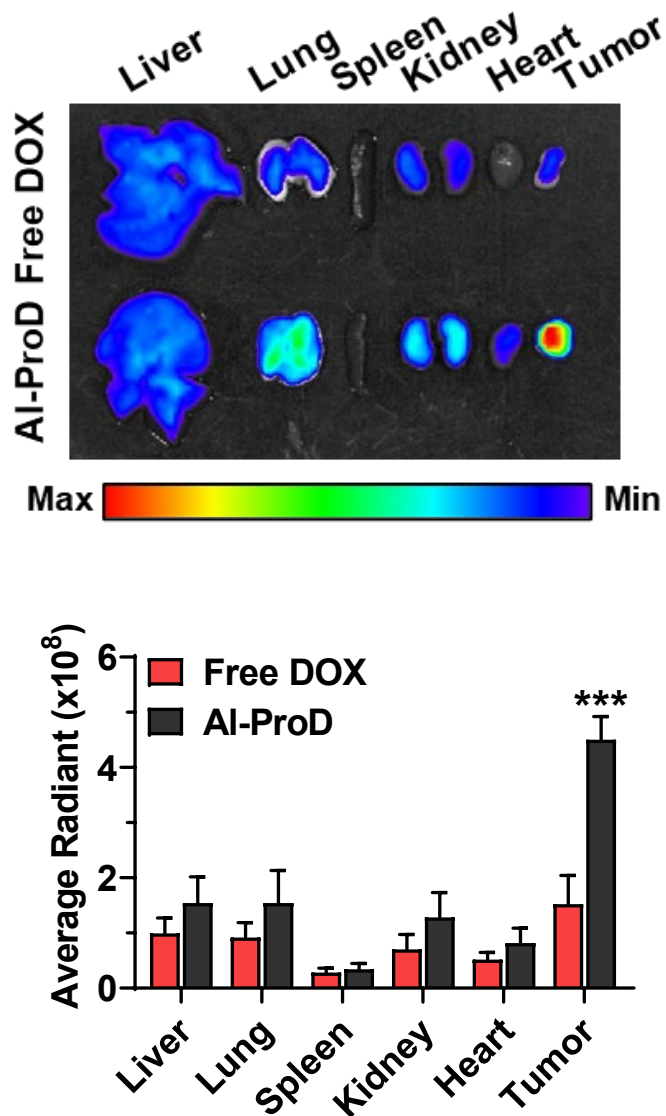


Figure 3.19. Ex vivo imaging of organs from mice treated with Al-ProD or free DOX after 12 h injection. The DOX fluorescence at major organs was quantified via Living Image software. Significance (***) $p < 0.001$ was determined by Student's t -test.

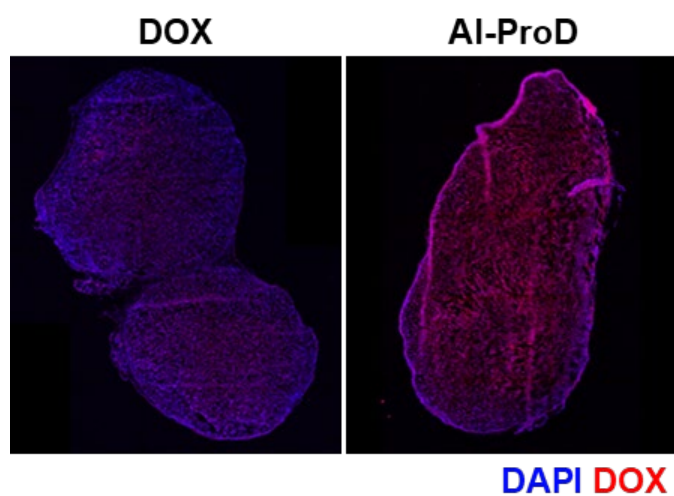


Figure 3.20. Fluorescence images of whole tumor tissues after 12 h of AI-ProD or free DOX treatment.

3.3.4. Antitumor efficacy and toxicity studies of Al-ProD in breast tumor models

To evaluate the antitumor efficacy, MDA-MB-231 tumor-bearing mice prepared by same protocol as in Figure 3.17 were treated with free DOX (5 mg/kg) or Al-ProD (5 mg/kg based on DOX contents) once every three days. Importantly, Al-ProD ($347.42 \pm 25.9 \text{ mm}^3$) significantly decreased the tumor volume compared with free DOX ($580.25 \pm 139.92 \text{ mm}^3$; $p < 0.05$) and saline ($1810.98 \pm 544.56 \text{ mm}^3$; $p < 0.001$) groups on day 20 after treatment (Figure 3.21). Tumor tissues stained with H&E and TUNEL also showed greatly elevated damaged area and apoptosis in the Al-ProD group compared with the free DOX and saline groups, which clearly indicated the potent antitumor efficacy by albumin-mediated passive targeting of Al-ProD (Figure 3.22). Next, I assessed the reduced off-target toxicity of Al-ProD by high cancer selectivity during treatment. Body weights of mice in the free DOX group gradually decreased during treatment owing to severe systemic toxicity, while those in the Al-ProD group showed no significant body weight loss, similar to the saline group (Figure 3.23). Furthermore, the mice in free DOX group were all dead within 18 days, with a median survival of 16 days, whereas Al-ProD-treated mice survived over 25 days (Figure 3.24). As a control, median survival of the saline group was measured to be 20 days, wherein the mice were dead as a result of tumor progression. In agreement with the above results, normal organs stained with H&E exhibited structural abnormalities in the free DOX group, whereas only negligible toxicity was observed in organs of the Al-ProD group on day 20 after treatment (Figure 3.25). Collectively, my findings demonstrate that Al-ProD effectively inhibits tumor growth without side effects, thereby allowing effective and safe chemotherapy.

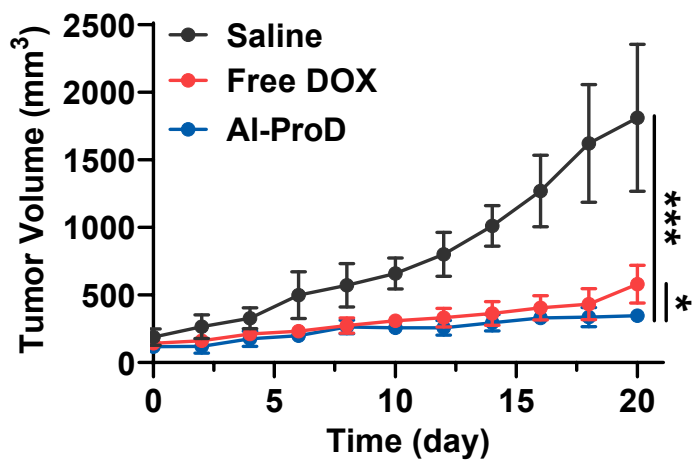


Figure 3.21. Tumor growth curves of MDA-MB-231 tumor-bearing mice after saline, free DOX, or Al-ProD treatment once every three days. Significance (* $p < 0.05$, *** $p < 0.001$) was determined by Student's t -test.

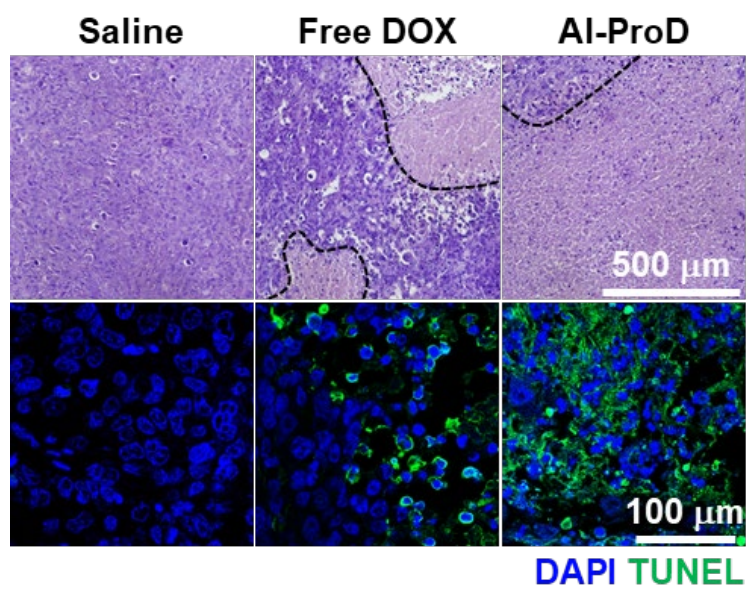


Figure 3.22. Tumor tissues stained with H&E or TUNEL to assess antitumor efficacy on day 20 after treatment.

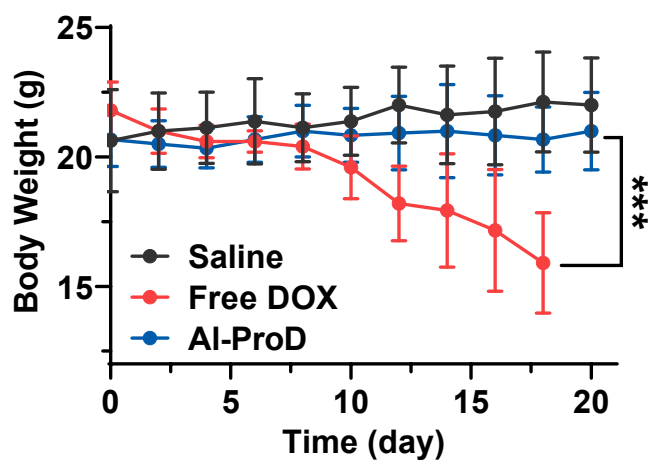


Figure 3.23. Body weights during treatment. Significance (***) $p < 0.001$ was determined by Student's *t*-test.

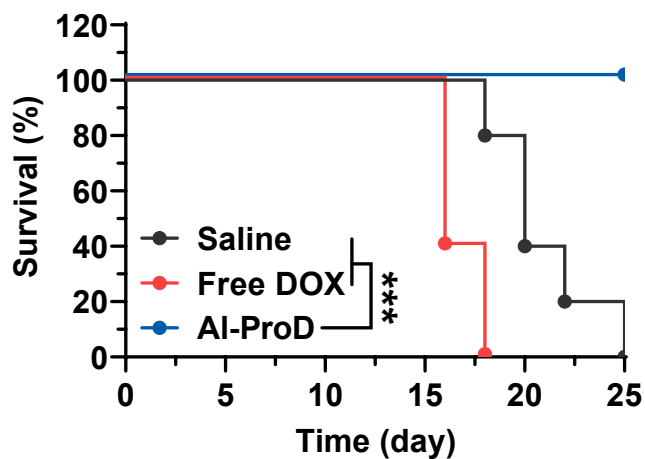


Figure 3.24. Mice survival during treatment. Significance (***) $p < 0.001$ was determined by Student's *t*-test.

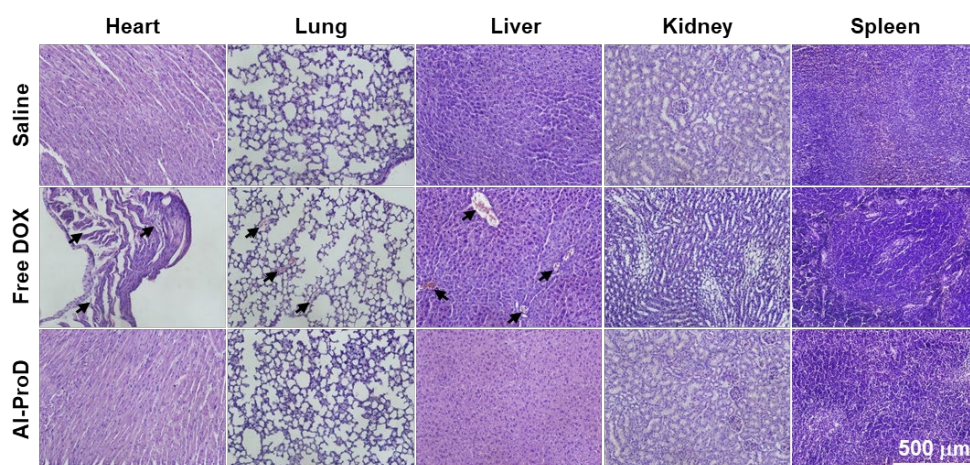


Figure 3.25. Major organs stained with H&E to assess structural abnormalities on day 20 after treatment.

3.4. Conclusions

In summary, I proposed achieving the effective and safe chemotherapy with cathepsin B-overexpressed tumor cell activatable albumin-binding doxorubicin prodrug (Al-ProD) via albumin-mediated drug delivery. Al-ProD, which consists of albumin-binding maleimide, cathepsin B-cleavable peptide, and doxorubicin, efficiently bound to plasma albumin, thereby dramatically extending the in vivo half-life of doxorubicin. Importantly, highly accumulated Al-ProD in the tumor tissues via albumin-mediated passive targeting selectively released doxorubicin in cathepsin B-overexpressed cancer cells, which provoked potent antitumor efficacy. Concurrently, Al-ProD significantly reduced the toxicity against normal tissues with innately low cathepsin B by maintaining an inactive state. As a result, localized tumor delivery of doxorubicin by Al-ProD greatly inhibited the breast tumor progression with minimized side effects. Compared with the conventional drug delivery system that encapsulates active drugs into nanoparticles, Al-ProD can prevent the off-target toxicities by accidental drug leakage during circulation. In addition, this system also reduces the risk of potential side effects from carrier materials by using the natural delivery carrier. Finally, precise and concise structures allow the simple preparation protocol, thereby overcoming the fundamental problems of targeted drugs for clinical translation, such as difficulty in quality control (QC) and mass production. Therefore, this study provides a promising approach for effective and safe chemotherapy, which may open new avenues for drug design and provide significant advances for translational nanomedicine. However, unexpectedly low delivery efficiency of targeted drugs is still a common limitation of current drug delivery systems. Thus, many researchers are making efforts

to develop the advanced formulation and to increase the understanding of the complex tumor microenvironment that reduces the delivery efficiency of targeted drugs. Considering the clinical success of albumin-mediated drug delivery to improve the pharmacokinetics and tumor targeting of drugs as well as ongoing pipelines like Al-ProD will further move albumin-binding drugs from bench to bedside.

3.5. References

1. Zhong, L., et al., Small molecules in targeted cancer therapy: advances, challenges, and future perspectives. *Signal Transduction and Targeted Therapy*, 2021. 6(1).
2. Senapati, S., et al., Controlled drug delivery vehicles for cancer treatment and their performance. *Signal Transduction and Targeted Therapy*, 2018. 3.
3. Kim, J., et al., Combination of cancer-specific prodrug nanoparticle with Bcl-2 inhibitor to overcome acquired drug resistance. *Journal of Controlled Release*, 2021. 330: p. 920-932.
4. Liu, B.Y., et al., Trackable Water-Soluble Prodrug Micelles Capable of Rapid Mitochondrial-Targeting and Alkaline pH-Responsive Drug Release for Highly Improved Anticancer Efficacy. *Acs Macro Letters*, 2019. 8(6): p. 719-723.
5. Sun, H.L. and Z.Y. Zhong, 100th Anniversary of Macromolecular Science Viewpoint: Biological Stimuli-Sensitive Polymer Prodrugs and Nanoparticles for Tumor-Specific Drug Delivery. *Acs Macro Letters*, 2020. 9(9): p. 1292-1302.

6. Wu, L. and X.G. Qu, Cancer biomarker detection: recent achievements and challenges. *Chemical Society Reviews*, 2015. 44(10): p. 2963-2997.
7. Choi, J., et al., Visible-Light-Triggered Prodrug Nanoparticles Combine Chemotherapy and Photodynamic Therapy to Potentiate Checkpoint Blockade Cancer Immunotherapy. *Acs Nano*, 2021. 15(7): p. 12086-12098.
8. Lock, L.L., et al., Enzyme-Specific Doxorubicin Drug Beacon as Drug-Resistant Theranostic Molecular Probes. *Acs Macro Letters*, 2015. 4(5): p. 552-555.
9. Um, W., et al., Visible light-induced apoptosis activatable nanoparticles of photosensitizer-DEVD-anticancer drug conjugate for targeted cancer therapy. *Biomaterials*, 2019. 224.
10. Wang, Y., et al., Peptide-drug conjugates as effective prodrug strategies for targeted delivery. *Advanced Drug Delivery Reviews*, 2017. 110: p. 112-126.
11. Wong, B.S., et al., Carbon nanotubes for delivery of small molecule drugs. *Advanced Drug Delivery Reviews*, 2013. 65(15): p. 1964-2015.
12. Chung, S.W., et al., Highly potent monomethyl auristatin E prodrug activated by caspase-3 for the chemoradiotherapy of triple-negative breast cancer. *Biomaterials*, 2019. 192: p. 109-117.
13. Chaudhury, C., et al., The major histocompatibility complex-related Fc receptor for IgG (FcRn) binds albumin and prolongs its lifespan. *Journal of Experimental Medicine*, 2003. 197(3): p. 315-322.
14. Elsadek, B. and F. Kratz, Impact of albumin on drug delivery - New applications on the horizon. *Journal of Controlled Release*, 2012. 157(1): p. 4-28.

15. Lim, S., et al., Recent advances and challenges of repurposing nanoparticle-based drug delivery systems to enhance cancer immunotherapy. *Theranostics*, 2019. 9(25): p. 7906-7923.
16. Torchilin, V., Tumor delivery of macromolecular drugs based on the EPR effect. *Advanced Drug Delivery Reviews*, 2011. 63(3): p. 131-135.
17. Eilber, F.C., et al., Administration of aldoxorubicin and 14 days continuous infusion of ifosfamide/mesna in metastatic or locally advanced sarcomas. *Journal of Clinical Oncology*, 2017. 35.
18. Hare, J.I., et al., Challenges and strategies in anti-cancer nanomedicine development: An industry perspective. *Advanced Drug Delivery Reviews*, 2017. 108: p. 25-38.
19. Sachdev, E., D. Sachdev, and M. Mita, Aldoxorubicin for the treatment of soft tissue sarcoma. *Expert Opinion on Investigational Drugs*, 2017. 26(10): p. 1175-1179.
20. Shim, M.K., et al., Cathepsin B-Specific Metabolic Precursor for In Vivo Tumor-Specific Fluorescence Imaging. *Angewandte Chemie-International Edition*, 2016. 55(47): p. 14698-14703.
21. Shim, M.K., et al., Cancer-specific drug-drug nanoparticles of pro-apoptotic and cathepsin B-cleavable peptide-conjugated doxorubicin for drug-resistant cancer therapy. *Biomaterials*, 2020. 261.
22. Shim, M.K., et al., Carrier-free nanoparticles of cathepsin B-cleavable peptide-conjugated doxorubicin prodrug for cancer targeting therapy. *Journal of Controlled Release*, 2019. 294: p. 376-389.

23. Kim, J., et al., The safe and effective intraperitoneal chemotherapy with cathepsin B-specific doxorubicin prodrug nanoparticles in ovarian cancer with peritoneal carcinomatosis. *Biomaterials*, 2021. 279.
24. Yang, S., et al., Cancer-activated doxorubicin prodrug nanoparticles induce preferential immune response with minimal doxorubicin-related toxicity. *Biomaterials*, 2021. 272.
25. Yang, F., et al., Doxorubicin, DNA torsion, and chromatin dynamics. *Biochimica Et Biophysica Acta-Reviews on Cancer*, 2014. 1845(1): p. 84-89.

Chapter 4. In situ albumin-binding and esterase-specifically cleaved BRD4-degrading PROTAC for targeted cancer therapy

4.1 Introduction

Proteolysis-targeting chimeras (PROTACs) are versatile small molecular therapeutic agents for cancer treatment via inducing the selective degradation of cancer-associated proteins. They have a heterobifunctional molecular structure where a ligand for the protein of interest (POI) and E3 ubiquitin ligase (E3) recruiter are chemically conjugated with each other [1, 2]. When PROTACs are internalized to cancer cells, they induce the polyubiquitination of POIs through concurrently binding to E3s and POIs, and polyubiquitinated POIs are degraded into oligomeric peptides by proteasomes. After the dissociation, PROTACs can be further recycled to participate in the degradation of other POIs [3]. Due to their unique mode of action (MOA), PROTACs can silence POIs in more catalytic, irreversible, and long-lasting manners, successfully overcoming the tumor drug resistance caused by the re-activation and mutation of proteins [1]. Furthermore, PROTACs are effective even in the treatment of ‘undruggable’ proteins since they are not required to access active sites of POIs [4, 5]. However, PROTACs have some issues in their biodistribution and cell permeation properties due to their hydrophobic and small molecular structures, which greatly diminishes their efficacy in anticancer therapy [6, 7].

To improve the pharmacokinetic and pharmacodynamic properties of PROTACs, nanomaterials including micelles, liposomes, and nanoparticles have been recently evaluated as their carriers [8, 9]. The use of nanomaterials was found to be somewhat effective in resolving the poor water solubility and short circulation time of PROTACs in vivo. These nanomaterials, however, often have limited drug loading capacity and may generate carrier-associated toxicity or immune reaction [10, 11]. Moreover, the complex structural and compositional heterogeneity of nanomaterials makes it hard not only to estimate their pharmacokinetic properties but also to control their quality in mass production for clinical application [12]. Although active targeting modalities including antibodies, aptamers, and ligands have also been explored as PROTAC carriers, most of them are costly and have limited drug loading amounts due to their bulky structures [13, 14]. In addition, the delivery efficiency of nanomaterials or active targeting modalities to target tissues does not exceed 1-2%, and the remains would be accumulated in off-target tissues to induce carrier-attributed toxicities [11, 15]. Therefore, a novel method different from traditional drug carriers is urged for the efficient delivery of PROTACs.

Albumin is a major plasma protein that plays an important role in the transport of nutrient sources [16]. Including its high biocompatibility and biodegradability, albumin has several favorable characteristics allowing itself to be used as a drug carrier. As drugs are loaded to albumin, their poor pharmacokinetic properties can be modulated, thereby extending their circulation time [17, 18]. Furthermore, albumin tends to selectively accumulate in tumor tissues utilizing both passive and active targeting pathways [19]. The highly permeable vasculature and lack of lymphatic drainage in tumor microenvironments contribute to the prolonged retention of albumin,

and cancer cells under stress conditions actively uptake the accumulated albumins to utilize them as nutrition sources [20]. In addition to the non-specific pinocytosis of albumin, several tumor-overexpressing receptors including glycoprotein 60 (GP60) and secreted protein acidic and rich in cysteine (SPARC) were reported to be involved in the intense albumin uptake and catabolism of cancer cells [18, 21]. Various approaches have been conducted to exploit albumins as drug carriers, and among them, the in situ covalent binding of drugs to the unpaired thiol of the 34th cysteine residue (Cys34) in albumin is considered the most effective [22, 23]. The introduction of maleimide moieties to drug molecules enables their immediate and site-specific binding to Cys34 of albumins via the thiol-maleimide (Thiol-Mal) click reaction [24]. Since the Thiol-Mal click reaction is feasible even under physiological conditions, the maleimide-conjugated drug molecules can conveniently ‘hitchhike’ native albumins without damaging their structures.

Herein, the in situ albumin-binding PROTAC was newly developed by conjugating the esterase-cleavable maleimide linker (ECMal) to bromodomain 4 (BRD4)-degrading PROTAC, resulting in ECMal-PROTAC. The BRD4-degrading PROTAC (ARV-771) is used as a model PROTAC as it has been reported to be advantageous in cancer treatment by inducing BRD4 deficiency-related cancer apoptosis [25]. To make ECMal-PROTAC, ARV-771 consisting of BRD4 targeting ligand and E3 ubiquitin ligase (E3) recruiter was firstly modified with 5-azidovaleric acid to form esterase-cleavable ester bond (N₃-PROTAC), then maleimide moiety was subsequently conjugated to N₃-PROTAC via click chemistry (Figure 4.1a). The resulting ECMal-PROTACs can ‘hitchhike’ albumins in the blood plasma and be cleaved to release free BRD4-PROTACs by the esterase after they are internalized to

targeted tumor cells (Figure 4.1b). The in situ albumin binding of ECMal-PROTACs was expected not only to prolong their circulation time but also to improve their specific accumulation in tumors via the enhanced permeation and retention (EPR) effect (Figure 4.2a). Moreover, albumins were supposed to be rapidly taken up by cancer cells, efficiently delivering ECMal-PROTACs intracellularly (Figure 4.2b). After their endocytosis and esterase-mediated cleavage, the discharged free ARV-771 in tumor cells would repeatedly and irreversibly degrade BRD4, eventually provoking the BRD4 deficiency-related tumor apoptosis (Figure 4.2c). For the validation of this hypothesis, the BRD4-degrading ECMal-PROTAC was synthesized using ECMal and its physicochemical properties, albumin binding ability, and esterase-specific cleavage are characterized in vitro. The endocytosis, intracellular BRD4 degradation, and thereby apoptosis induction of ECMal-PROTAC were also assessed against 4T1 cancer cells. Finally, the ECMal-PROTAC was intravenously administered to tumor-bearing mice to determine the improvement in its biodistribution and anticancer efficacy according to the presence of albumin-binding moiety.

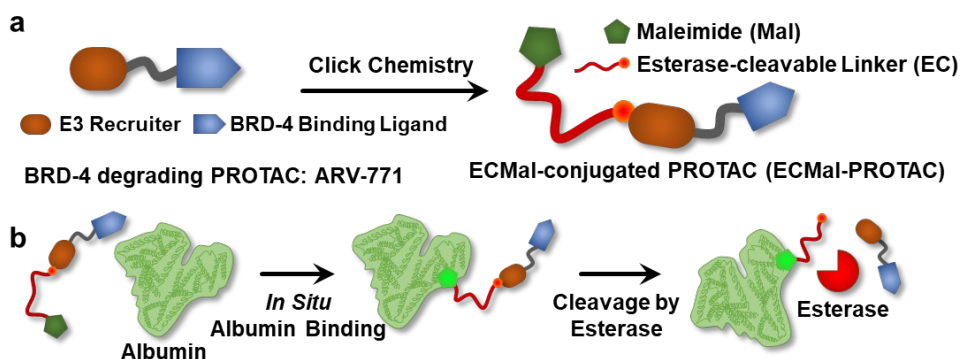


Figure 4.1. Schematic illustration for the MOA of ECMal-PROTAC. (a) In situ albumin-binding esterase-cleavable BRD4-degrading PROTAC (ECMal-PROTAC) was developed by conjugating the ECMal linkers to ARV-771 molecules via two synthetic steps. (b) ECMal-PROTACs administered in blood vessels spontaneously bind to plasma albumins via stie-specific Thiol-Mal reaction, and the maleimide linkers in ECMal-PROTACs are cleaved by esterase to recover the free form of ARV-771s after they are internalized to cancer cells.

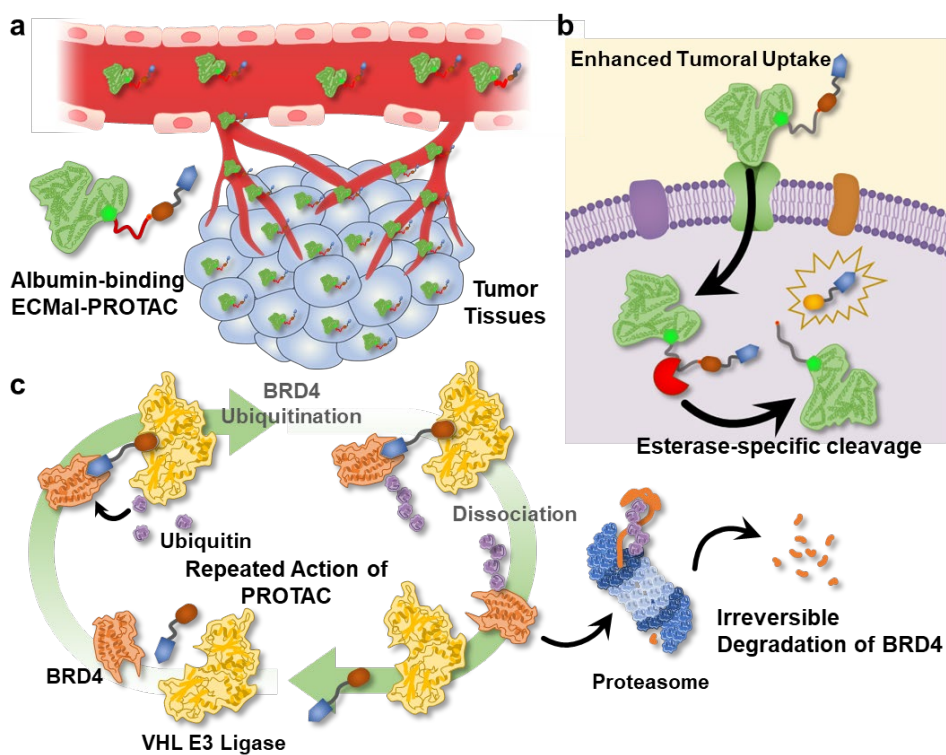


Figure 4.2. Schematic illustration for the In vivo MOA of ECMal-PROTAC. (a) Through the in situ albumin binding, ECMal-PROTACs can be improved with their blood half-lives and selectively accumulated in tumor tissues via the EPR effect. (b) The albumin-bound ECMal-PROTACs are actively internalized to cancer cells and cleaved to recover free ARV-771s. (c) The free ARV-771s concurrently bind both BRD4 and VHL E3 ligase, inducing the polyubiquitination of BRD4. Afterward, the BRD4/ARV-771/E3 ligase complexes are dissociated and the polyubiquitinated BRD4 is degraded into oligopeptides as it is recognized by the proteasome. The dissociated ARV-771s are recycled to participate in the degradation of another BRD4.

4.2. Materials and Methods

4.2.1. Materials

ARV-771 (99.02%) was obtained from Chemscene (Monmouth Junction, NJ, USA), and *N,N*-dimethylformamide (DMF; 99.8%), *N*-(3-dimethylaminopropyl)-*N*'-ethylcarbodiimide hydrochloride (EDC-HCl), 4-dimethylaminopyridine (DMAP; 99%), esterase from porcine liver, and triethylamine (TEA; 99.5%) were purchased from Sigma-Aldrich (St. Louis, MO, USA). 5-azidovaleric acid (98%), 4-maleimidobutyric acid (98%), and 2-mercaptoethanol (98%) were commercially available from Tokyo Chemical Industry (TCI; Toshima, Tokyo, Japan). Bicyclononyne-polyethylene glycol-maleimide (BCN-PEG₂-Mal; 95%) was obtained from Axispharm (San Diego, CA, USA), and acetonitrile (ACN) was purchased from Honeywell (Charlotte, NC, USA). Dimethyl sulfoxide (DMSO; 99%), bovine serum albumin (BSA; 98%), and TWEEN 20 were obtained from Biosesang (Ansan, Gyeonggi, Republic of Korea). Cyanine 5.5-N-hydroxysuccinimide ester (Cy5.5-NHS) and cyanine 5.5-carboxylic acid (Cy5.5-COOH) were purchased from Lumiprobe (Hunt Valley, MD, USA), and anti-BRD4, anti-c-Myc, anti-Bcl-2, and anti- β -actin antibodies were available from Abcam (Discovery Drive, Cambridge, United Kingdom). Cell counting kit-8 (CCK-8) was purchased from Vitascientific (Beltsville, MD, USA), and Roswell Park Memorial Institute (RPMI) 1640 medium, fetal bovine serum (FBS), penicillin, and streptomycin were commercially available from WELGENE Inc. (Daegu, Republic of Korea). 4T1 (mouse breast cancer cells) cell line was obtained from American Type Culture Collection (ATCC; Manassas, VA, USA).

Five-week-old female Balb/c and Balb/c nu/nu mice were purchased from NaraBio, Inc (Seoul, Republic of Korea). All chemical agents were used as received.

4.2.2. Instruments

The completion of each synthetic step, the albumin binding of ECMal-PROTAC, and the cleavage of ECMal-PROTAC under the presence of esterase were analyzed with reversed-phase high-performance liquid chromatography (RP-HPLC; 1200 series, Agilent Technologies, Palo Alto, CA, USA) equipped with a C18 column (Eclipse XDB-C18, 4.6 × 150 mm, particle size = 5 µm, Agilent Technologies). The molar masses of products in every synthetic procedure and the ECMal-PROTAC-bound albumin were confirmed with liquid chromatography-mass spectroscopy (LC-MS; Q-TOF 5600, AB SCIEX, Framingham, MA, USA) and expressed as their mass-to-charge ratios (m/z). The hydrodynamic size of albumin was measured through dynamic light scattering (DLS; Zetasizer Nano ZS, Malvern Instruments, Malvern, UK). The chemical conjugation of FITC or Cy5.5 dye to ARV-771 or BSA was verified with a fluorescence spectrophotometer (FL; Hitachi F-7000, Hitachi High-Tech, Hitachinaka, Ibaraki, Japan). A confocal laser scanning microscope (CLSM; Leica TCS SP8, Leica Microsystems GmbH, Wetzlar, Germany) and a microplate reader (VERSAmax™, Molecular Devices Corp., Sunnyvale, CA, USA) were used to observe the in vitro endocytosis and intracellular activity of ECMal-PROTAC. To investigate the in vivo and ex vivo biodistribution of ECMal-PROTAC, an IVIS Lumina Series III system (PerkinElmer, Waltham, MA, USA) was utilized with Living Image software (PerkinElmer).

4.2.3. Synthesis of ECMal-PROTAC

The ARV-771 (20.0 mg, 20.27 μmol) was placed into a 3 mL 1-neck round-bottom flask equipped with a magnetic stirrer bar and dissolved in 0.5 mL anhydrous DMF. 5-azidovaleric acid (7.25 mg, 50.68 μmol), DMAP (12.38 mg, 101.35 μmol), and EDC-HCl (15.73 mg, 101.35 μmol) were successively introduced to the flask and the mixture was allowed to react with a gentle stirring at room temperature (RT) for 12 h. The resulting crude was concentrated under reduced pressure and separated via C18 column chromatography (Sep-Pak® C18 cartridges 5 g; Waters Corporation, Milford, MA, USA) with an eluent of ACN/H₂O (70/30, v/v) to obtain the N₃-PROTAC, and the collected N₃-PROTAC was furtherly lyophilized to remove residual solvents.

For the synthesis of ECMal-PROTAC, N₃-PROTAC (20.0 mg, 17.99 μmol) was put into a 3 mL 1-neck round-bottom flask and dissolved in 0.5 mL DMSO. The BCN-PEG₂-Mal (12.8 mg, 26.98 μmol) was then added to the solution and the reaction was carried out at RT for 2 h. The crude product was passed through a C18 preparative column of RP-HPLC with a gradient elution of ACN/H₂O from 20/80 to 80/20 (v/v), and lyophilized to isolate the pure ECMal-PROTAC powder. Products for each synthetic step were confirmed via RP-HPLC and LC-MS analysis.

4.2.4. In vitro albumin binding and dissociation test with ECMal-PROTAC

The time-dependent albumin binding rate of ECMal-PROTAC was monitored via the RP-HPLC. In brief, a BSA solution in PBS (200 μM) was co-incubated with an ECMal-PROTAC solution (140 μM) in a 1:1 volume ratio. The reaction was quenched with mercaptoethanol at time points of 0, 5, 30, and 60 min, and the HPLC spectra of the mixture were acquired at each time point using a gradient elution mode (ACN/H₂O,

20/80 to 80/20 (v/v), 30 min). The albumin-binding rate of ECMal-PROTAC was calculated by quantifying the changes in integrities of peaks corresponding to the ECMal-PROTAC over time. After the evaluation, the albumin-binding ability of ECMal-PROTAC was reaffirmed by comparing the LC-MS spectra of free BSA and the resulting BSA-bound ECMal-PROTAC (Alb-ECMal-PROTAC). The sizes of albumins in PBS media before and after the ECMal-PROTAC binding were also measured using DLS. Next, the cleavage of the Alb-ECMal-PROTAC with the esterase treatment was performed and the release of free ARV-771 was observed in vitro. The Alb-ECMal-PROTAC was prepared in the same way as the albumin-binding rate measurement and the solution was adjusted to pH 8.0. 15 units of esterase were subsequently added to 0.2 mL of the Alb-ECMal-PROTAC solution, and the mixture was investigated with RP-HPLC at time points of 0, 3, 6, and 9 h to detect the peak corresponding to free ARV-771.

4.2.5. Preparation of Cy5.5-conjugated ARV-771 and BSA

Cy5.5-conjugated ARV-771 and BSA were synthesized to examine the in vitro cellular uptake, in vivo pharmacokinetics, and biodistribution of ARV-771 and Alb-ECMal-PROTAC. Briefly, ARV-771 (5 mg, 5.07 μ mol), Cy5.5-COOH (5.8 mg, 7.60 μ mol), and DMAP (3.1 mg, 25.34 μ mol) were put into a 4 mL vial and dissolved in 1 mL anhydrous DMF. The EDC-HCl (3.9 mg, 25.34 μ mol) was subsequently introduced into the vial to activate the carboxylic acid group of Cy5.5-COOH, and the reaction was performed at RT for 12 h. The crude product was passed through a C18 column using an eluent of ACN/H₂O (40/60) to collect pure Cy5.5-conjugated ARV-771 (Cy5.5-ARV-771). To produce Cy5.5-labeled BSA (Cy5.5-Alb), unlabeled BSA (66.5 mg, 1.00

μmol), and Cy5.5-NHS (0.1 mg, 0.10 μmol) were dissolved in 10 mL anhydrous DMF and their reaction proceeded at RT for 12 h. After the reaction, the mixture was diluted with H_2O , dialyzed using a membrane bag (MWCO = 10,000 Da), and lyophilized to collect pure Cy5.5-Alb with a 1:10 molar ratio of Cy5.5 and BSA. The fluorescence intensities of Cy5.5-ARV-771 and Cy5.5-Alb were quantified with FL, and Cy5.5-ARV-771 was further blended with native ARV-771 to adapt the molar ratio of Cy5.5 and ARV-771 to 1:10. Before using them for in vivo biodistribution test, Cy5.5-Alb was also mixed with ECMal-PROTAC to yield Cy5.5-Alb-bound ECMal-PROTAC (Cy5.5-Alb-ECMal-PROTAC).

4.2.6. In vitro cellular uptake and cell viability of ECMal-PROTAC

The cellular uptake and cytotoxic effect of ARV-771 and Alb-Mal-RPOTAC were observed using a 4T1 mouse breast cancer cell line. 1×10^5 4T1 cells were seeded in a glass-bottom confocal dish (35 mm in diameter) and cultured with RPMI for 24 h. After the stabilization, cells were treated with Cy5.5-ARV-771 (5 μM) or Cy5.5-Alb-ECMal-PROTAC (5 μM) at 37 °C for 1, 3, 6, and 12 h. The cells were then washed three times with PBS, fixed with a 4% formaldehyde solution for 15 min, and their nuclei were stained with 4',6-diamidino-2-phenylindole (DAPI) for 10 min. Fluorescence signals from DAPI and Cy5.5 in 4T1 cells were monitored through a CLSM to assess the time-dependent cellular uptake of ARV-771 and Alb-ECMal-PROTAC. The relative intracellular fluorescence intensities from Cy5.5 were also calculated using Image-Pro software (Media Cybernetics, Rockville, MD, USA), and their changes were plotted as a function of time.

The dose-dependent cytotoxicity of ARV-771 and ECMal-PROTAC was investigated via the cell counting kit-8 (CCK-8) assay. 4T1 cells were separately plated in 96-well culture plates at 3×10^3 cells for each well and preserved at 37 °C and 5% carbon dioxide atmosphere for 24 h. The cells were then treated with different concentrations (0.01 to 100 µM) of ARV-771 or ECMal-PROTACs for 48 h, respectively, and successively exposed to 10% CCK-8-containing culture media for 30 min. The viability of ARV-771- or ECMal-PROTAC-treated 4T1 cells was analyzed with a microplate reader. The alteration of cell viability according to the concentration of ARV-771 or ECMal-PROTAC was drawn and fitted using GraphPad Prism 8 software (GraphPad Software, San Diego, CA, USA) to determine their half-maximal inhibitory concentration (IC₅₀) values.

4.2.7. Western blot analysis

The elimination of BRD4 and other associated proteins such as c-Myc and Bcl-2 with the ARV-771 or ECMal-PROTAC treatment was assessed via their western blot assay. 1×10^5 4T1 cells were cultured in each well of 6-well culture plates and maintained at 37 °C and 5% carbon dioxide atmosphere for 24 h. Subsequently, the cells were incubated with various concentrations of ARV-771 (0 to 10 µM) or ECMal-PROTAC (0 to 10 µM) at 37 °C for 24 h, washed with PBS three times, and lysed with 1% protease-containing lysis buffer. The cell debris in the resulting lysates was then removed via centrifugation at 12,000 rpm for 25 min, and the supernatants were assessed with a BCA kit to quantify proteins in them. The supernatants were loaded onto 10% sodium dodecyl sulfate-polyacrylamide gels, developed by electrophoresis (SDS-PAGE), and blotted onto polyvinylidenedifluoride (PVDF) membranes. After the

blotting, membranes were treated with 5% BSA-containing tris buffered saline with 0.1% Tween 20 (TBS-T) for 2 h to inhibit any indiscriminate binding of immunoglobulin G (IgG) and successively exposed to rabbit anti-mouse primary antibodies (1,000:1) at 4 °C for 24 h. Finally, membranes were washed three times with TBS-T and further incubated with HRP-conjugated mouse anti-rabbit IgG antibody for 1 h at RT. The immunoreactive bands on membranes were analyzed via an enhanced chemiluminescence (ECL) system.

4.2.8. In vivo biodistribution of ECMal-PROTAC with tumor-bearing mice

The in vivo pharmacokinetic properties and biodistribution of ARV-771 and ECMal-PROTAC were determined and compared to each other using 4T1 tumor-bearing mice. For the preparation of tumor-bearing mice, 1×10^6 4T1 cells were inoculated to the left thighs of mice ($n = 3$ for each test group) and let being proliferated until the tumor volume reached 150 - 200 mm³. Each recipient group was administered with Cy5.5-ARV-771 (3 mg/kg, equivalent to ARV-771) or Cy5.5-Alb-ECMal-PROTAC (3 mg/kg, equivalent to ARV-771), and their whole blood was drawn at certain time points (from 0 to 96 h) to examine time-dependent changes in blood circulation levels of ARV-771 and ECMal-PROTAC. The obtained blood samples were analyzed for their fluorescence intensities using IVIS Lumina Series III system and the data were expressed as a function of time with GraphPad Prism 8 software to calculate the blood half-life and area under the curve (AUC) of ARV-771 and ECMal-PROTAC. The mice in all experimental groups were also taken with their whole body fluorescence images via the IVIS Lumina Series III system at 0, 1, 3, 6, 12, and 24 h after the injection to monitor the tumor accumulation. After 24 h, mice were sacrificed

and their major organs (heart, liver, lung, spleen, and kidney) and tumor tissues were harvested to evaluate the biodistribution of ARV-771 and ECMal-PROTAC *ex vivo*. After obtaining the confocal fluorescence images of whole tumor tissues, those tissues were further stained with anti-CD31-FITC to determine the intratumoral distribution of ARV-771 and ECMal-PROTAC. All experiments with animals were performed in compliance with relevant laws and institutional guidelines of the Institutional Animal Care and Use Committee (IACUC; the approved number of 2021-143) in KIST.

4.2.9. In vivo therapeutic efficacy of ECMal-PROTAC against tumor-bearing mice

To investigate the *in vivo* therapeutic efficacy of ARV-771 and ECMal-PROTAC, 1×10^6 4T1 cells were injected into the left thighs of mice to produce 4T1 tumor-bearing mice ($n = 5$ for each test group). As tumors grew to $100 \pm 10 \text{ mm}^3$ in volume, the subject mice were treated with ARV-771 (10 mg/kg) or ECMal-PROTAC (10 mg/kg, equivalent to ARV-771) once every three days (four shots in total), and their tumor sizes and body weights were measured once every two days. 15 days after the treatment, all recipients were euthanized to extract their major organs (heart, liver, lung, spleen, and kidney) and tumors, and the digital images of excised tumors were obtained to compare their sizes. Subsequently, the western blot assay of tumor tissues was conducted to verify the BRD4-degrading activity of ECMal-PROTAC and the following suppression of downstream c-Myc and Bcl-2 proteins. Tumor tissues were further stained with their terminal deoxynucleotidyl transferase dUTP nick end labeling (TUNEL), anti-BRD4, and anti-c-Myc to observe the BRD4 deficiency-mediated cancer apoptosis. Afterward, all tissues of major organs and tumors were histologically analyzed upon staining them with hematoxylin & eosin (H&E).

4.2.10. Statistical analysis

All the statistical data in this study were denoted as mean \pm standard deviation (SD) from at least three independent trials. Statistical analysis between the two groups was performed with Student's t-test. One-way analysis of variance (ANOVA) test was used to compare more than two groups, and the statistical significance for multiple comparisons was defined with Tukey-Kramer post-hoc test. p-Values of each statistical data were indicated by asterisks (* $p < 0.05$, ** $p < 0.01$, *** $p < 0.001$, and **** $p < 0.0001$) in figures.

4.3. Results

4.3.1. Synthesis of BRD4-degrading ECMal-PROTAC

The endogenous albumin binding of PROTAC through the in situ Thiol-Mal reaction was assumed to effectively modulate the poor bioavailability of PROTAC and increase its distribution at targeted tumor tissues. For the development of albumin-binding PROTAC, esterase-specifically cleavable maleimide moiety (ECMal) was introduced into ARV-771 molecules (ECMal-PROTAC) (Figure 4.3a). ARV-771, which consists of a bromodomain 4 (BRD4) inhibitor (JQ1) and a ligand for Von Hippel-Lindau (VHL) E3 ligase, is a type of BRD4-degrading PROTAC for the cancer treatment by degrading bromodomain and extra-terminal domain (BET) proteins overexpressed in cancer cells [26]. The conjugation of ECMal linkers to ARV-771 and its albumin binding would promote its tumor-specific accumulation and cellular uptake. After being endocytosed to cancer cells, the albumin-bound ECMal-PROTAC was supposed to be degraded into free ARV-771 by the intracellular esterase and recover its BRD4-degrading activity [27]. The synthetic scheme of ECMal-PROTAC was illustrated in Figure 4.3b. Firstly, ARV-771s were conjugated with 5-azidovaleric acid via Steglich esterification to obtain azide-ARV-771s (N₃-PROTACs), then ECMal-PROTACs were prepared by the copper-free alkyne-azide click reaction between N₃-PROTACs and BCN-PEG₂-Mal. After finishing the reaction, the resulting mixture was purified with C18 column chromatography. The collected product was analyzed with high-performance liquid chromatography (HPLC) and liquid chromatography-mass spectrometry (LC-MS), demonstrating the successful synthesis of ECMal-PROTAC with high purity (N₃-PROTAC: 88.7% yield and 98.9% purity, ECMal-PROTAC: 62.9%

yield and 98.2% purity). The HPLC spectra of ARV-771, N₃-PROTAC, and ECMal-PROTAC exhibited the entire shifts of corresponding peaks after each reaction, confirming that chemical conjugations completely proceeded without any significant side reaction (Figure 4.4a). In the LC-MS analysis of ECMal-PROTAC, its *m/z* value was measured to be 1,586.7 ([M] + 1H⁺), which was precisely matched to its calculated molecular weight (1,587.32 Da) (Figure 4.4b). In addition, comparing the *m/z* values of ARV-771 (985.37 *m/z*, [M]) and ECMal-PROTAC, their difference (601.33 *m/z*, [M] + H⁺) was analogous to the calculated molecular weight of ECMal linker (601.68 Da), reassuring the successful conjugation of ECMal linker to ARV-771.

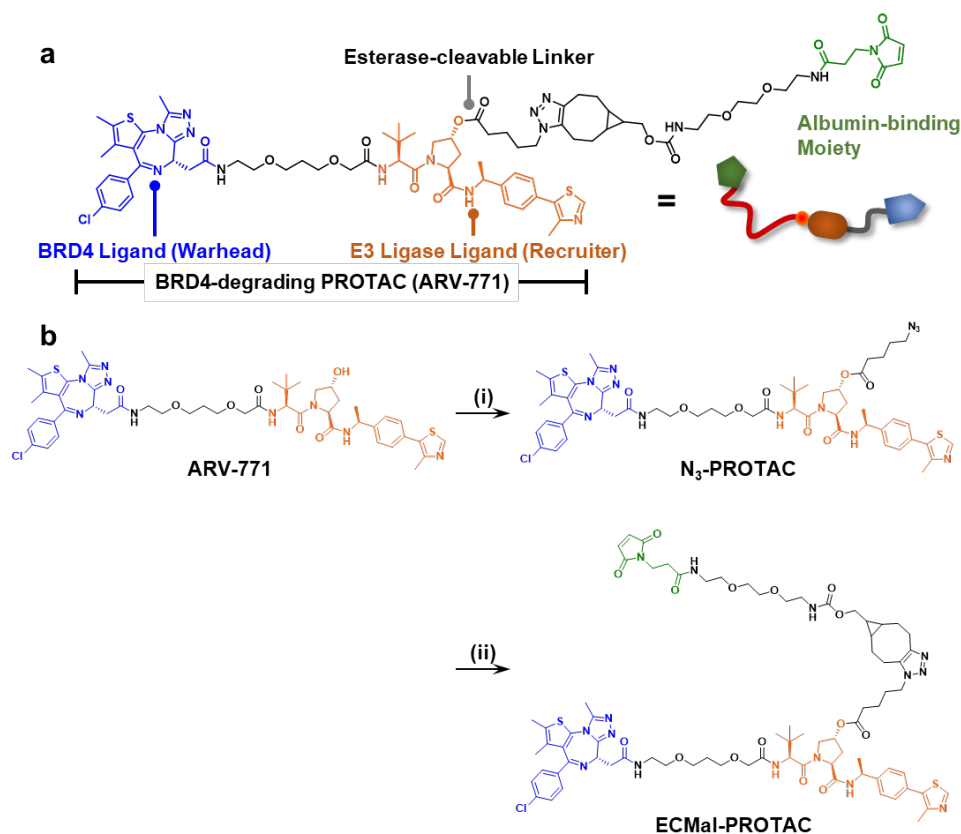


Figure 4.3. Synthesis of ECMal-PROTAC. (a) The exact chemical structure of ECMal-PROTAC. (b) Chemical synthetic steps of ECMal-PROTAC. (i) 5-azidovaleric acid, EDC, DMAP, DMF, RT, 12 h, yield 88.7%, purity 98.9%. (ii) BCN-PEG₂-Mal, MeOH, RT, 2 h, yield 62.9%, purity 98.2%.

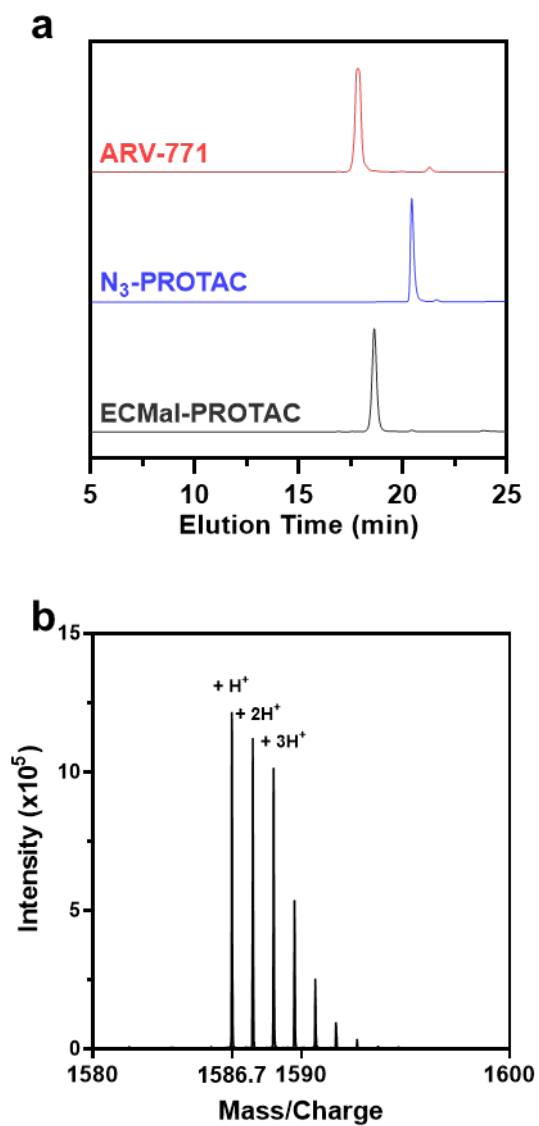


Figure 4.4. Characterization of ECMal-PROTAC. (a) HPLC spectra of ARV-771, N₃-PROTAC and ECMal-PROTAC indicated the completion of each synthetic step. (b) . LC-MS peak of synthesized ECMal-PROTAC, consistent with its theoretical value (ECMal-PROTAC: 1,586.7 m/z , $[M] + H^+$).

The albumin binding ability of ECMal-PROTAC was examined in vitro by simply mixing it with bovine serum albumin (BSA), which contains only one unpaired thiol group, similar to human serum albumin (HSA) [28]. In the RP-HPLC analysis after mixing ECMal-PROTAC (70 μ M) and BSA (100 μ M), the peak of ECMal-PROTAC rapidly decreased and that of BSA was slightly broadened, which indicated the specific and strong binding of ECMal-PROTAC to BSA (Figure 4.5a). In contrast, the free ARV-771 was confirmed not able to interact with albumin even after 60 min of mixing reaction (Figure 4.5b). The peak of ECMal-PROTAC was not diminished either when mixed with BSAs which were pre-treated with 4-maleimidobutyric acid as a cys34 blocking agent, demonstrating the site-specific reaction between ECMal-PROTAC and BSA. As quantifying the concentration decrease of unbound ECMal-PROTAC and plotting it depending on time, it was determined that over 75% of ECMal-PROTAC was conjugated to BSA during the first 3 min and the reaction was accomplished within 10 min (Figure 4.5c). Taking into account the higher albumin concentration in the blood (500-750 μ M) than that used in the albumin binding test (100 μ M), it is suggested that the intravenously injected ECMal-PROTAC would safely bind to circulating albumin before its clearance and elimination [29]. The molecular weights of albumins before and after the binding of ECMal-PROTAC were measured with LC-MS (before: 66,500 m/z , [M], after: 68,087 m/z , [M] + 1H⁺) (Figure 4.5d). The change in molecular weight according to the ECMal-PROTAC binding was determined to be 1,587 Da, which was consistent with that of ECMal-PROTAC itself (1,587 m/z , [M] + 1H⁺). When analyzing the size of albumin in PBS media via DLS, merely negligible changes were observed in the hydrodynamic volume after the ECMal-PROTAC binding (Figure 4.6). The sizes of native BSA and BSA-bound ECMal-PROTAC (Alb-

ECMal-PROTAC) were 5.43 ± 1.42 and 6.99 ± 1.38 nm, respectively, indicating that the binding of ECMal-PROTAC did not induce any decomposition or aggregation of albumin.

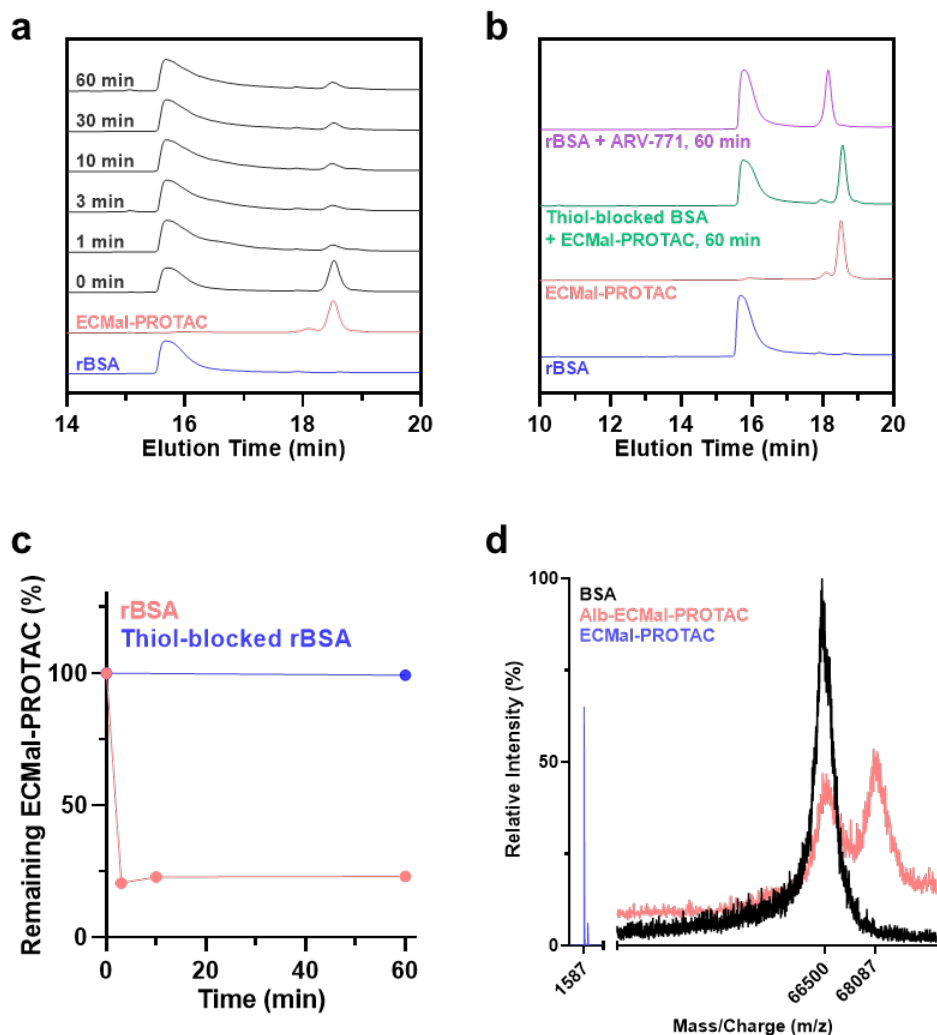


Figure 4.5. Albumin binding affinity study of ECMal-PROTAC. (a) The time-dependent changes in HPLC spectra of the BSA and ECMal-PROTAC mixture. (b) The mixture of free ARV-771 with BSA or ECMal-PROTAC with thiol-blocked BSA. (c) The decrease in HPLC peak area corresponding to ECMal-PROTAC was quantified. (d) The LC-MS peak of ECMal-PROTAC, BSA, and their mixtures. The difference in molecular weights of BSA and Alb-ECMal-PROTAC was consistent with that of ECMal-PROTAC (ECMal-PROTAC: 1,587 m/z , $[M] + 1H^+$, BSA: 66,500 m/z , $[M]$, Alb-ECMal-PROTAC: 68,087 m/z , $[M] + 1H^+$).

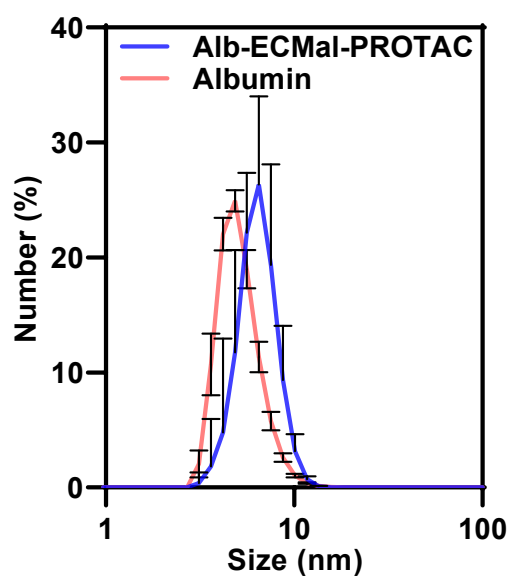


Figure 4.6. Through the DLS analysis before and after the binding of ECMal-PROTAC, it was confirmed that the ECMal-PROTAC did not induce any aggregation or decomposition of albumin.

After confirming the albumin binding ability of ECMal-PROTAC, the Alb-ECMal-PROTAC was furtherly treated with esterase to verify whether the ester bond between ARV-771 and maleimide linker can be cleaved to recover free ARV-771. For the esterase cleavage test, Alb-ECMal-PROTAC was utilized rather than the free ECMal-PROTAC since the ECMal-PROTAC would be internalized to cancer cells as its albumin-bound form in physiological conditions. In Figure 4.7, the esterase cleaved the ester bond, securing the gradual release of free ARV-771 from ECMal-PROTAC-bound albumin. The HPLC peak of released PROTAC corresponded to that of native ARV-771, assuring the restoration of its active form. The cleavage of Alb-ECMal-PROTAC was somewhat delayed as 63.2% of free ARV-771 were released within 48 h, which was attributed to the hydrophobic molecular structure of ARV-771 [30]. Its slow degradation rate was expected to be accelerated in the actual intracellular condition where acidic pH would support the hydrolysis of ester bonds [27]. Those results on the evaluation of the binding ability of ECMal-PROTAC using BSA were also considered valid for the HSA due to structural analogies of albumins derived from mammalian blood plasma [31].

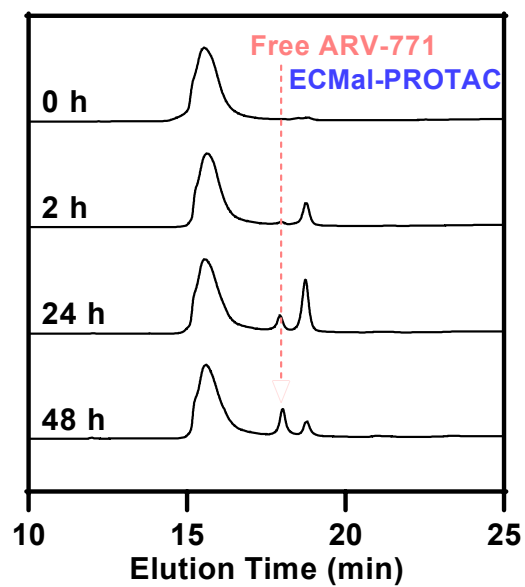


Figure 4.7. The Alb-ECMal-PROTAC was furtherly treated with an esterase solution (15 units) and monitored via HPLC, showing the release of free ARV-771 with the enzymatic activity of esterase.

4.3.2. In vitro cellular uptake, BRD4 degradability, and therapeutic effect of ECMal-PROTAC

The enhanced endocytosis of ECMal-PROTAC and the subsequent promotion of BRD4 deficiency-mediated apoptosis were monitored in vitro against 4T1 cancer cells. To visualize the cellular uptake of PROTACs, 4T1 cells were incubated with Cy5.5-conjugated ARV-771 (Cy5.5-ARV-771, 5 μ M) and Cy5.5-labeled BSA-bound ECMal-PROTAC (Cy5.5-Alb-ECMal-PROTAC, 5 μ M), respectively. The molar ratio of Cy5.5 to BSA was precisely controlled to 1:10 for the accurate comparison of fluorescence intensities. As shown in Figure 4.8, both Cy5.5-ARV-771 and Cy5.5-Alb-ECMal-PROTAC (red color) were gradually uptaken by 4T1 cells within 12 h. The endocytosed concentrations of Cy5.5-ARV-771 and Cy5.5-Alb-ECMal-PROTAC at 12 h were similar to each other, exhibiting 0.61 ± 0.11 and 0.61 ± 0.06 of relative fluorescence intensities, respectively (Figure 4.9). The cellular uptake rate of Cy5.5-Alb-ECMal-PROTAC was slightly faster than that of Cy5.5-ARV-771, suggesting that 4T1 cancer cells tend to actively uptake albumins as nutrition sources [32].

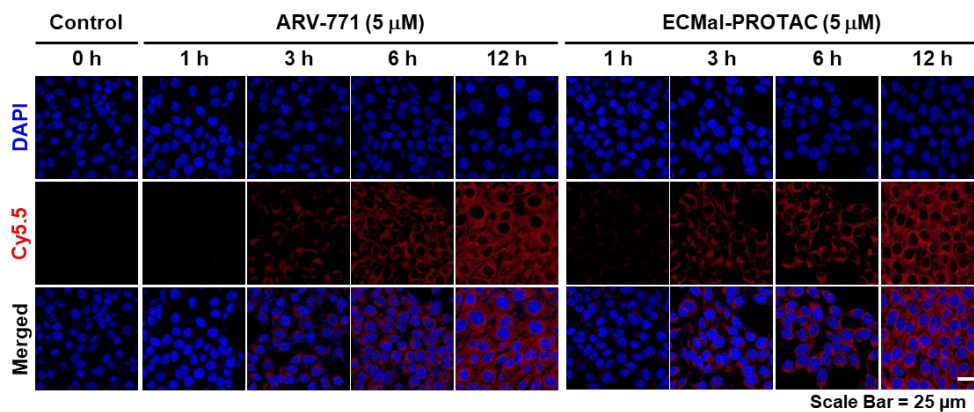


Figure 4.8. In vitro cellular uptake of ECTMaI-PROTAC. The confocal images of 4T1 cancer cells displayed higher endocytosis of Cy5.5-Alb-ECTMaI-PROTAC than that of Cy5.5-ARV-771.

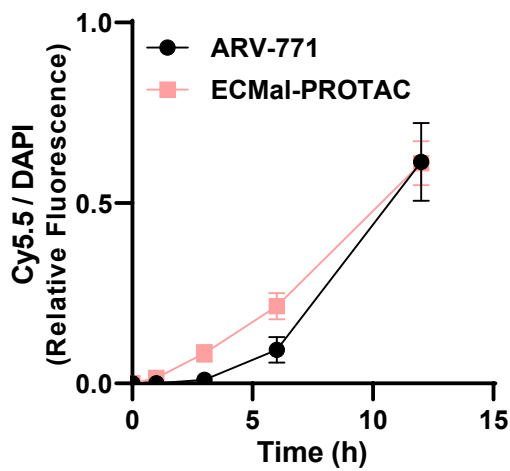


Figure 4.9. The intracellular fluorescence intensities were quantified. The internal concentration of Cy5.5-Alb-ECTMaI-PROTAC was similar to that of Cy5.5-ARV-771 at 12 h.

BRD4 is an epigenetic protein that regulates the transcription of genes at the initiation and elongation steps [33]. The transcription of cancer-associated genes is particularly dependent on BRD4, accordingly, the silencing of BRD4 in cancer cells leads to their apoptosis by inhibiting the oncogene transcription [34]. The BRD4 degradation ability of ECMal-PROTAC after its tumor internalization was assessed with western blot analysis. ECMal-PROTAC was internalized into 4T1 cells via binding to mouse serum albumins (MSAs) in a cell culture medium, and degraded the overexpressed BRD4 proteins in a concentration-dependent manner (Figure 4.10). Both free ARV-771 and ECMal-PROTAC (0 to 10 μ M) could effectively catalyze the degradation of BRD4 after 48 h post-incubation, further demonstrating the successful recovery of ECMal-PROTAC to free ARV-771 by the action of esterase. The levels of other proteins such as c-Myc and Bcl-2 were also diminished with the treatment of ECMal-PROTAC since the BRD4 played a key role in the transcription of their mRNAs [35] (Figure 4.11a). As quantifying the band of BRD4, the half-maximal degradation concentration (DC50) of ECMal-PROTAC was found to be 1.81 μ M, slightly lower than that of ARV-771 (DC50 = 3.38 μ M) (Figure 4.11b). It was deduced that the activity of ECMal-PROTAC was successfully recovered as the esterase cleaved its ECMal linker after its endocytosis.

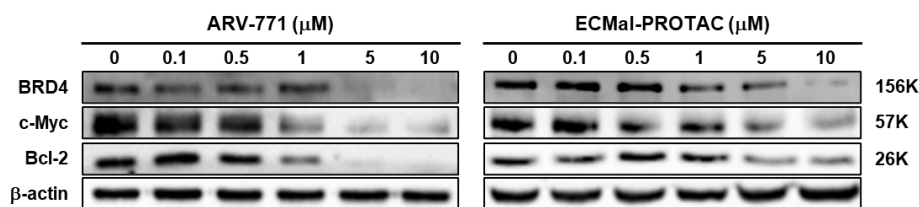


Figure 4.10. In vitro protein degradability of ECMal-PROTAC. The western blot assay after the treatment of ARV-771 or ECMal-PROTAC to 4T1 cells showed an effective degradation of BRD4 in a concentration-dependent manner, followed by the underexpression of c-Myc and Bcl-2 proteins.

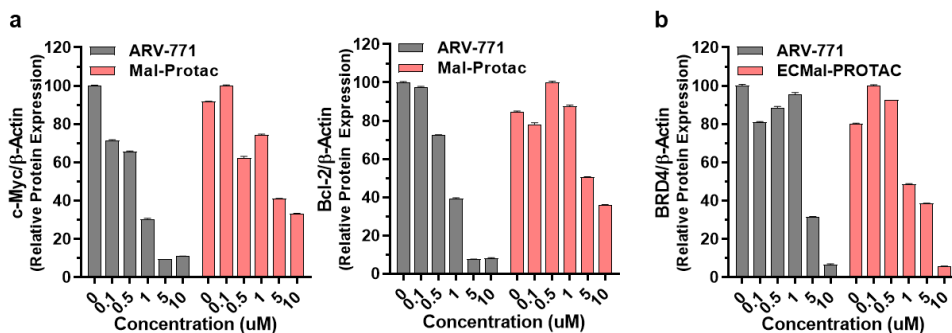


Figure 4.11. The relative expression level of (a) c-Myc, Bcl-2 and (b) BRD4 in 4T1 cells depending on the ARV-771 or ECMal-PROTAC treatment, plotted as a function of concentration.

The cytotoxicity of ECMal-PROTAC on cancer cells was verified with a cell counting kit-8 (CCK-8) assay, wherein it was treated to 4T1 cells at various concentrations (0.01 to 100 μ M) for 48 h. It showed a notable antiproliferative property against BRD4-enriched 4T1 cells with an IC₅₀ of 7.780 μ M (Figure 4.12). The endocytosed ECMal-PROTAC was thought to induce the deficiency in BRD4 and the subsequent underexpression of c-Myc and Bcl-2, which are downstream effectors of BRD4, eventually promoting tumor cell apoptosis [35]. Although there was a marginal increase in the IC₅₀ of ECMal-PROTAC compared to that of native ARV-771 (IC₅₀ = 6.375 μ M) due to the delayed activation of albumin-binding ECMal-PROTAC, it still effectively killed the cancer cell. Throughout the BRD4 degradation and tumor cell viability assays, it was demonstrated that ECMal-PROTAC can successfully recruit the VHL E3 pathway, facilitate the exhaustion of BRD4, and thereby bring about cancer cell death.

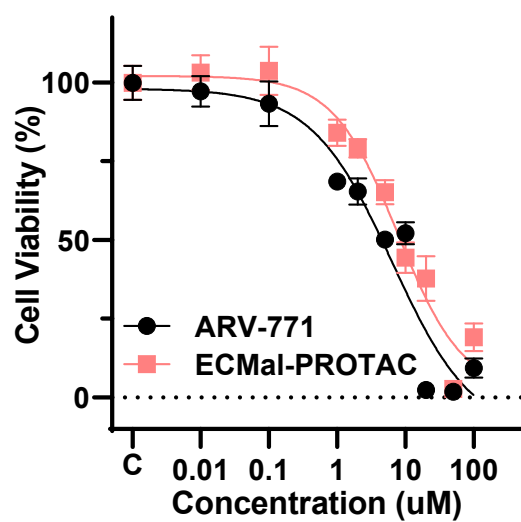


Figure 4.12. The ECMal-PROTAC elicited effective cytotoxicity to BRD4-overexpressing 4T1 cells, which was comparable to native ARV-771. All data were denoted as means \pm S.D. (n = 3).

4.3.3. In vivo biodistribution of ECMal-PROTAC in tumor-bearing mice

The biodistribution and tumor targetability of ECMal-PROTAC were investigated using BALB/c mouse models and their outcomes were compared to those of ARV-771. Firstly, the influence of albumin binding on the extended blood circulation time was evaluated by injecting the Cy5.5-conjugated ARV-771 (Cy5.5-ARV-771; 3 mg/kg, equivalent to ARV-771) or Cy5.5-labeled albumin-bound ECMal-PROTAC (Cy5.5-Alb-ECMal-PROTAC; 3 mg/kg equivalent to PROTAC) to tail veins of tumor-free BALB/c mice ($n = 3$) (Figure 4.13). The molar ratios of Cy5.5 to ARV-771 and Cy5.5 to albumin were adjusted to 1:10 to normalize the fluorescence signal. As observing their fluorescence intensities in the blood plasma, the Cy5.5-Alb-ECMal-PROTAC remained up to 12 h whereas Cy5.5-ARV-771 was totally eliminated after 1 h. The half-life of Cy5.5-Alb-ECMal-PROTAC was calculated to be 0.60 h, which was 12.8-fold longer than that of Cy5.5-ARV-771. The area under the curve (AUC) of Cy5.5-Alb-ECMal-PROTAC (635.4) was also 12.3 times larger than that of Cy5.5-ARV-771 (51.8), achieving the prolonged plasma residence time via albumin binding mechanism. It was supposed that the in situ albumin binding of ECMal-PROTAC efficiently modulated the hydrophobicity and low water solubility of PROTAC molecules, and took the advantage of GP60- and FcRn-involved albumin recycling systems as well [36].

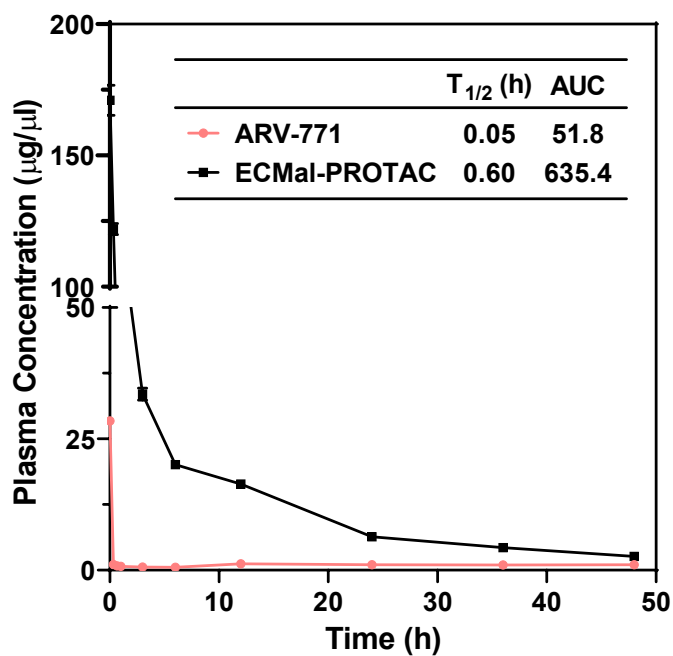


Figure 4.13. Pharmacokinetic profiles of intravenously administered Cy5.5-ARV-771 (3 mg/kg, equiv. to ARV-771) and Cy5.5-Alb-ECMal-PROTAC (3 mg/kg, equiv. to ARV-771), confirming that the albumin binding of ECMal-PROTAC significantly increased its blood half-life compared to the ARV-771. All data were denoted as means \pm S.D. (n = 3).

To monitor the tumor-specific accumulation of ECMal-PROTAC, 4T1 tumor-bearing BALB/c mice were treated with Cy5.5-Alb-ECMal-PROTAC (3 mg/kg, equivalent to ARV-771) or Cy5.5-ARV-771 (3 mg/kg, equivalent to ARV-771) intravenously after their tumor sizes grew to 150 - 200 mm³. As shown in the non-invasive near-infrared fluorescence (NIRF) imaging, the tumor-specific accumulation of Cy5.5-Alb-ECMal-PROTAC was much higher than that of Cy5.5-ARV-771 at all time points, which was attributed to the tumor-targeting ability of albumin (Figure 4.14). When quantifying the fluorescence signal in the tumoral region, Cy5.5-Alb-ECMal-PROTAC reached its highest level at 12 h after the administration and its fluorescence intensity was 12.6-fold higher than that of Cy5.5-ARV-771 (Figure 4.15). The enhanced tumor accumulation of Cy5.5-Alb-ECMal-PROTAC was thought to be dedicated by not only the increase in its elongated blood circulation time but also its passive targetability of Alb-ECMal-PROTAC. After 24 h post-injection, the biodistribution of Cy5.5-Alb-ECMal-PROTAC or Cy5.5-ARV-771 in normal organs and tumor tissues was measured via ex vivo fluorescence analysis (Figure 4.16). In the case of the Cy5.5-ARV-771, both tumors and other major organs except the kidney expressed merely weak fluorescence signals, pointing that a large portion of administered Cy5.5-ARV-771 was immediately cleared through the renal route. This result coincided well with the pharmacokinetic profile of ARV-771, showing that the poor stability of ARV-771 in a physiological condition caused its rapid renal excretion [37]. On the other hand, the fluorescence intensity from the tumor was significantly increased when applied with Cy5.5-Alb-ECMal-PROTAC. The mean fluorescence value of Cy5.5-Alb-ECMal-PROTAC in the excised tumor was determined to be 16.3-fold higher than that of Cy5.5-ARV-771, therefore, the tumor-specific deliverability of the albumin binding

approach was reassured (Figure 4.17). Moreover, the whole-tumor fluorescence images showed that the fluorescence signal by Cy5.5-Alb-ECMal-PROTAC was much brighter and more uniformly distributed throughout the tissue, compared to Cy5.5-ARV-771 (Figure 4.18). As tumor tissues were stained with DAPI (nuclei) and CD31 marker (blood vessel), it was further confirmed that Cy5.5-Alb-ECMal-PROTAC was delivered to the tumor in a greater amount and sufficiently penetrated into deep tissues rather than being dispersed just around the blood vessels (Figure 4.19). The cross-sectional fluorescence plot of Cy5.5-Alb-ECMal-PROTAC-treated tumor tissues more clearly demonstrated the inconsistency between Cy5.5 and CD31 signals (Figure 4.20). The outcomes in pharmacokinetics and biodistribution profiles of Cy5.5-Alb-ECMal-PROTAC evidenced the practical utility of albumin as a tumor-specific PROTAC carrier with prolonged blood circulation and enhanced tumor accumulation.

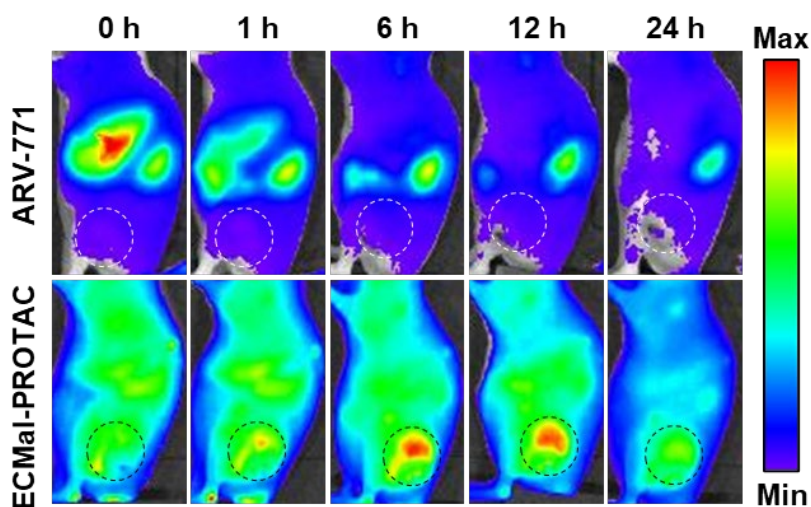


Figure 4.14. The time-dependent biodistribution of Cy5.5-Alb-ECMaI-PROTAC and Cy5.5-ARV-771 was observed using the IVIS Lumina Series III system.

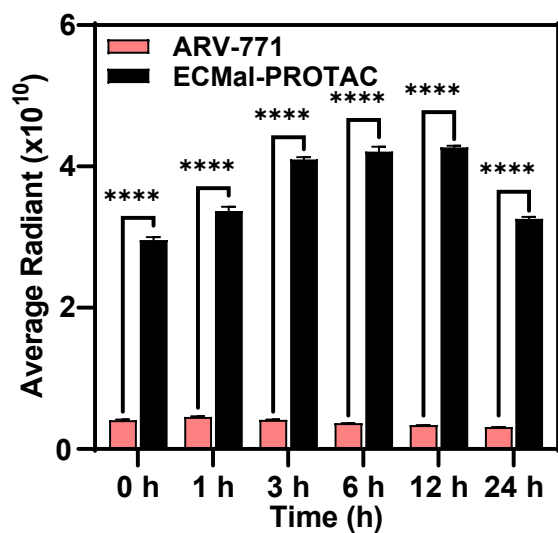


Figure 4.15. Quantification analysis on the Cy5.5 fluorescence at tumor tissues in NIRF images (n = 3, **** $p < 0.0001$).

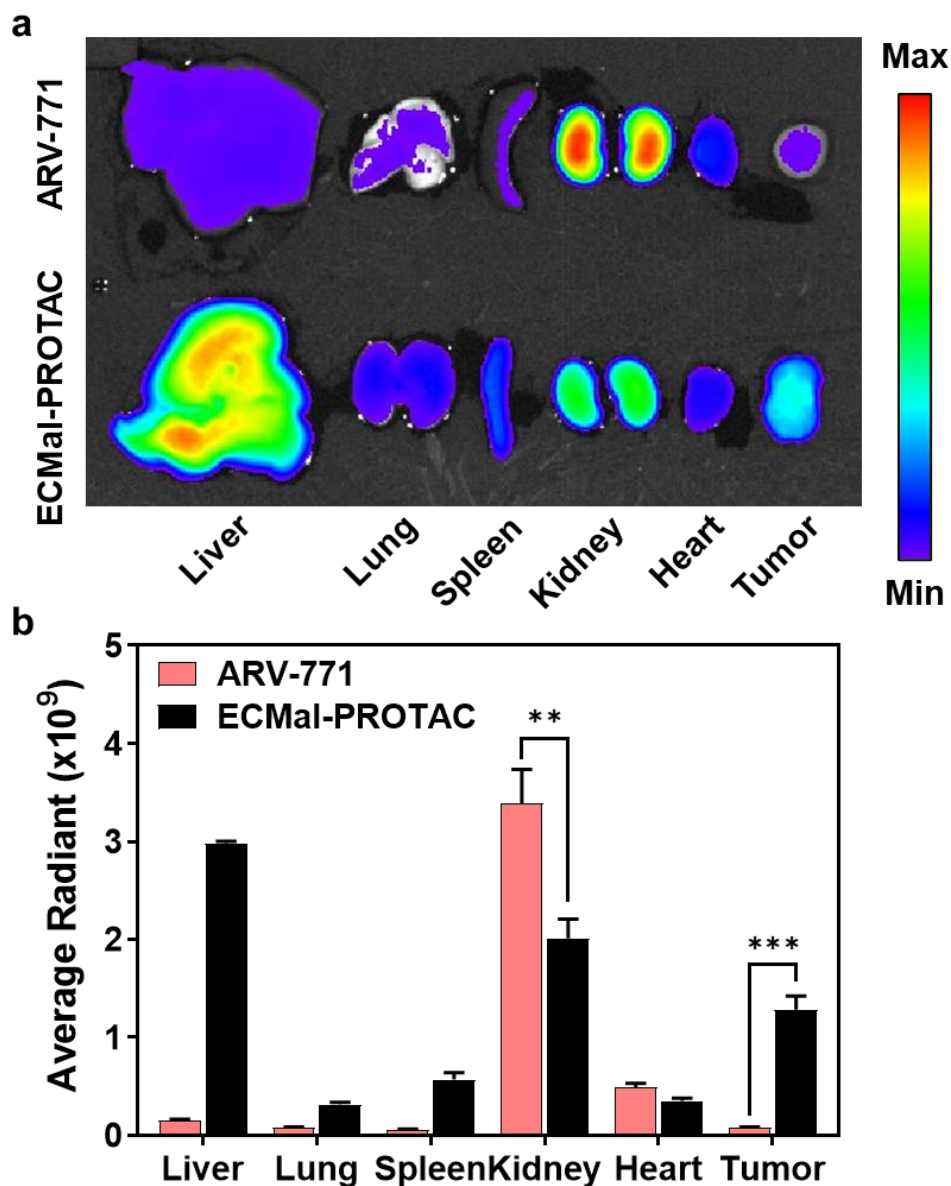


Figure 4.16. (a) The ex vivo fluorescence images of excised major organs and tumor tissues after the single administration of Cy5.5-ARV-771 (3 mg/kg, equiv. to ARV-771) and Cy5.5-Alb-ECMal-PROTAC (3 mg/kg, equiv. to ARV-771), and (b) their quantified fluorescence intensities. All data were denoted as means \pm S.D. ($n = 3$, ** $p < 0.01$, *** $p < 0.001$).

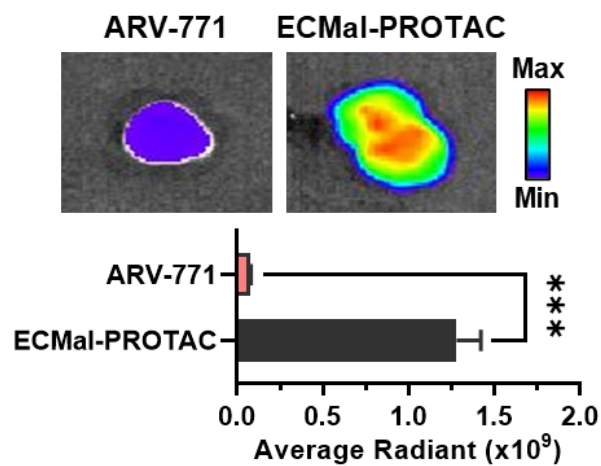


Figure 4.17. The ex vivo fluorescence images of excised tumor tissues were obtained and their fluorescence intensities were quantified (n = 3, *** $p < 0.001$).

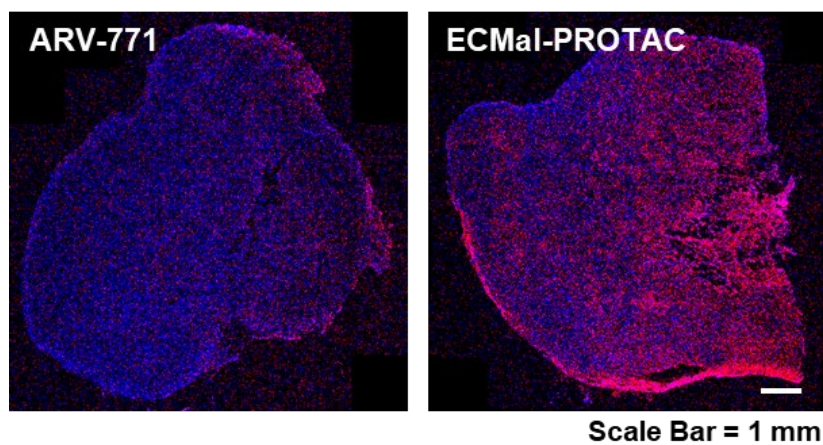


Figure 4.18. The whole tumor confocal fluorescence images were additionally obtained with the excised tumors.

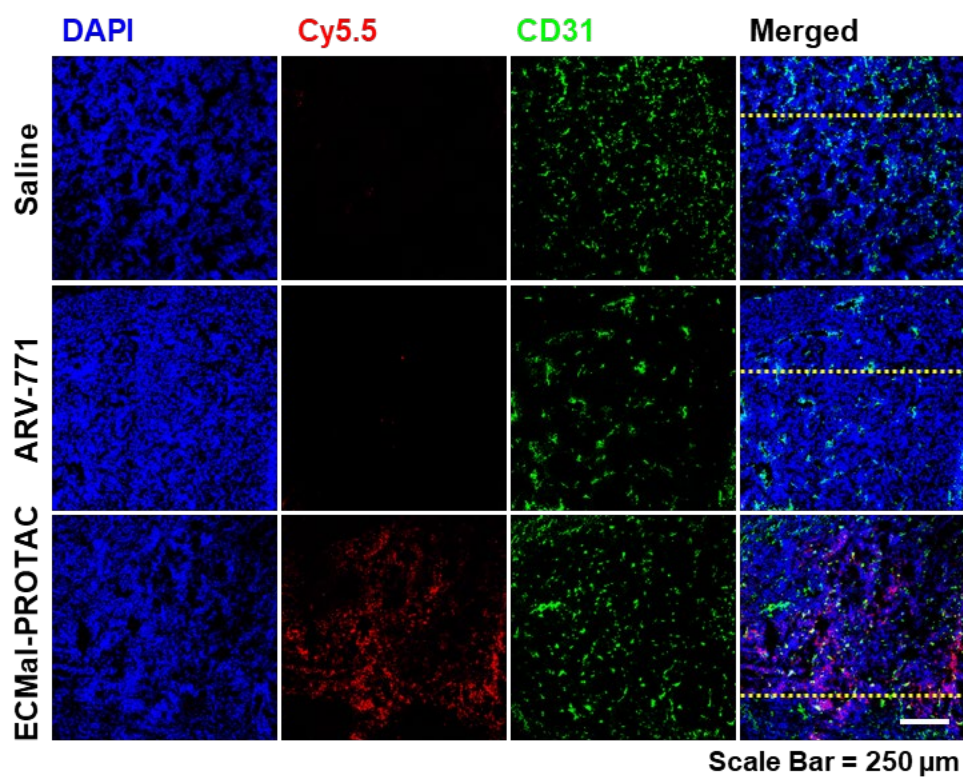


Figure 4.19. Excised tumor tissues were further co-stained with DAPI (nuclei) and CD31 (blood vessel), analyzed with confocal fluorescence microscopy.

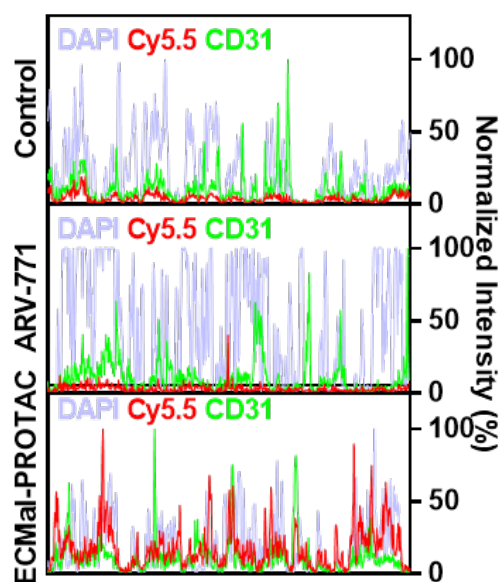


Figure 4.20. Cross-sectional fluorescence signals of yellow line on the figure 3.19 were plotted. Cy5.5-Alb-ECMal-PROTAC was uniformly distributed throughout the entire tumor tissues. All data were denoted as means \pm S.D.

4.3.4. *In vivo therapeutic efficacy of ECMal-PROTAC in tumor-bearing mice*

Upon accomplishing the identification of *in vitro* cellular activities and pharmacokinetic properties of ECMal-PROTAC and ARV-771, their *in vivo* antitumor performances against 4T1 tumor-grafted mice were subsequently compared to each other. When the tumor volumes reached $100 \pm 10 \text{ mm}^3$, the ECMal-PROTAC and ARV-771 were intravenously injected at a dose of 10 mg/kg (equivalent to ARV-771) once every 3 d for 15 d (four injections in total). The changes in tumor size with ECMal-PROTAC, ARV-771, or saline treatment were checked every two days, showing an outstanding therapeutic effect of ECMal-PROTAC. As depicted in Figure 4.21, the tumor sizes of the saline- and ARV-771-treated groups after 15 d were enlarged to 15.8- and 14.8-fold, respectively, exerting no statistically significant difference in their tumor growth rates. Unlike the ARV-771-treated groups, the administration of ECMal-PROTAC was found to remarkably suppress the increase in tumor size. The volume of the ECMal-PROTAC-treated tumor was $176.13 \pm 81.62 \text{ mm}^3$ after 15 d of medication, which was 6.1- and 5.3-fold smaller than saline- and ARV-771-treated ones, respectively. Accounting for the similar *in vitro* cytotoxicity of ARV-771 and ECMal-PROTAC, the notable *in vivo* antitumor potency of ECMal-PROTAC over ARV-771 was judged to be originated from its prolonged circulation and tumor-specific accumulation by the *in situ* albumin binding. The *ex vivo* digital further assured the effectiveness of ECMal-PROTAC, showing much smaller tumor size compared to other groups. (Figure 4.22a). In addition, TUNEL-stained fluorescence images of tumor tissues exhibited prevalent cancer cell apoptosis with the ECMal-PROTAC treatment (Figure 4.22b).

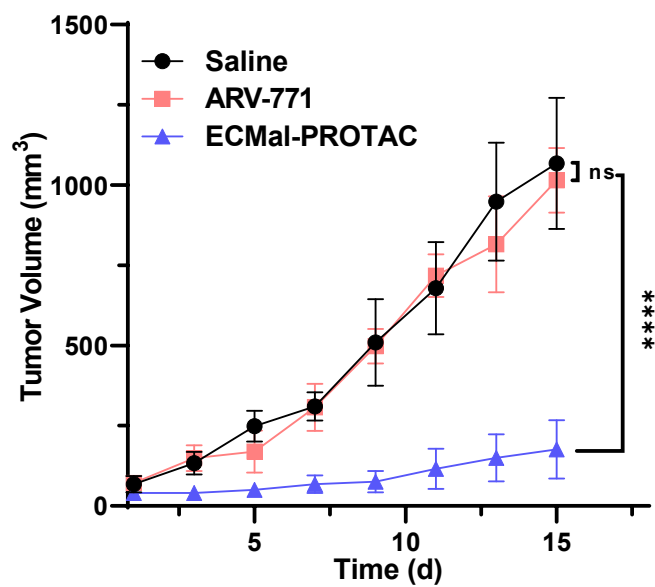


Figure 4.21. The tumor growth profile according to the repeated treatment of saline, native ARV-771, or ECMal-PROTAC was obtained (n =5, ns = not significant, **** p < 0.0001).

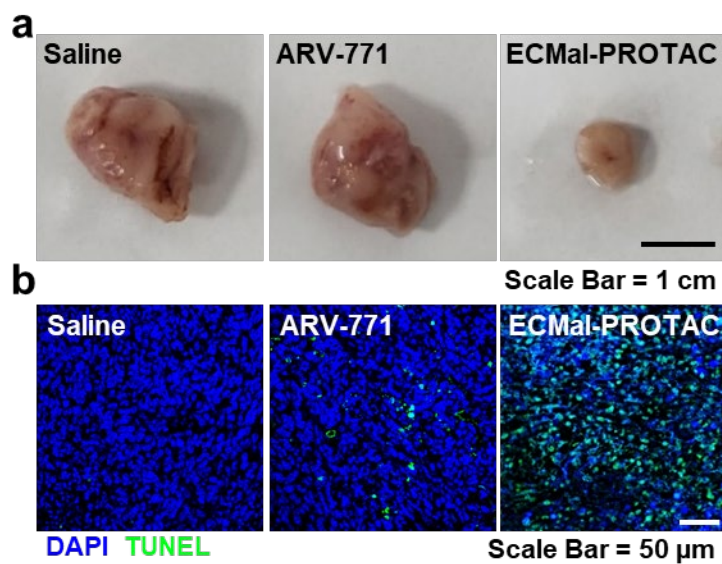


Figure 4.22. (a) Digital images of excised tumors indicated that the treatment of ECMal-PROTAC successfully suppressed tumor growth compared to other experimental groups. (b) Confocal fluorescence images of excised tumor tissues after their TUNEL staining.

During the therapeutic procedures, none of the subject mice which were injected with ECMal-PROTAC or ARV-771 suffered from serious systemic adverse events or elicited meaningful weight loss (Figure 4.23). In addition, the hematoxylin and eosin (H&E) histology of resected normal organs after 19 d did not express any serious abnormalities, while strong damages were observed in the ECMal-PROTAC-treated tumor tissue (Figure 4.24). The repeated administration of ARV-771 did not harm the integrities of normal organs either, however, it exhibited poor anticancer efficacy. Noteworthy, the impact of ECMal-PROTAC on hepatic tissues was also negligible, even if its considerable proportion had been determined to be delivered to the liver in the biodistribution test. When hepatic tissues were furtherly evaluated with TUNEL assay, the apoptotic rate in the ECMal-PROTAC-treated liver was not much different from that in the saline-treated one (Figure 4.25). These results suggested that ECMal-PROTAC exerted relatively much-relieved toxicity to normal cells with low BRD4 expression levels [38]. The treatment of ARV-771 rarely affected both normal organs and tumor tissues, which was thought to be due to its rapid clearance and poor bioavailability.

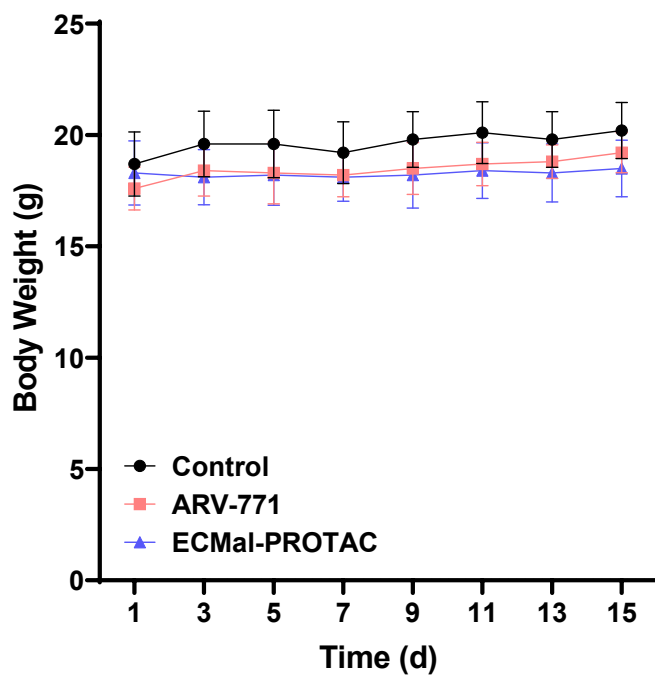


Figure 4.23. The changes in body weights of saline-, ARV-771- (10 mg/kg), and ECMal-PROTAC (10 mg/kg, equivalent to ARV-771)-treated mice. All data were denoted as means \pm S.D. (n = 5).

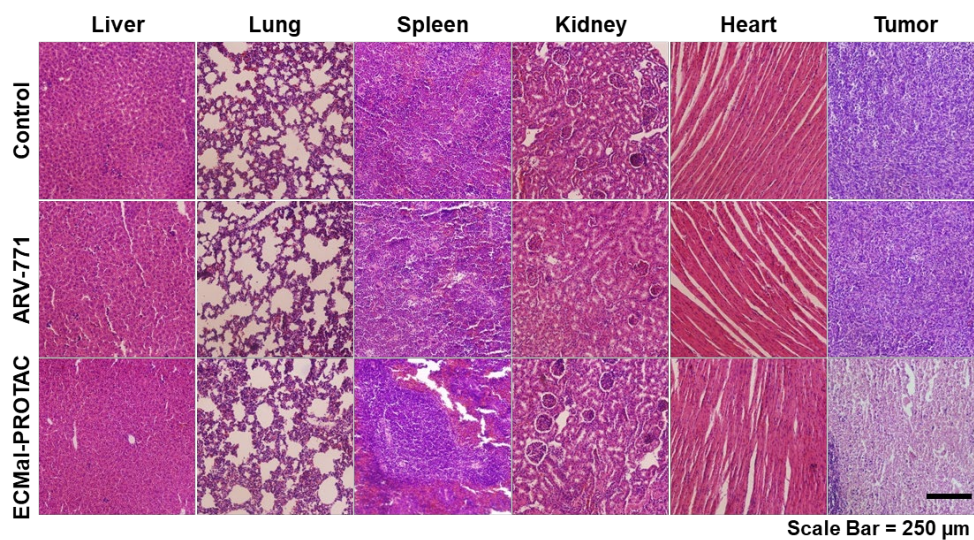


Figure 4.24. The histological analysis of major organs extracted from experimental groups with multiple administrations of saline, ARV-771 (10 mg/kg), and ECMal-PROTAC (10 mg/kg, equivalent to ARV-771), demonstrating the systemic safety of ECMal-PROTAC.

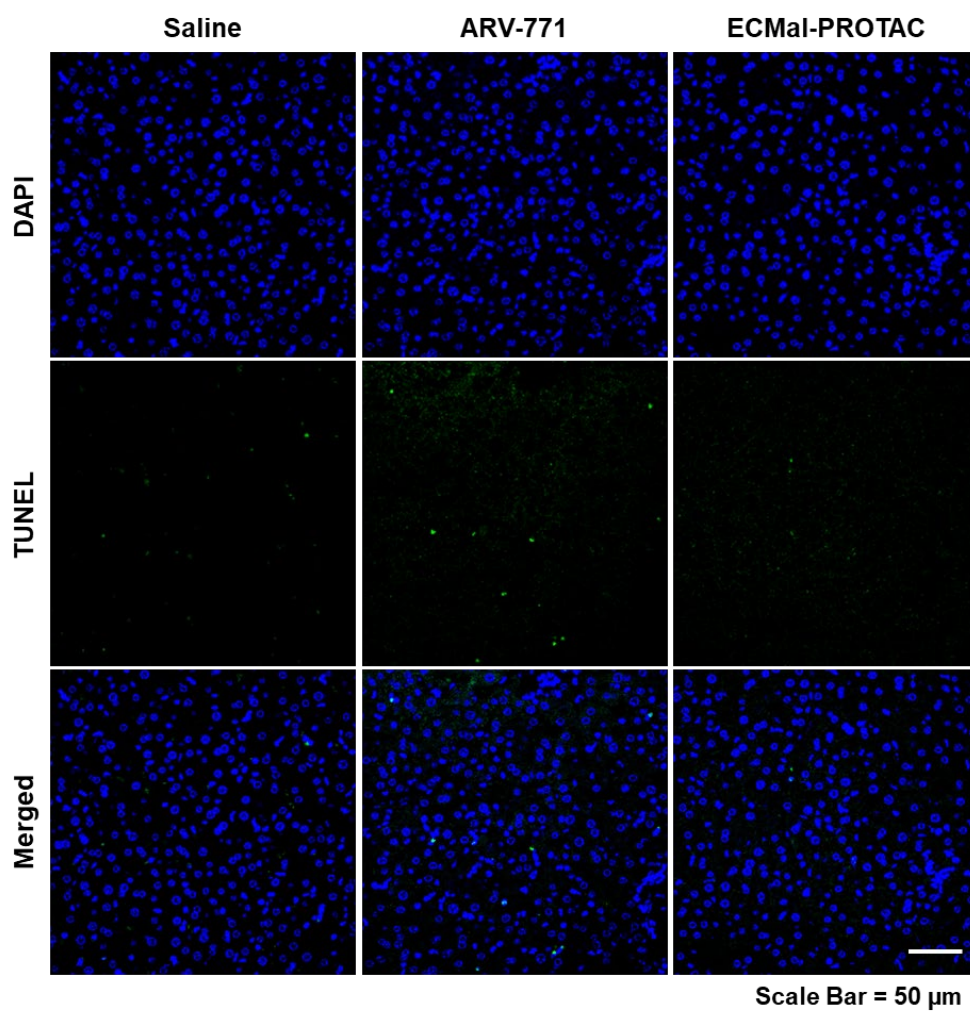


Figure 4.25. TUNEL assay of livers excised from experimental groups repeatedly treated with saline, ARV-771 (10 mg/kg), and ECMal-PROTAC (10 mg/kg, equivalent to ARV-771).

Excised tumor tissues were additionally performed with their western blot and histological analysis to demonstrate the reduction of BRD4 and other downstream protein levels. As shown in Figure 4.26, ECMal-PROTAC-treated tumor tissues were confirmed to have much lower levels of BRD4, c-Myc, and Bcl-2 than saline-treated tumor tissues, whereas ARV-771-treated ones were almost unchanged in their internal protein levels. Quantitatively, the relative expression levels of BRD4, c-Myc, and Bcl-2 in ECMal-PROTAC-treated tumors were 7.5-, 2.2-, and 2.3-fold lower than those in saline-treated tumors, respectively (Figure 4.27). When histologically visualizing the BRD4 and c-Myc in tumor tissues, the ECMal-PROTAC-treated tumors displayed obviously weak fluorescence signals compared to those treated with saline or ARV-771 (Figure 4.28). The BRD4 degradation in the ARV-771-treated tumor was regarded as negligible as its delivered amount to the tumor was not enough to provoke therapeutic responses. The histologies of tumor tissues with DAB staining additionally validated the successful degradation and downregulation of BRD4 through the ECMal-PROTAC treatment (Figure 4.29). The general mechanism for BRD4 deficiency-associated cancer cell apoptosis was illustrated in Figure 4.30. BRD4s overexpressed in tumors are translocated to nuclei and promote the transcription of oncogenes MYC and BCL2 to their mRNAs, and the transcribed mRNAs are subsequently translated to c-Myc and Bcl-2 proteins [39]. The c-Myc proteins play a key role in the growth and proliferation of cancer cells, and Bcl-2s elicit an anti-apoptotic effect [40, 41]. Therefore, when tumors are treated with BRD4-degrading PROTACs, the insufficiency in BRD4 efficiently prohibits intracellular c-Myc and Bcl-2 production, resulting in cell apoptosis. Overall, ECMal-PROTAC was confirmed to have low systemic toxicity and high tumor

localization ability by in situ binding to circulating albumin and to treat tumors with tremendous potency utilizing the BRD4 degradation pathway.

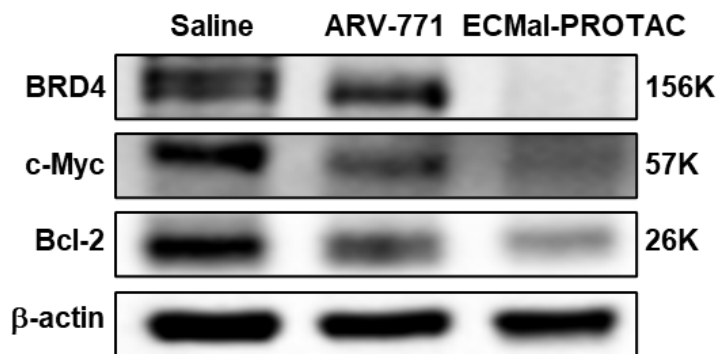


Figure 4.26. Western blot assay of excised tumor tissues with ECMal-PROTAC treatment showed reduced levels of BRD4, c-Myc, and Bcl-2.

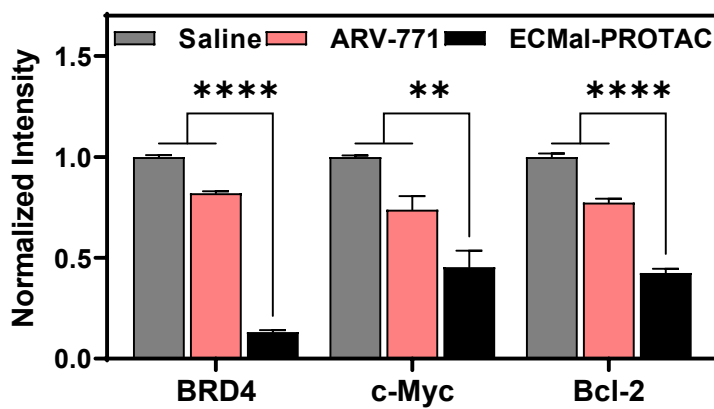


Figure 4.27. Quantification analysis of the band intensity on the figure 4.26.

Significance (** $p < 0.01$, **** $p < 0.0001$) was determined by Student's t-test.

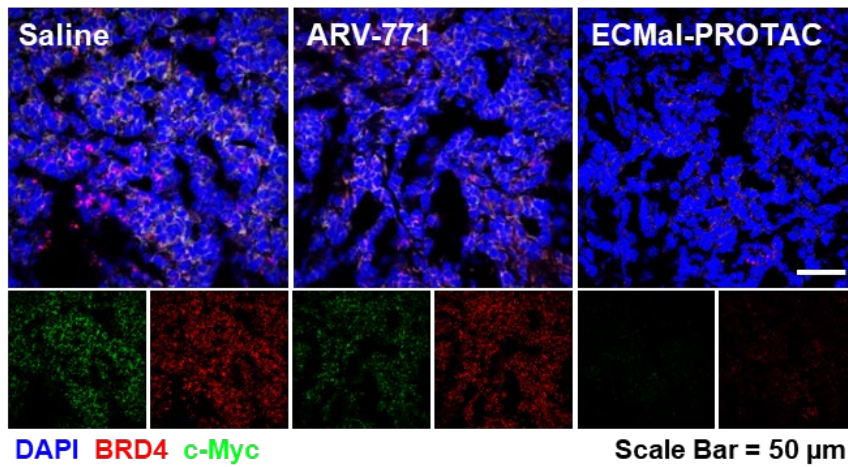


Figure 4.28. The BRD4-degrading and subsequent c-Myc-suppressing properties of ECMal-PROTAC were further visualized by staining tumor tissues with anti-BRD4 and anti-c-Myc.

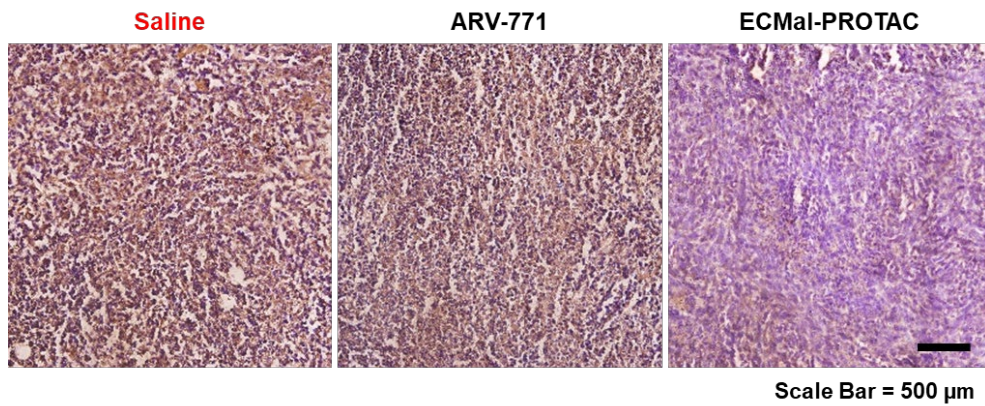


Figure 4.29. DAB-stained tumors with repeated treatment of saline, ARV-771, and ECMal-PROTAC, showing the BRD4 deficiency in ECMal-PROTAC-treated tissues.

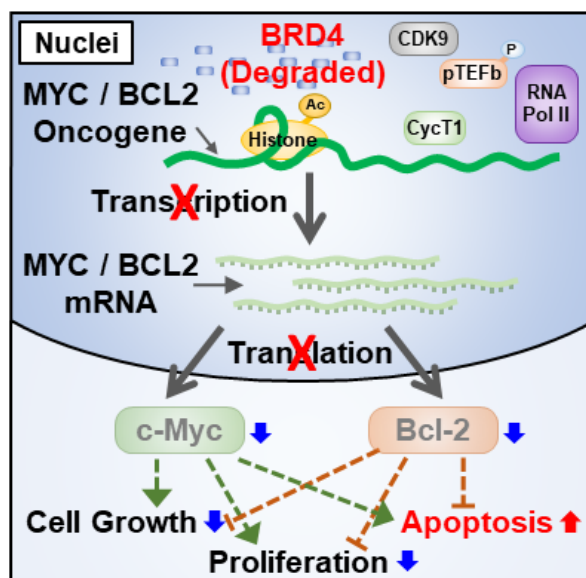


Figure 4.30. The MOA of BRD4-degrading PROTAC was schematically described. The degradation of BRD4 inhibits the transcription of oncogenes including MYC and Bcl-2, thereby lowering the intracellular concentrations of translated c-Myc and Bcl-2. The deficiency of c-Myc and Bcl-2 significantly depresses cell growth and proliferation, and eventually leads to cell apoptosis. All data were denoted as means \pm S.D.

4.4. Conclusions

Despite the therapeutic versatility of PROTACs, their undesirable pharmacokinetic property and the poor delivery performance of existing PROTAC carriers have hampered their applications in cancer therapy. Herein, ECMal-PROTAC, the in situ albumin-binding PROTAC, was proposed as a novel PROTAC delivery system. ECMal-PROTAC was synthesized with high purity utilizing simple click chemistry, rapidly bound to albumin via Thiol-Mal reaction, and degraded to free ARV-771 under the presence of esterase. After being uptaken into cancer cells, it effectively catalyzed the degradation of BRD4, followed by the downregulation of c-Myc and Bcl-2, and induced BRD4 deficiency-mediated apoptosis. As administered intravenously, ECMal-PROTAC spontaneously and rapidly bound to innate albumin in blood plasma, achieving its improved pharmacokinetic properties and high accumulation in tumor tissue. The ECMal-PROTAC delivered inside cancer cells actively degraded BRD4 and inhibited the expression of downstream c-Myc and Bcl-2 proteins after being esterase-specifically detached from albumin, thereby exhibiting remarkable anticancer efficacy by silencing the BRD4-related gene transcription pathway. In conclusion, ECMal-PROTAC was confirmed to be a highly promising strategy due to its improved pharmacokinetic profile, potent tumor targetability, and universal applicability to various types of PROTACs in cancer treatment.

4.5. References

1. Gao, H., X. Sun, and Y. Rao, PROTAC technology: opportunities and challenges. *ACS Medicinal Chemistry Letters*, 2020. 11(3): p. 237-240.
2. Paiva, S.-L. and C.M. Crews, Targeted protein degradation: elements of PROTAC design. *Current opinion in chemical biology*, 2019. 50: p. 111-119.
3. Neklesa, T.K., J.D. Winkler, and C.M. Crews, Targeted protein degradation by PROTACs. *Pharmacology & therapeutics*, 2017. 174: p. 138-144.
4. Toure, M. and C.M. Crews, Small-molecule PROTACS: new approaches to protein degradation. *Angewandte Chemie International Edition*, 2016. 55(6): p. 1966-1973.
5. Zeng, S., et al., Proteolysis targeting chimera (PROTAC) in drug discovery paradigm: Recent progress and future challenges. *European Journal of Medicinal Chemistry*, 2021. 210: p. 112981.
6. Edmondson, S.D., B. Yang, and C. Fallan, Proteolysis targeting chimeras (PROTACs) in 'beyond rule-of-five' chemical space: Recent progress and future challenges. *Bioorganic & Medicinal Chemistry Letters*, 2019. 29(13): p. 1555-1564.
7. He, S., et al., Aptamer-protac conjugates (apcs) for tumor-specific targeting in breast cancer. *Angewandte Chemie International Edition*, 2021. 60(43): p. 23299-23305.
8. Saraswat, A., et al., Galactose-decorated liver tumor-specific nanoliposomes incorporating selective BRD4-targeted PROTAC for hepatocellular carcinoma therapy. *Heliyon*, 2022: p. e08702.

9. Zhang, C., et al., Semiconducting polymer nano-PROTACs for activatable photo-immunometabolic cancer therapy. *Nature communications*, 2021. 12(1): p. 1-12.
10. Shim, M.K., et al., Carrier-free nanoparticles of cathepsin B-cleavable peptide-conjugated doxorubicin prodrug for cancer targeting therapy. *Journal of Controlled Release*, 2019. 294: p. 376-389.
11. Torrice, M., Does nanomedicine have a delivery problem? 2016, ACS Publications.
12. Hare, J.I., et al., Challenges and strategies in anti-cancer nanomedicine development: An industry perspective. *Advanced Drug Delivery Reviews*, 2017. 108: p. 25-38.
13. Liu, J., et al., Cancer selective target degradation by folate-caged PROTACs. *Journal of the American Chemical Society*, 2021. 143(19): p. 7380-7387.
14. Maneiro, M.a., et al., Antibody-PROTAC conjugates enable HER2-dependent targeted protein degradation of BRD4. *ACS chemical biology*, 2020. 15(6): p. 1306-1312.
15. Wilhelm, S., et al., Analysis of nanoparticle delivery to tumours. *Nature reviews materials*, 2016. 1(5): p. 1-12.
16. Yamasaki, K., et al., Albumin-drug interaction and its clinical implication. *Biochimica et Biophysica Acta (BBA)-General Subjects*, 2013. 1830(12): p. 5435-5443.
17. Cho, H., et al., Emerging Albumin-Binding Anticancer Drugs for Tumor-Targeted Drug Delivery: Current Understandings and Clinical Translation. *Pharmaceutics*, 2022. 14(4).

18. Hoogenboezem, E.N. and C.L. Duvall, Harnessing albumin as a carrier for cancer therapies. *Advanced drug delivery reviews*, 2018. 130: p. 73-89.
19. Neumann, E., et al., Native albumin for targeted drug delivery. *Expert opinion on drug delivery*, 2010. 7(8): p. 915-925.
20. Davidson, S.M., et al., Direct evidence for cancer-cell-autonomous extracellular protein catabolism in pancreatic tumors. *Nature medicine*, 2017. 23(2): p. 235-241.
21. Zhao, P., et al., Roles of Albumin-Binding Proteins in Cancer Progression and Biomimetic Targeted Drug Delivery. *ChemBioChem*, 2018. 19(17): p. 1796-1805.
22. Chung, S.W., et al., Albumin-binding caspase-cleavable prodrug that is selectively activated in radiation exposed local tumor. *Biomaterials*, 2016. 94: p. 1-8.
23. Kratz, F., et al., A novel macromolecular prodrug concept exploiting endogenous serum albumin as a drug carrier for cancer chemotherapy. *Journal of medicinal chemistry*, 2000. 43(7): p. 1253-1256.
24. Abu Ajaj, K., et al., In vitro and in vivo study of an albumin-binding prodrug of doxorubicin that is cleaved by cathepsin B. *Cancer chemotherapy and pharmacology*, 2009. 64(2): p. 413-418.
25. Sun, B., et al., BET protein proteolysis targeting chimera (PROTAC) exerts potent lethal activity against mantle cell lymphoma cells. *Leukemia*, 2018. 32(2): p. 343-352.

26. Raina, K., et al., PROTAC-induced BET protein degradation as a therapy for castration-resistant prostate cancer. *Proceedings of the National Academy of Sciences*, 2016. 113(26): p. 7124-7129.
27. Bai, Y., et al., β -Cyclodextrin-modified hyaluronic acid-based supramolecular self-assemblies for pH-and esterase-dual-responsive drug delivery. *Carbohydrate polymers*, 2020. 246: p. 116654.
28. Mantovani, G., et al., Design and synthesis of N-maleimido-functionalized hydrophilic polymers via copper-mediated living radical polymerization: a suitable alternative to PEGylation chemistry. *Journal of the American Chemical Society*, 2005. 127(9): p. 2966-2973.
29. Bern, M., et al., The role of albumin receptors in regulation of albumin homeostasis: Implications for drug delivery. *Journal of Controlled Release*, 2015. 211: p. 144-162.
30. Lee, S.Y., et al., Esterase-sensitive cleavable histone deacetylase inhibitor-coupled hyaluronic acid nanoparticles for boosting anticancer activities against lung adenocarcinoma. *Biomaterials science*, 2019. 7(11): p. 4624-4635.
31. Jahanban-Esfahlan, A., et al., Recent developments in the detection of bovine serum albumin. *International journal of biological macromolecules*, 2019. 138: p. 602-617.
32. Bradshaw, A.D., The role of secreted protein acidic and rich in cysteine (SPARC) in cardiac repair and fibrosis: Does expression of SPARC by macrophages influence outcomes? *Journal of molecular and cellular cardiology*, 2016. 93: p. 156-161.

33. White, M.E., J.M. Fenger, and W.E. Carson III, Emerging roles of and therapeutic strategies targeting BRD4 in cancer. *Cellular immunology*, 2019. 337: p. 48-53.
34. Qin, A.-c., et al., The therapeutic effect of the BRD4-degrading PROTAC A1874 in human colon cancer cells. *Cell Death & Disease*, 2020. 11(9): p. 1-12.
35. Wu, X., et al., Inhibition of BRD4 suppresses cell proliferation and induces apoptosis in renal cell carcinoma. *Cellular Physiology and Biochemistry*, 2017. 41(5): p. 1947-1956.
36. Sleep, D., Albumin and its application in drug delivery. *Expert opinion on drug delivery*, 2015. 12(5): p. 793-812.
37. Chen, Y., et al., Proteolysis-targeting chimera (PROTAC) delivery system: Advancing protein degraders towards clinical translation. *Chemical Society Reviews*, 2022.
38. Bakshi, S., et al., Toxicity of JQ1 in neuronal derivatives of human umbilical cord mesenchymal stem cells. *Oncotarget*, 2018. 9(73): p. 33853.
39. Liu, B., et al., BRD4-directed super-enhancer organization of transcription repression programs links to chemotherapeutic efficacy in breast cancer. *Proceedings of the National Academy of Sciences*, 2022. 119(6): p. e2109133119.
40. Reed, J.C., Double identity for proteins of the Bcl-2 family. *Nature*, 1997. 387(6635): p. 773-776.
41. Wang, H., et al., c-Myc depletion inhibits proliferation of human tumor cells at various stages of the cell cycle. *Oncogene*, 2008. 27(13): p. 1905-1915.

Chapter 5. Conclusions

The side effects of first-line chemotherapy caused by cancer treatment have always been considered as great challenge. Several studies have been introduced to overcome this problem, however, there is limitation to satisfying both cancer cell specificity and targeting efficiency. In this study, cancer targeting efficiency and specificity of conventional anticancer agents were improved by using two types of tumor-targeting moieties and two types of linkers.

At first study, MMAE, which is not suitable for single chemotherapy due to its strong toxicity, was introduced for prodrug. Phe-Arg-Arg-Gly peptide was conjugated to MMAE as multifunctional linker. This modified chemodrug was self-assembled as nanoparticle due to interaction between phenylalanine of adjacent molecules. Also, MMAE prodrug released free MMAE at the tumor site because tumor overexpressed enzyme cathepsin B cleaved Arg-Arg peptide. As a result, FRRG-MMAE prodrug shows enhanced tumor targeting efficiency and tumor specific cytotoxicity.

Next, a new prodrug was developed by modifying doxorubicin, which is also used as a first-line chemodrug. A successful drug delivery system using albumin in the human blood was introduced using a maleimide functional moiety, and RR peptide was used for tumor specificity. Using these strategies, effective tumor targeted prodrug was developed with minimized side effects to normal cells.

Finally, a new prodrug was developed by modifying ARV-771 PROTAC, which is used only as a combination therapy due to its low cancer targeting and specificity. By introducing maleimide functional group, low tumor targeting efficiency

of ARV-771 was overcome. Also, maleimide functional group was conjugated to ARV-771 via ester bond which is cleaved by tumor overexpressed lysosomal esterase. As a result, it was possible to maximize the effect of ARV-771 which showed little effect when used monotherapy. In addition, due to its BRD4 protein degradation mechanism, related oncogene of PD-L1 was regulated. As a result, albumin bound BRD4 degradable PROTAC has a potential of cancer immunotherapy.

In summary, by using tumor specific cleavable linkers and functional moieties for the purpose, it is possible to reduce the side effects of conventional anticancer drugs and enhance the anticancer effect only on the tumor site. Through this study, various methods for modifying conventional anticancer agents could be suggested by introducing appropriate linkers and functional moieties. This new prodrug platform design could lead the development of customized targeting chemotherapy.

국문초록

표적형 항암 치료를 위한 리소좀 특이적 나노약물

암 치료제의 발전에도 불구하고, 기존의 항암제는 환자에 대한 범용성과 접근성이 용이하여 여전히 암 치료에 최우선적으로 사용되고 있다. 그러나 이러한 항암제는 특유의 작용 방식으로 인한 비특이적 작용으로 인한 심각한 부작용을 가지고 있다. 위와 같은 이유로 암을 표적적으로 치료하기 위해 여러가지 개선된 항암제가 개발되었다. 이러한 개선을 통해서 기존 약물들의 종양 표적 능력은 향상되었음에도 불구하고, 여전히 몇 가지의 한계점이 존재하고 있다. 이를 위해 본 논문에서는 기존의 표적형 항암제를 제작하는 방식에 프로드러그 전략을 조합하여 새로운 방식의 종양 표적형 프로드러그를 개발하였다. 제 1장에서는 독성이 높은 모노메틸 아리스타틴 E (MMAE)를 독성을 나타내는 약물로 도입하였다. 위 약물의 독성을 종양 특이적으로 나타내게 하기 위해, 종양 과발현 효소인 카텡신 B에 의해 절단가능한 펩티드 FRRG를 MMAE에 접합시켰다. FRRG 펩타이드의 페닐알라닌은 분자간 소수성 상호작용을 가짐으로써, FRRG가 결합된 MMAE가 나노 제형을 형성할 수 있도록 하였다. 이러한 FRRG-MMAE의 나노 구조는 EPR 효과로 인해 종양 부위에 축적되고, 종양 조직에서 과발현된 카텡신 B 효소는 MMAE에 접합된 FRRG 펩티드를 절단하여 종양 부위에서만 MMAE를 방출하게 하였다. 제 2장에서는 종양 표적화 효율을 높이기 위해 알부민을 약물 전달체로 채택하였다. 알부민을 사용하기 위해 카텡신 B에 의해 절단되는 펩티드 FRRG가 결합된 독소루비신 항암제에 말레이마이드 작용기를 도입하였다. 합성된 Maleimide-

FRRG-Dox는 클릭 반응을 통해 체내 알부민에 결합할 수 있어 종양 표적화 효율과 체내 반감기의 개선이 가능하였다. 제 3장에서는 항암제로써 새로운 신약인 PROTAC을 도입하고, 말레이마이드 작용기를 에스터 결합을 이용하여 합성하였다. Maleimide-PROTAC은 알부민 결합을 통해 종양 부위에 축적되었고, 종양에서 과발현된 에스테레이즈에 의해 PROTAC을 방출하였다. 정리하자면 본 연구에서는, 3 가지 부분으로 구성된 새로운 프로드러그를 디자인하고 그 효능을 평가하였다. 새로운 프로드러그 디자인의 첫 부분에는 작용기 또는 아미노산을 도입하여 종양 표적능의 향상을 도모하였다. 두 번째 부분은 종양 과발현 효소 또는 종양 미세 환경에 의해 절단되는 링커를 도입하여 종양 특이적으로 약물이 작용될 수 있도록 하였다. 마지막 부분은 1차 화학 요법에서 일반적으로 사용되는 항암제를 도입하여 종양 표적적이고 특이적으로 약물이 방출될 수 있도록 하였다. 개선된 약물들은 종양 표적화 효율의 향상과 종양 특이적인 독성을 나타내는 것이 확인되었고, 이를 통해 기존 항암제의 한계점이 극복되었음을 확인할 수 있었다.

주요어 : 종양, 표적 치료, 카텡신 B, 알부민, 펩티드-약물 결합체, 프로탁

학번 : 2016-20832